

Considerations in Designing a Nuclear Power Plant with a Hydrogen and Biofuels Facility

Lauren Ayers, Matthew Chapa, Lauren Chilton, Robert Drenkhahn, Brendan Ensor,
Jessica Hammond, Kathryn Harris, Anonymous Student, Sarah Laderman,
Ruaridh Macdonald, Benjamin Nield, Uuganbayar Otgonbaatar,
Alex Salazar, Derek Sutherland, Aditi Verma, Rebecca Krentz-Wee, and Elizabeth Wei
December 14, 2011

Contents

I	Introduction	9
II	Background	10
1	Core	11
1.1	Main Goals of the Core Group	11
1.2	Design Parameters	11
1.2.1	Biofuels Coordination	11
1.2.2	Viability to get Licensed and Built in the Upcoming Decades	12
1.3	Design Options and Evaluation	13
1.3.1	Liquid Metal Fast Reactors	13
1.3.2	Molten Salt Reactors	14
1.3.3	Gas Cooled Reactors	14
1.3.4	Supercritical Coolant Reactors	15
1.3.5	Table of Design Comparison	15
2	Process Heat	17
2.1	Goals of the Process Heat Design Group	17
2.2	Design Challenges	17
2.3	Possible Heat Exchanger Designs	17
2.3.1	Straight Shell-and-Tube	18
2.3.2	Modified Shell-and-Tube	18
2.3.3	Plate	19
2.3.4	Printed Circuit	19
2.3.5	Ceramic	19
3	Hydrogen	21
3.1	Goals of Hydrogen	21
3.2	Design Options and Evaluation	21
3.2.1	Steam-Methane Reforming	22
3.2.2	Water Electrolysis	22
3.2.3	Westinghouse Sulfur Process	23
3.2.4	Hydrogen from Urine	24
3.2.5	Hydrogen from Bacteria	25
3.2.6	High Temperature Steam Electrolysis	25
3.2.7	Br-Ca-Fe UT-3	25
4	Biofuels	27
4.1	Main Goals of Biofuels	27
4.2	Design Parameters	27
4.3	Design Options and Evaluation	27
4.3.1	Possible Sources of Biomass	27
4.3.2	Electrofuels to Hydrogen Process	29
4.3.3	Algae Transesterification Process	30
4.3.4	Fermentation to Ethanol Process	30
4.3.5	Fischer Tropsch Process	30
III	Results	33
5	Overall Plant Design	33

6	Core	35
6.1	Process Overview	35
6.1.1	Core Overview	35
6.1.2	Secondary Overview	35
6.1.3	Table of Important Parameters	36
6.2	Primary System Design	37
6.2.1	Fuel	37
6.2.2	Criticality Calculations	37
6.2.3	Shutdown Margin	38
6.2.4	Thermal Analysis	38
6.2.5	Depletion Analysis	39
6.2.6	Core Reactivity Feedback Parameters	40
6.2.7	Natural Circulation and Flow Analysis	40
6.2.8	Safety Systems	44
6.3	Secondary System	45
6.3.1	Heat Exchanger	46
6.3.2	Condensers and Compressors	48
6.3.3	Accident Scenario Analysis	48
6.4	Economics	49
7	Process Heat	51
7.1	Process Overview	51
7.2	Heat Exchangers	52
7.2.1	Choice of Material and Working Fluid	52
7.3	PCHE Design	54
7.4	Process Heat PCHEs	55
7.4.1	PCHE1	55
7.4.2	PCHE2	57
7.4.3	PCHE Conclusions	59
7.5	Fouling	59
7.6	Heat Exchanger at Biofuels Plant	60
7.7	Heat Sink	61
7.7.1	Purpose, Location, and Components	61
7.7.2	Heat Rate and Design	61
7.7.3	Environmental Concerns	61
7.8	Process Heat System Costs	62
7.8.1	PCHE	62
7.8.2	Circulator	62
7.8.3	Piping	62
7.9	Heat Storage Details	63
7.9.1	Lithium Chloride	63
7.9.2	Alloy 20	63
7.9.3	System Design	64
7.9.4	PCM Sizing and Design	67
7.9.5	Heat Storage Summary	70
7.10	Circulator	70
7.11	Heat Sink	71
7.11.1	Purpose, Location, and Components	71
7.11.2	Heat Rate and Design	71
7.11.3	Environmental Concerns	71
7.12	Piping	71
7.13	Process Heat System Costs	73
7.13.1	PCHE	73
7.13.2	Circulator	73

7.13.3 Piping	73
8 Hydrogen	74
8.1 Introduction	74
8.2 High Temperature Steam Electrolysis (HTSE)	74
8.2.1 HTSE Production Plant	74
8.2.2 Materials and Components	78
8.2.3 Material Corrosion	80
8.3 Other Design Considerations	81
8.3.1 Biofuels shutdown	81
8.3.2 Core shutdown	81
8.3.3 Mechanical failures	81
8.4 Conclusions	81
9 Biofuels	82
9.1 Process Overview	82
9.2 Switchgrass	82
9.2.1 Densification	84
9.2.2 Transportation to Site	85
9.3 Gasification	85
9.4 Acid Gas Removal	87
9.5 Fischer-Tropsch Reactor	89
9.6 Fractional Distillation and Refining	94
9.7 Biofuels Results Summary	97
IV Conclusions	98
10 Future Work	98
10.1 Short-Term Future Work	98
10.1.1 Process Heat	98
10.1.2 Biofuels Plant	98
10.2 Long-Term Future Work	99
10.2.1 Core	99
10.2.2 Process Heat	99
10.2.3 Biofuels Plant	99
11 Economics Of Design	100
11.1 Expected Revenue	100
V Acknowledgements	100
References	101
VI Appendix A: Core Parameter QFD	109
VII Appendix B: Criticality Model	111
VIII Appendix C: Investigation of PCHE thermal hydraulics	120

IX	Appendix D: Implementation of switchgrass as feedstock for a industrial biofuels process in a nuclear complex	126
X	Appendix E: Impact of gasifier design on FT product selectivity	130
XI	Appendix G: Excess O₂ and Hydrogen Storage	137

List of Figures

1	Combined Multiple Shell-Pass Shell-and-Tube Heat Exchanger (CMSP-STHX) with continuous helical baffles [158]	18
2	A PCHE heat exchanger made of Alloy 617 with straight channels [160]. The semi-circular fluid channels have a diameter for 2mm.	20
3	Steam methane reforming block diagram [48]	22
4	Electrolysis process block diagram	23
5	The Westinghouse Sulfur Process for hydrogen production [4].	24
6	Schematic representation of the direct urea-to-hydrogen process [36].	24
7	Schematic system arrangement of UT-3 process [31].	26
8	possible production paths for commercial products	28
9	Simulated potential for switchgrass crop with one harvest per year[147]	29
10	Basic outline of the process turning biomass into biodiesel fuel	31
11	Volumetric energy density of alternative commercial fuels burned for energy[30]	31
12	Radial view of the core showing the layout of the fuel assemblies, control rods, reflector, and shield.	35
13	Table of important parameters for the reactor, still to be done are depletion calculations and kinematics	36
14	K-effective versus rod position for final core model	37
15	Thermal Conductivities for different materials in a fuel pin	38
16	Temperatures at different locations in the fuel pin with varying axial height. This is shown with the axially varying linear heat rate (in blue).	39
17	Sketch of model for LBE flow calculations	41
18	Mass flux through down channel given an outlet temperature of 650°C for varying inlet temperatures and values of D. Green represents D = 1 m, blue represents D = 2 m, and red represents D = 3 m.	42
19	Variation in Reynolds number for flow through down channel given an outlet temperature of 650°C for varying inlet temperatures and values of D. Green represents D = 1 m, blue represents D = 2 m, and red represents D = 3 m.	43
20	The axis going up the screen is mass flux (kg/s-m^2), the axis on the lower left side of the screen is inlet temperature ($^{\circ}\text{C}$), and the axis on the lower right side is outlet temperature ($^{\circ}\text{C}$).	44
21	Overview of the secondary system of the reactor	45
22	The nodal values of temperature, pressure, and mass flow for the secondary system	46
23	Printed Circuit Heat Exchanger (PCHE) Design	47
24	Geometry options for the in-reactor shell-and-tube heat exchanger.	47
25	An overview of the process heat system	51
26	Axial temperature profile of the hot and cold fluid and hot and cold channel walls	56
27	Heat flux profile for PCHE1	56
28	Minimum mass flux and flow quality in PCHE2	57
29	Axial temperature profile of PCHE2	58
30	Heat flux profile of PCHE2	59
31	The basic design of the storage heat exchanger	64
32	A view of the cross-sectional flow area of the storage heat exchanger.	65
33	The charging layout for the storage heat exchanger.	66
34	The storage loop during energy discharge.	67
35	The mass flow rate of the LBE as a function of time when the storage device discharges.	70
36	Helium Pipe Layout. Adapted from [87]	72
37	HTSE Hydrogen Production Plant	75
38	Power Requirement for Water Electrolysis [121]	78
39	SOEC schematic	79
40	Schematic of proposed biofuels production plant	83
41	Sites for switchgrass growth in the U.S.	84
42	Schematic of silvagas gasification process	86

43	Typical acid gas removal process after gasification of biomass without a combustion chamber	87
44	Amine Acid Gas Removal Process	88
45	LO-CAT acid gas removal process	89
46	Slurry phase bubble reactor schematic [100]	90
47	The effect of feed ratio $r = H_2/CO$ on selectivity at $T = 300^\circ C$ [100]	91
48	ASF distribution for chain growth [100]	92
49	Effect of catalyst concentration on conversion ratio	93
50	Effect of superficial velocity, catalyst concentration on the number of coolant tubes [122] . . .	93
51	Heat transfer coefficient as a function of catalyst concentration	94
52	Distiller Schematic	95
53	Bethel Low Temperature Fischer-Tropsch Refinery Design	96
54	Core house of quality	109
55	PCHE nodalization [54]	120
56	PCHE volume and heat transfer coefficient as a function of channel diameter	122
57	Reynolds number and Pressure drop as a function of S-CO ₂ mass flow rate	124
58	Heat transfer coefficients and PCHE volume as a function of S-CO ₂ mass flow rate	125
59	Map of biomass resources in Texas. Harris County is noticeable in dark green to the lower right. (National Renewable Energy Laboratory)	127
60	Silva gas and FICBC for product selectivity	130
61	Block diagram of the UT-3 plant.	134
62	Proposed Calcium Pellet Design [131]	135
63	The mixed conducting membrane process. O ₂ is separated from the steam mixture and diffused across as ions with the aid of a pump.	136
64	Hydrogen storage options with corresponding energy, operating temperature, and wt.% [123]	138

List of Tables

1	Power density comparison for different reactor types	12
2	Reactor Design Comparison[88, 139, 62, 49, 120, 44, 98, 126, 136]	16
3	Principal Features of Heat Exchangers (adapted from [133, 103])	17
4	Inputs and Outputs Comparison for Biofuel Production Processes	28
5	Comparison of Biomasses for Biofuel Production	29
6	Summary of turbine costs [54]	49
7	Fractional costs of the different supercritical CO ₂ cycle designs [54]	50
8	Potential Working Fluid Properties [18]	52
9	Summary of PCHE results	53
10	Potential Materials for PCHE	54
11	Impact of design parameters on PCHE volume and pressure drop	54
12	Steam/hydrogen and oxygen streams from the hydrogen plant	60
13	PCHE capital cost	62
14	Relevant physical properties of LiCl	63
15	The composition of Alloy 20. Adapted from [11].	64
16	A summary of the heat storage results	70
17	Losses through helium transport pipes	73
18	PCHE capital cost	73
19	SOEC Outlet Mass Flows	76
20	Summary of options for solid electrolyte materials	80
21	Mass distributions of wood and switchgrass [39]	86
22	Composition of Syngas Output from Silvagas Gasifier [118]	87
23	Composition of Syngas Output after Acid Gas Removal	89
24	Products of Fischer-Tropsch Process and Relative Boiling Points	94
25	Straight channel and zigzag channel PCHEs	121
26	Hydrogen Production Rates and Thermal Power Requirements	133
27	Comparison of CVD (TEOS) and Zr Silica ceramic membranes	135

Part I

Introduction

The political and social climate in the United States is making a transition to one of environmentalism. Communities are demanding green energy produced in their own country in order to curb global warming and dependency on foreign energy suppliers. Because of these trends, the overall design problem posed to the 22.033 Fall 2011 class is one of a green energy production facility. This facility was constructed to contain a nuclear reactor, a hydrogen production plant, and a biofuels production plant. This design was chosen so the reactor can provide heat and electricity to supply both hydrogen and biofuel production plants their necessary input requirements. Since nuclear power can also provide much more energy, a clean form of electricity can then be sold to the grid. The hydrogen production plant's main goal is to provide enough hydrogen to power a biofuels production cycle. In order to make this plant more economically feasible and in line with the green energy goal, no extra hydrogen will be sold. Instead, their sole purpose will be to supply the biofuels facility with as much hydrogen is required. In turn, the biofuels production plant will produce bountiful biodiesel and biogasoline for sale to the public.

Due to the complexity of this plant, the design work was subdivided into four groups: (1) Core, (2) Process Heat, (3) Hydrogen, and (4) Biofuels. The core group was responsible for creating a reactor design (including primary and secondary systems) that could power hydrogen and biofuel production plants with both electricity and heat in addition to selling any additional electricity to the grid. The process heat group was responsible for transferring the heat provided by the reactor to the hydrogen and biofuels facilities (in addition to wherever else heat was needed). The hydrogen group was responsible for receiving the core heat from process heat and creating enough hydrogen to power the biofuels process, if not more. The biofuels group was responsible for taking that hydrogen and process heat and creating biodiesel and biogasoline for sale to the general public. There were two integrators to the combine the design work from all four groups and present a cohesive green energy facility.

This design is quite significant because the world is starting to turn towards green production and in order to meet people's growing energy needs, large, clean electricity and gasoline generating plants will need to be built. Facilities that produce both carbon-emission-free electricity and fuel will hopefully become a rising trend to help combat global warming and other increasingly alarming environmental concerns.

Part II
Background

1 Core

1.1 Main Goals of the Core Group

The overall goal of the project was to prove that nuclear plants can work in tandem with hydrogen and biofuels production and furthermore that the potential reactor types are not just limited to high temperature gas reactors but can also work at lower temperatures, such as those produced by liquid salt and metal cooled reactors. With those overarching goals in mind, the primary goals of the core group were to design a reactor with:

- sufficiently high outlet temperature to be useful for process heat applications
- capability to produce sufficient electricity to supply overall plant needs or at least 100 MWe
- technology that is a viable alternative to the current commercial reactor fleet
- a good chance at being approved and built within the next few decades

The high outlet temperature is necessary for hydrogen and biofuel production and is the most limiting factor in choosing reactors. The goal of being capable of producing at least 100 MWe was necessary only to insure proper sizing of the reactor. A reactor not capable of producing this amount of electricity would not be able to supply the amount of process heat needed. A large reactor design was chosen, because these are the designs most likely to be approved for construction in the upcoming decades. Showing the profitability of using a nuclear plant that is already being considered for construction for biofuel production adds extra incentive to construct such designs. A viable reactor has to be both technically feasible and stand a reasonable chance at being licensed and built. Extremely exotic core designs were thus excluded because of the unlikeliness that such designs would be built or licensed in the near future. In the end, the design chosen, a lead-bismuth eutectic (LBE) cooled fast reactor with a supercritical CO₂ (S-CO₂) secondary cycle, provides a reactor that has a viable chance at being approved and constructed in the coming decades and also provides a high temperature alternative to current light water technology. The overall design, not just the reactor plant, proves that reactors of this type can work profitably with biofuels production. Furthermore, other reactor types with similar or higher outlet temperatures can be extrapolated to be profitable as well.

1.2 Design Parameters

When considering which design to pursue, many factors were important. In order to help sort through the different parameters the group used the Quality Functional Deployment method (QFD) and in particular a house of quality. An explanation of this method and the house of quality constructed can be seen in Appendix X.

The parameters outlined in the following sections were the primary differentiating factors between different designs and were what guided the choice of reactors. They are also in the house of quality constructed for this decision. Other factors that are not explicitly listed here were either not of significant concern or were not factors that differentiated one reactor from another.

1.2.1 Biofuels Coordination

Certain reactor types would not be compatible with the hydrogen and biofuel production processes described later in the report. This is because if the outlet temperature of the working coolant was too low, it would become impractical to heat it up for use. However, certain designs that have garnered a lot of attention as potential candidates to be used in the coming decades to replace existing reactors are liquid metal fast reactors, including sodium and lead cooled reactors. These reactors operate at much higher temperatures than typical light water reactors (LWR) and, while falling short of the optimal temperature, still produce high enough temperatures to be compatible with the biofuel and hydrogen processes. Furthermore, it would be beneficial if the nuclear plant took up as little physical space as possible so as to integrate well with the other plants on site. These two design parameters are described in more detail below.

	Power Density (MW/m ³)		
System	Core average	Fuel Average	Fuel Maximum
HTGR	8.4	44	125
PTGR	4.0	54	104
CANDU	12	110	190
BWR	56	56	180
PWR	95-105	95-105	190-210
LMFBR	280	280	420

Table 1: Power density comparison for different reactor types

1.2.1.1 Reactor Outlet Temperature

The major design parameter considered was reactor outlet temperature. The temperatures that the reactor must supply to the hydrogen and biofuel plants quite substantial ($>700^{\circ}\text{C}$) and the current reactor fleet (except for gas reactors) cannot achieve those temperatures. High temperature gas reactors provide optimal temperatures, but as will be seen later on, fall short in many other categories and thus were not the de facto reactor of choice. A temperature close to the requirements could suffice with extra heating coming from other means (either electrical or by burning excess hydrogen or biofuels). The final design chosen, was LBE cooled fast reactor with a S-CO₂ secondary loop. This design has an outlet temperature of 650°C .

1.2.1.2 Footprint of the Reactor

A design parameter that the group considered important was size of the overall reactor plant. It was felt that a smaller reactor plant would make construction cheaper and would allow more flexibility when choosing a location for the plant. With biofuels and hydrogen plants that would also be present, having a smaller plant would be useful so as to limit overall size of the facility. A small reactor plant also allows for more flexibility in how the reactor can be used independent of the hydrogen and biofuels production plants. It can be used in locations where space is limited such as ships, densely packed nations, etc. The LBE cooled reactor had a higher power density and was physically smaller compared to other plants [88] as shown in Table 1.

This was aided by a liquid metal coolant (which allows for greater heat removal per volume and thus more power production per volume) and by a secondary S-CO₂ cycle [54]. The secondary S-CO₂ using a Brayton cycle offers a smaller plant than the typical Rankine steam cycle primarily because of the decrease in size of the turbines [54].

1.2.2 Viability to get Licensed and Built in the Upcoming Decades

As mentioned previously, the viability of the reactor is a critical goal to the project. Liquid metal fast reactors, both sodium and lead cooled, have been built and operated in the past, for example at Dunreay in Scotland for sodium and on Soviet submarines for lead, and thus have proven track records when it comes to technical viability. While some of those designs, notably the sodium cooled Superphenix, have faced problems, experience with these reactors and decades of design optimization have led to more stable and promising designs. Still, the question arose as to how difficult the licensing process would be for designs that the Nuclear Regulatory Commission (NRC) is unfamiliar with. None of the reactors under consideration had much in way of a recent predecessor that the NRC had dealt with. Therefore, the primary thought process was to examine each design from the viewpoint of a regulator and see which reactor would have the easiest time getting through licensing. A design such as the molten salt reactor (MSR) would be very difficult to get licensed (even though reactors have been built of this type in the United States, albeit a while ago [70]) because of the uneasiness of molten fuel paired with a toxic coolant. Similarly, a reactor such as the Sodium Fast Reactor (SFR) would be faced with a problem in regards to preventing its coolant coming into contact with any water or air because the coolant then reacts violently. Lead reactors face problems in keeping the coolant from solidifying and also face toxicity issues. The secondary loop is one facet of the design that is chosen where it adds to the difficulty in the plant licensing because there is no experience with S-CO₂ in a nuclear reactor in the US. Nevertheless, CO₂ is very inert and, if released, would cause little issue.

1.2.2.1 Safety

Some of the designs possess operating characteristics and materials that offer significant performance advantages at the cost of safety. For the chosen LBE-cooled design, one safety concern was that the bismuth could be neutronically activated. This was deemed to be a minor concern for two reasons. First, proper shielding could minimize worker dose due to bismuth activation. Second, the coolant is made of lead and bismuth, both high-Z elements, which results in an excellent built-in gamma shield.

With any fast reactor, a positive void coefficient of reactivity is a concern and the design proposed in this study is no different. One safety advantage is that LBE takes a considerable amount of heat to boil and the moderation provided by the lead-bismuth is miniscule. Therefore, the low possibility of coolant voiding was deemed a minor concern. Furthermore, a LBE cooled core can be designed for natural convection circulation cooling which is an excellent passive safety feature that should aid in loss of off-site power accidents that have recently (because of the Fukushima accidents) been focused on. The final design utilized this safety advantage.

1.2.2.2 Simplicity of Design

Minimizing the amount of structures, systems, and components (SSCs) is beneficial in reducing construction and capital costs. A simple design allows for simple operation, less parts to maintain, and less opportunity to overlook an issue. Therefore reactor designs were also vetted based on how complex the design would be. For example, having an intermediary loop or an online reprocessing plant added to the complexity of the reactor. The range of designs considered went from simple single fluid designs such as Supercritical Water Reactors (SCWR) to SFRs containing three interfacing coolant systems and MSR containing a on-line reprocessing plant. The final LBE cooled design utilized a primary coolant system of LBE and a secondary coolant system of S-CO₂, similar to current pressurized water reactors (PWRs) in the sense that both use a primary and secondary coolant.

1.2.2.3 Material Concerns

In any reactor, material stability and corrosion resistance are important considerations. In the high operating temperatures that are being employed in this plant design, the ability of the materials to be able to withstand such an environment became a significant concern. In fact, all high temperature designs considered faced material corrosion concerns. The final LBE cooled design also faced corrosion issues and was in the end limited by creep lifetime. Current optimization of this design includes searching for a material capable of handling the high temperature environment for longer periods of time. Currently, there is a large push in research to find materials capable of handling these environments which bodes well for high temperature reactors.

1.3 Design Options and Evaluation

1.3.1 Liquid Metal Fast Reactors

Liquid metal reactors, including the SFR and the Lead Fast Reactor (LFR) are among the most viable high temperature designs. Most current SFR and LFR designs have outlet temperatures of about 550°C [150] though these designs have the capability to go to higher temperatures. From the literature, it seems that an outlet temperature of 550°C was chosen to match reactors to readily available turbines with well known performance histories [150]. Given that, this suggested higher temperatures may be possible, further research was done on the fundamental material concerns with SFR or LFR operation and how these might contribute to a hard maximum temperature. It was found that both sodium and lead cores and coolant could operate at higher temperatures, but current cladding is the limiting factor. Cladding begins to creep and eventually fails at temperatures around 650°C [150]. Because of this limit, the average temperature of the cladding is kept below 550°C. Materials research to push this boundary seems most developed for LFR materials, with the US Navy in particular believing that outlet temperatures could approach 800°C within the next 30 years [57].

The feasibility of LFRs operating at these temperatures is supported by the significantly higher boiling point of lead (1749°C as opposed to 883°C for sodium) which would protect against voiding and thus ensure

sufficient cooling of the fuel in the event of accident scenarios and protecting against other dangerous transients. Having a small, safe, and economically competitive reactor with a suitable outlet temperature would be most appealing to any potential clients. The LFR meets these requirements well and aligns with these QFD criteria, see Appendix X. The possible exception to this may be the LFR's economic competitiveness, given the high costs of building any new reactor design, although burning actinides or having a positive breeding ratio may change this. These two processes would allow the reactor to be fueled using relatively low uranium enrichment (with as low as 11% enrichment being reported for U-Zr fueled SFRs [97]) thus allowing fuel to be bred in the reactor during operation and reducing costs. This may eventually lead to the possibility of fast reactors, including LFRs, being deployed with a once-through fuel cycle and having economics near that of current once-through LWR reactors [97]. LFR reactors can have small footprints due to the density and thermal conductivity of the lead coolant, which will be useful in this project given that the hydrogen and biofuel plants may be very large, reducing the impact of the facility as a whole as well as making the reactor more secure. LBE, with a melting point of 123.5°C, was chosen as the final coolant choice because it offers a lower melting point than lead and generally does not expand or contract much with cooling or heating [3]. However, it can produce a dangerous radioisotope of polonium [3], and thus additional operational handling procedures would need to be followed to ensure the safety of the workers.

1.3.2 Molten Salt Reactors

The next design investigated was the MSR. This reactor design is capable of the requisite temperature and has additional features that are quite attractive for the plant needs. One of these features is the ability to scale the reactor to any size, allowing flexibility during future design iterations [126]. Using both a graphite moderator and a molten-salt coolant, this reactor also does not require pressurization thus eliminating equipment costs and providing added safety. In the case of an accident where the core overheats, a safety plug would drain the molten core into a sub-critical geometry, ending threat of a criticality incident before an accident escalates. As a fuel, the MSR would need to use medium-enriched uranium, but was also compatible with a thorium fuel cycle. This would reduce fuel costs substantially because of the great abundance of thorium as compared to uranium[74]. Some disadvantages of the MSR include the presence of hazardous materials in the reactor vessel and salt. A salt being considered for extensive use is FLiBe, which contains beryllium and poses a risk to workers on the premises. A second concern is the production of hydrogen fluoride (HF) in the core, which is lethal if it comes in contact with human tissue {ToxicSubstances2003}. Additionally the hydrogen bonding to the fluoride in the HF is tritium, a dangerous radioactive isotope. Depending on the fuel chosen, it could add proliferation concerns due to the reprocessing of the fuel on-site. A thorium fuel cycle would eliminate the potential production of plutonium and is advantageous in that respect. Though the MSR had some potential for the project, it was not as practical or effective as some of the other designs considered.

1.3.3 Gas Cooled Reactors

The Advanced Gas Reactor (AGR), High Temperature Gas Reactor (HTGR), Pebble Bed Modular Reactor (PBMR), and Very High Temperature Reactor (VHTR) gas-cooled reactors operate with a thermal neutron spectrum and are moderated with graphite. The HTGR, PBMR, and VHTR all use helium as their primary coolant and the AGR design uses CO₂. The designs do differ in their operating temperatures, however, all of these designs operate at significantly higher temperatures than traditional PWR or boiling water reactors (BWRs). The PBMR specifies that the fuel is contained within small, tennis-ball-sized spheres, which is one of the fuel options for the HTGR or the VHTR. Besides these “pebbles,” the other fuel option for these reactor types are small cylindrical compacts, which can then be compiled to form more a prismatic reactor core [62]. For either the pebble or the compact fuel design, the fuel starts as tiny particles of uranium dioxide (UO₂) or uranium carbide (UC) and is then coated with layers of carbon and silicon carbide (SiC). These layers form the tri-isotropic (TRISO) fuel particles that can be assembled into either the pebble or compact form for the fuel.

The TRISO fuel particles provide these gas reactors with several passive safety features. In the event that there was a loss of coolant accident, the refractory materials of the coating (the carbon and the silicon carbide) would be able to contain the radioactive material. Additionally, in a loss of flow accident (LOFA) or a loss of coolant accident (LOCA), the large amount of graphite in the core would be able to absorb a significant amount of heat and avoid melting of the reactor fuel [62, 88]. The high temperatures of the VHTR

in particular allow for high efficiency and has been noted for its compatibility for hydrogen production, the end goal of the process heat for our overall design. While the gas reactors had ideal temperatures for our design, other concerns, notably the size and economics/viability of one being built prevented these reactors from being chosen.

1.3.4 Supercritical Coolant Reactors

The SCWR operates at high pressure and temperature (25 MPa and 550°C) and use water in supercritical state (neither a liquid nor a gas, but with properties of both) as the coolant [49]. Such reactors could operate on either a fast or thermal neutron spectrum. A SCWR resembles a BWR in design but differs in the conditions it operates under. Supercritical water has excellent heat transfer properties compared to normal water and thus less coolant flow is needed for the core than the BWR. There also exists a large temperature change across the core (greater than 200°C). Due to the high temperatures and use of the Brayton cycle, this plant has excellent thermodynamic efficiencies on the order of ~45% [49]. The design for a typical SCWR is simple, much like BWRs, with one loop (although a SCWR of equal power would be smaller than a BWR). SCWRs have no risk of boiling and can achieve high electric power levels (1700 MWe). Furthermore, there is a significant amount of experience with supercritical water in fossil fuel plants {Alstom}, but not in a neutron irradiation environment. These conditions along with the high temperatures also give rise to significant materials concerns and there is some difficulty achieving a negative void coefficient, particularly with fast designs.

Supercritical D₂O (S-D₂O) Reactors are under consideration in Canada [44] at the moment. They can use thorium as a fuel in a fast reactor, otherwise, there is limited difference between these and SCWR. Supercritical CO₂ reactors use S-CO₂ as the primary coolant. S-CO₂ has a number of advantages over supercritical water [120] including:

- It requires a lower pressure (7.4 MPa vs. 22.1 MPa) to keep critical, and thus operates at a lower pressure (20 MPa vs. 25 MPa)
- It is better suited for fast reactors because of the absence of the strong hydrogen moderator that water has
- It has the advantage of having a turbine rated at 250 MWe that has a diameter of 1.2 m and a length of 0.55 m (supercritical water uses turbines sized similarly to current LWR technology)

For all these reasons, S-CO₂ is attractive for a consolidated reactor plant. Much research has been done on its use as a secondary coolant in an indirect cycle with lead or molten salt and the decision was made to use this as our secondary coolant for a number of reasons including:

- Small footprint
- Excellent heat transfer properties
- Excellent thermodynamic efficiency
- Lower required pressures than supercritical water

1.3.5 Table of Design Comparison

	SFR	LFR	VHTR	MSR	SCWR
Neutron Spectrum	Fast	Fast	Thermal	Fast or thermal	Fast or thermal
Outlet Temp. (°C)	530 to 550	near-term: 550-650 long-term: 750-800	>1000	650	550
Coolant	Na	Pb or LBE	Helium (CO ₂)	FLiBe	S-H ₂ O CO ₂ , D ₂ O
Moderator	None	None	Graphite	Graphite	Same as coolant
Relative Power	High	High	Medium to High	High	High
Power Density	High	High	Low	N/A	Low to Med.
Feasibility	Med.	Med.	Low to Med.	Low to Med.	Med.
On-line Refueling	No	No	Yes	Yes	No
Fuel Enrichment	MEU to HEU	MEU	LEU to MEU	LEU	LEU or nat U
Pressure	~ 1 atm	~ 1 atm	depends	~ 1 atm	20-25 MPa
Price	Above Avg.	Above Avg.	Above Avg.	High	Below avg.
Physical Size	Below Avg.	Small	Very Large	Large	Average
Materials Concerns	neutron activation Na reactive w/air & water	need to melt coolant Po creation with LBE	high temp concerns molten salt can be corrosive	molten fuel FLiBe dangers (Be/tritium/HF)	supercritical fluid
Other Notes	Actinide management	Can't void coolant LBE has good thermal properties Pb/LBE are not reactive w/water	Coolant remains single phase Using He reduces corrosion	on-line reprocessing	similar to current BWR designs

Table 2: Reactor Design Comparison[88, 139, 62, 49, 120, 44, 98, 126, 136]

2 Process Heat

2.1 Goals of the Process Heat Design Group

A lead-bismuth cooled reactor with a secondary loop of S-CO₂ has been chosen as the heat source for this facility that will couple the reactor with a hydrogen and biofuels plant. The heat provided by the reactor will be transported to the hydrogen and biofuels facilities with minimum temperature and pressure losses. The process heat system will consist of high temperature heat exchangers (HX) in the secondary loop, heat exchangers at the biofuels and hydrogen plants, a heat storage system and piping connecting all these components. Various heat sink options are also under consideration. The goal of the process heat subgroup was to determine an optimal layout design from the various types of technology available to fulfill the three main tasks of exchanging, transporting, and storing heat. Once this has been completed, the objective is to size and model these components based on the operating conditions and heat requirements of the reactor, biofuels, and hydrogen plants.

2.2 Design Challenges

Overarching process heat issues include working with large temperature gradients, minimizing heat and pressure losses, and choosing robust components. A major design challenge is the fact that the core is outputting a temperature on the order of 650°C which is significantly lower than the input temperature needed to power some of the hydrogen production processes. In addition, it was determined that a heat storage device would be implemented in order to heat the lead-bismuth coolant to a point just above its melting temperature during the event of a shutdown.

It is imperative that the materials chosen for fabricating heat exchangers for the process heat system are able to withstand operating conditions of high temperatures (up to 900°C) and pressures (up to 5 MPa). Susceptibility of candidate materials to stress corrosion cracking under constant load as well as slow-strain-rate conditions, fracture toughness, and crack growth behavior have been studied extensively and literature indicates that Alloy 230 and Alloy 617 are suitable for fabricating high temperature heat exchangers [72]. The operating conditions for the heat exchanger at the hydrogen plant will be more severe due to temperatures higher than the core outlet temperature. Studies indicate that Alloy C-22 and Alloy C-276, because of their high tensile strength and ductility until fracture, are suitable heat exchanger materials for operation in or near acidic environments [127].

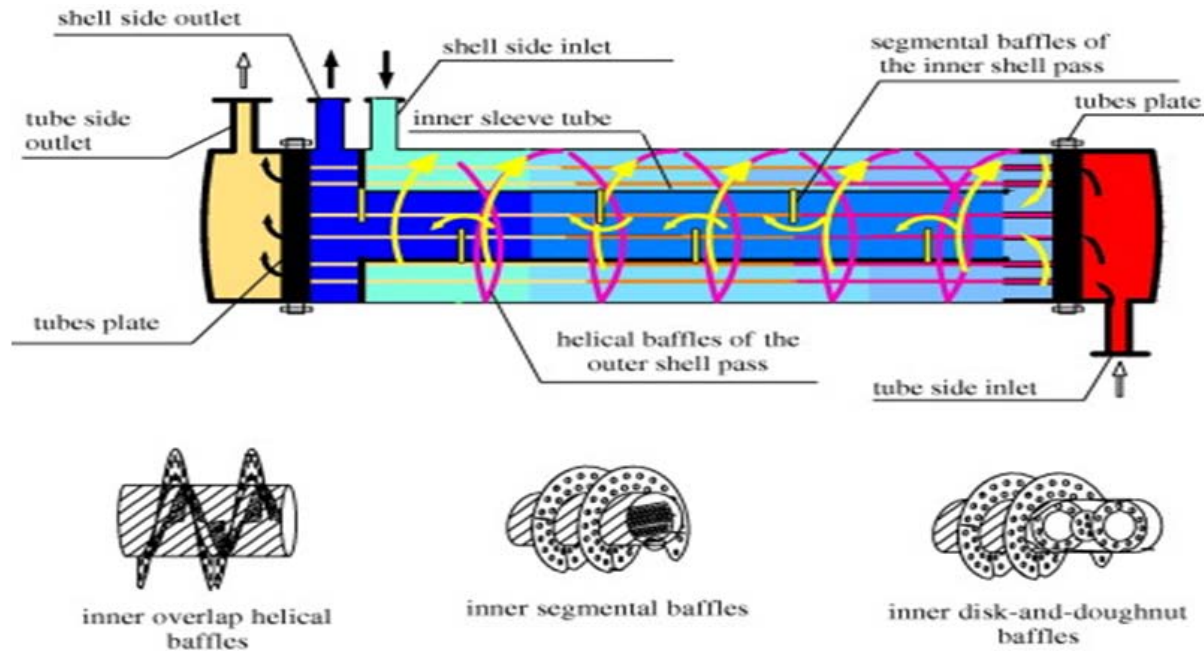
2.3 Possible Heat Exchanger Designs

The applicability of heat exchanger (HX) designs to this system was evaluated based on the feasibility of the heat exchanger technology as well operating temperatures and pressures. Effectiveness, size, heat transfer area per unit volume, working fluid options, heat losses and pressure drops for the various designs were also primary considerations. However, several of these considerations have conflicting implications for HX design. For example, compact heat exchangers (such as the PCHE discussed below) have high effectivenesses and heat transfer coefficients but incur larger pressure losses.

The principal features of five HX designs - shell and straight tube, shell and helical tube, plate, and printed circuit and ceramic heat exchangers- are listed in Table 3.

HX Type	Compactness (m ² /m ³)	Temp. Range (°C)	Max P (MPa)	Multi- stream	Multi- pass	Cleaning Method
Straight Shell-and-Tube	~100	~+900	~30	No	Yes	Mech, Chem
Helical Shell-and-Tube	~200	~600	2.5	No	No	Mech
Plate	~200	-35 to ~+900	~60	Yes	Yes	Mech, Chem
Printed Circuit	2000 to 5000	-200 to ~+900	~60	Yes	Yes	Chemical
Ceramic Heat Exchangers	N/A	1200	N/A	yes	yes	Mech, Chem

Table 3: Principal Features of Heat Exchangers (adapted from [133, 103])



Courtesy of Elsevier, Inc., <http://www.sciencedirect.com>. Used with permission.

Figure 1: Combined Multiple Shell-Pass Shell-and-Tube Heat Exchanger (CMSP-STHX) with continuous helical baffles [158]

2.3.1 Straight Shell-and-Tube

Shell-and-tube HXs find extensive application in nuclear plants and process heat systems. These HXs can be designed to be robust and suitable for special operating conditions such as a radioactive environment. They can be fabricated using Hastelloy, Incoloy or graphite and polymers [102]. The design can be adapted to include fins if one of the working fluids is a gas as the heat exchanger allows liquid/liquid, gas/liquid, and two phase systems. These heat exchangers are very large due to low heat transfer area per unit volume ($\sim 100 \text{ m}^2/\text{m}^3$) but allow high operating temperatures (up to 900°C) and pressures (up to 30 MPa) [133].

2.3.2 Modified Shell-and-Tube

Helically baffled Straight shell-and-tube heat exchangers can be modified by introducing multiple passes, or pathways for the liquid as well as by adding baffles. Baffles are flow-directing panels within the tube that increase the efficiency of heat transfer. Typical segmental baffles are perpendicular to the tube and can result in dead zones with lower local heat transfer. Helically baffled shell-and-tube heat exchangers, due to their geometry, are able to induce turbulent flow and therefore increase heat transfer rates. This turbulence combined with the high shear stress makes the helical shell-and-tube exchanger less likely to experience disruptive fouling. A helically baffled shell and tube HX is shown in shown in Figure 1.

Another advantage of the helical baffle is that it reduces vibrations within the heat exchanger (because the fluid is crossing the tube bundle at an angle instead of vertically) and therefore increases the heat exchanger's physical stability. Helical heat exchangers can operate at large pressures and are expected to withstand a maximum pressure of 70 MPa [95]. A recently published paper [158] numerically assesses the benefits of a combined multiple shell-pass shell-and-tube heat exchanger with continuous helical baffles (CMSP-STHX) as shown in Figure 1. In their reference system (and in the majority of systems to date) the inner shell pass uses standard segmental baffles while the outer shell pass uses continuous helical baffles. This is due to the difficulties in manufacturing helical baffles in the smaller central shell. Despite this, it was found that with the same mass flow rate and heat transfer as a conventional shell-and-tube heat exchanger with segmental baffles (SG-STHX), the helical version experienced a pressure drop 13% lower than that of the standard heat exchanger. If the pressure drop was held constant, the helical HX was capable of a 6.6% higher mass flow

rate and a 5.6% higher heat transfer rate than the standard heat exchanger [158].

Helical tube The shell and helical tube HX is a variation on the shell and straight tube design and consists of tubes spirally wound and fitted in a shell. Spiral tube geometry provides a higher heat transfer area per unit volume ($200 \text{ m}^2/\text{m}^3$ compared to $100 \text{ m}^2/\text{m}^3$ for straight shell-and-tube type HXs). This design has been proven by its use in the High Temperature Engineering Test Reactor (HTTR) [64]. Helical type HXs are well suited to gas/liquid systems. A disadvantage of this design is the difficulty in maintenance of the helical coils [133, 129]. These heat exchangers find extensive application in nuclear plants and also as process heat systems and can be designed to be very robust and suitable for special operating conditions such as a radioactive environment. They can be fabricated using Hastelloy, Incoloy, graphite and polymers [102]. The design can be adapted to include fins if one of the working fluids is gaseous and the heat exchanger allows liquid/liquid, gaseous/liquid as well as two phase systems. These heat exchangers are very large due to low heat transfer area per unit volume ($\sim 100 \text{ m}^2/\text{m}^3$) but allow high operating temperatures (up to 900°C) and pressures (up to 30 MPa).

2.3.3 Plate

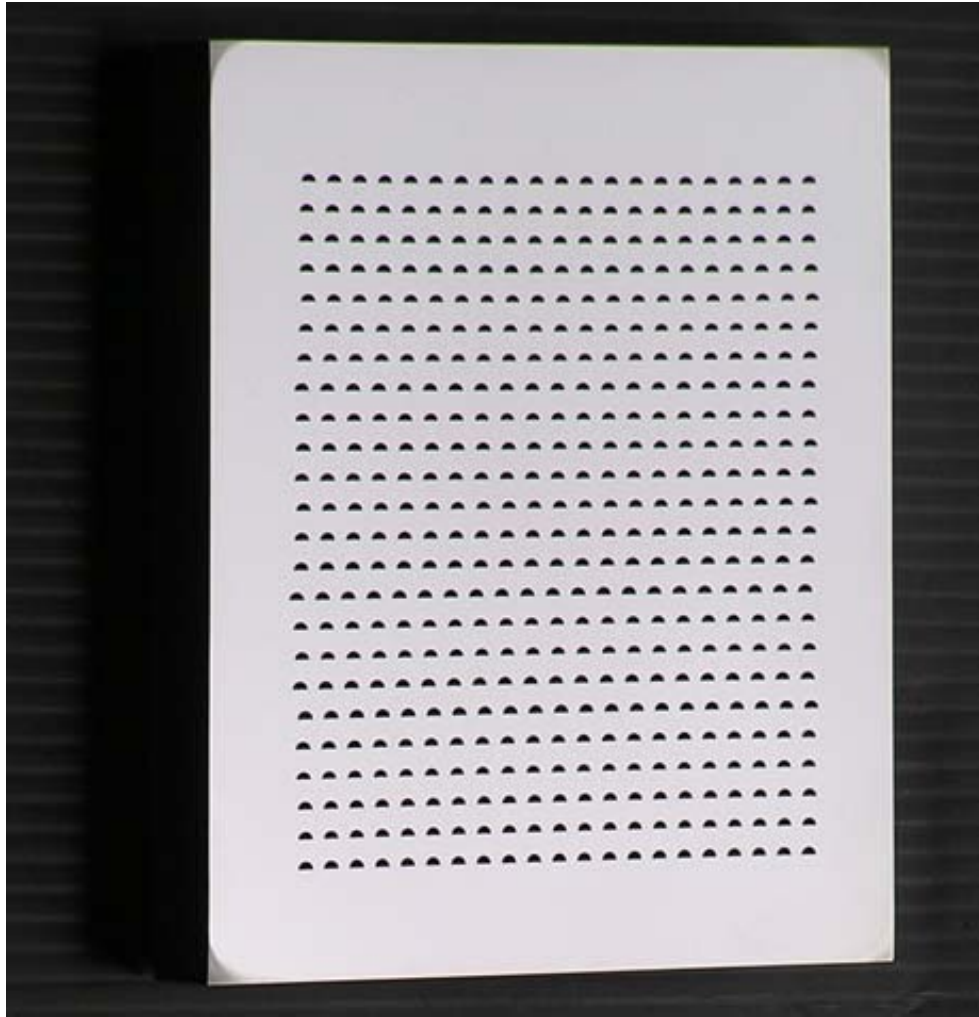
In a plate type heat exchanger, the heat transfer occurs through planar surfaces which allows counter, cross, and parallel flow configurations [135] and can be fabricated from Hastelloy and nickel alloys. These heat exchangers, however, allow both multi-pass and multi-stream capabilities and greatest ease of cleaning and maintenance as compared to the other designs reviewed for this project. There are several variations on plate type designs, however, the Bavex plate HX provides the highest operating temperatures (up to 900°C) [133, 129].

2.3.4 Printed Circuit

PCHEs (an example of which is seen in Figure 2) can operate under high temperature ($\sim 900^\circ\text{C}$) and high pressure ($\sim 60\text{MPa}$) conditions. They are typically used in petrochemical, refining, and upstream hydroprocessing industries. PCHEs can incorporate multiple process streams into a single unit and have low mass/duty ratios of $\sim 0.2 \text{ t/MW}$ [16]. They are suitable for corrosive environments and have an effectiveness of up to 98%. In a PCHE, the fluid flow channels, which are of the order of several millimeters, are chemically etched and the flow can be parallel, cross, counter flow, or a combination of all three. Also, the absence of gasket and braze material lowers the probability of leakage [99]. However, there is potential for thermal stresses in the axial direction when there are sharp temperature variations. This design also suffers from low capacity factors due to the need for offline inspection and repairs [111]. Furthermore, small flow channels could result in fouling problems which would require offline repairs using chemical methods [133]. However, redundant modules may be installed to improve capacity factors of the process heat system during maintenance and repairs. PCHEs have not been used previously for nuclear applications, but are under reviews as potential HXs for the Next Generation Nuclear Plant [124].

2.3.5 Ceramic

A multi-stream heat exchanger capable of operating at high temperatures in the presence of both reducing and oxidizing fluid streams is required at the Biofuels plant. This HX will be required to draw heat from waste hydrogen and oxygen fluid streams to produce steam. Ceramic heat exchangers fabricated from reaction bonded silicon carbide (RBSiC) or siliconized silicon carbide (SiSiC) are best suited to this application. Both ceramic materials have lower thermal conductivities than Ni-Cr alloys used for fabricating HXs discussed earlier in this section. However, unlike metal alloys both RbSiC and SiSiC have demonstrated resistance to oxidative and reductive environments at temperatures up to 1200°C [103]. Multi-stream cross-flow heat exchangers can be fabricated using either ceramic material.



Source: Li, Xiqing., et al. "Alloy 617 for the High Temperature Diffusion-Bonded Compact Heat Exchangers." Published in ICAPP 2008, Anaheim, CA, June 8-12, 2008. © American Nuclear Society and the authors. All rights reserved. This content is excluded from our Creative Commons license. For more information, see <http://ocw.mit.edu/fairuse>.

Figure 2: A PCHE heat exchanger made of Alloy 617 with straight channels [160]. The semi-circular fluid channels have a diameter for 2mm.

3 Hydrogen

3.1 Goals of Hydrogen

The hydrogen production plant was implemented in this design to partly satisfy the overall goal of designing a nuclear system that can produce at least 100 MWe and produces hydrogen and biofuels. Before the choice of the hydrogen production method could be made, the purpose of the hydrogen production plant had to be determined. The plant would either provide hydrogen for use in a large scale hydrogen economy or only would provide the necessary hydrogen input for the biofuel production plant. Hydrogen is currently used in the petroleum and chemical industries; however, a large-scale hydrogen infrastructure involves hydrogen becoming the main source of energy for transportation in an effort to offset oil consumption and curb greenhouse gas emissions. However, research has shown that the chemical properties and costs of building a hydrogen infrastructure currently make a hydrogen economy unfeasible [37, 66]. Contrarily, biofuels can be distributed using presently available distribution infrastructures. Also, biofuels can be used while blended with traditional gasoline in slightly modified internal combustion engines, or in new engines that can run solely on biofuels [29]. In an effort to immediately impact oil consumption and reduce greenhouse gas emissions in an economical fashion, the purpose of the hydrogen plant was deemed as supplying only the amount of hydrogen required for the biofuel production facility.

With the purpose of the hydrogen production plant determined, the main design considerations used to compare different hydrogen production methods are as follows. The biofuel production plant requires 7.9 kg/s (682,560 kg/day) of hydrogen to achieve the desired biofuel production rate, and thus 7.9 kg/s was the hydrogen production quota imposed on this design. In an effort to minimize greenhouse gas emissions in this nuclear reactor system overall, a hydrogen production process that produces no net greenhouse gases was desired. Also, the objective to minimize power consumption was used to guide design choices, especially to minimize steady-state electrical power consumption since it is less energy efficient than using solely thermal power while considering the thermodynamic efficiency of converting heat into electricity of ~45%. The lead-bismuth nuclear reactor exit temperatures are ~600C, and thus hydrogen production methods that are able to operate closest to this temperature are preferable. This design consideration is motivated by the previously stated objective to minimize steady-state electrical power consumption. If maximum temperature requirements are higher than the available thermal temperatures of approximately 600 C, then additional electrical power will be required to raise the temperature of reactants so chemical processes proceed properly. Also, maximum temperature requirements coupled with the type of reactants involved in each hydrogen production method were considered, motivated by the tendency for greater material degradation concerns in corrosive, high-temperature environments. If these material concerns were not sufficiently mitigated, they would jeopardize the reliability and longevity of the hydrogen production plant. The requirement to replace components frequently would negatively effect both the economics of the hydrogen plant and also jeopardize consistent biofuel production capabilities. Lastly, the commercial viability of each hydrogen production approach was considered, such that scalability to hydrogen production quotas was conceivable and that the scaled power requirements from previous studies were favorable relative to the total thermal and electrical output of the lead-bismuth nuclear reactor used in this design. All of these design objectives and considerations were used to guide the design choices of choosing a hydrogen production method to reach a 7.9 kg/s hydrogen production rate required by the biofuel production plant.

3.2 Design Options and Evaluation

A total of eight options were explored, both thermo-chemical and electrochemical, to identify the optimal process for hydrogen production. Four major hydrogen production methods were investigated: water electrolysis, high-temperature steam electrolysis, thermochemical water splitting, and bacterial hydrogen production. Other hydrogen production methods using natural gases were quickly rejected due to the design objective to use a hydrogen production method that partly fulfills the overall design goal of minimizing greenhouse gas emissions from this nuclear system design. Material concerns dominate the high temperature steam electrolysis and thermochemical water splitting due to relatively high temperatures (500-900°C) and corrosive reactants and products. However, the water electrolysis and bacterial hydrogen production process are dominated by commercial viability concerns.

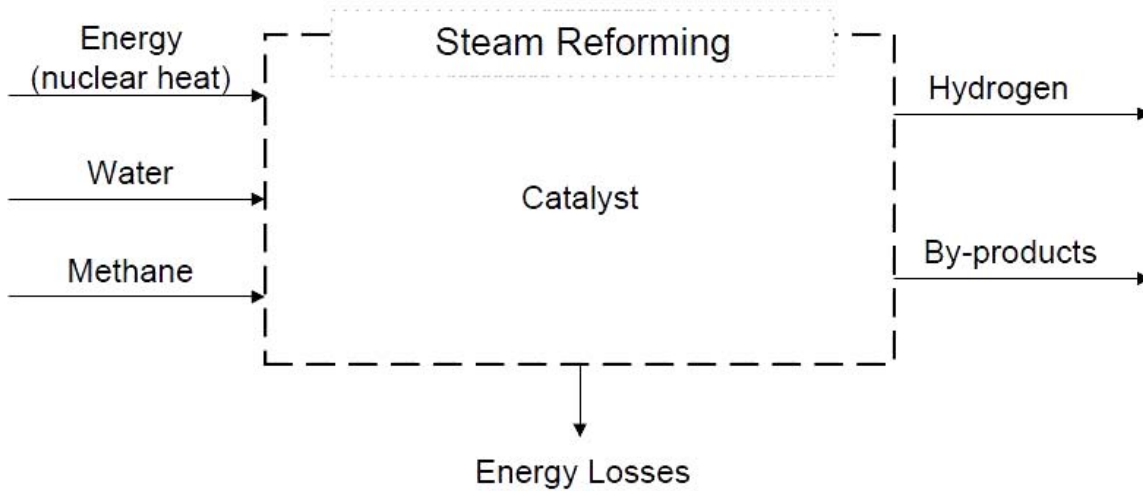


Figure 3: Steam methane reforming block diagram [48]

3.2.1 Steam-Methane Reforming

Steam reforming of natural gas (as shown in Figure 3) is one of the most widely used in industry today for chemical manufacturing and petroleum refining. Steam reforming first converts methane into hydrogen and carbon monoxide by a reaction with steam over a nickel catalyst. In a second step known as a water gas shift reaction, the carbon monoxide from the first reaction is reacted with steam to form hydrogen and carbon dioxide [125]. The chemical reactions can be seen in Equations 1 and 2.



These reactions occur at 750°C for Equation 1, which is a little high but within an acceptable range, and 350°C and below for Equation 2, which is well within the acceptable range. Steam reforming is about 70% efficient, which is an advantage [89]. However, despite the efficiency, input temperature, and proven feasibility of the technology, steam methane failed the most critical parameter, which was to be carbon emission-free, because it produces CO_2 . For this reason, SMR was one of the first production options to be discarded.

3.2.2 Water Electrolysis

Electrolysis produces hydrogen by passing electricity through two electrodes in water. This causes a dissociation of H_2O as H^+ and O^- travel to the cathode and anode respectively to form H_2 and O_2 . Two distinct categories of electrolysis units are presently used for industrial production of hydrogen: alkaline electrolyzers and solid polymer electrolyte (SPE) electrolyzers. The alkaline electrolyzers feature an aqueous solution of potassium hydroxide used for its high conductivity and resulting in a faster dissociation of water. For the SPE, the electrolyte is a solid ion conducting membrane that allows the H^+ ion to transfer from the anode side of the membrane to the cathode side, where it forms hydrogen. Figure 4 shows a stylized depiction of the electrolysis process.

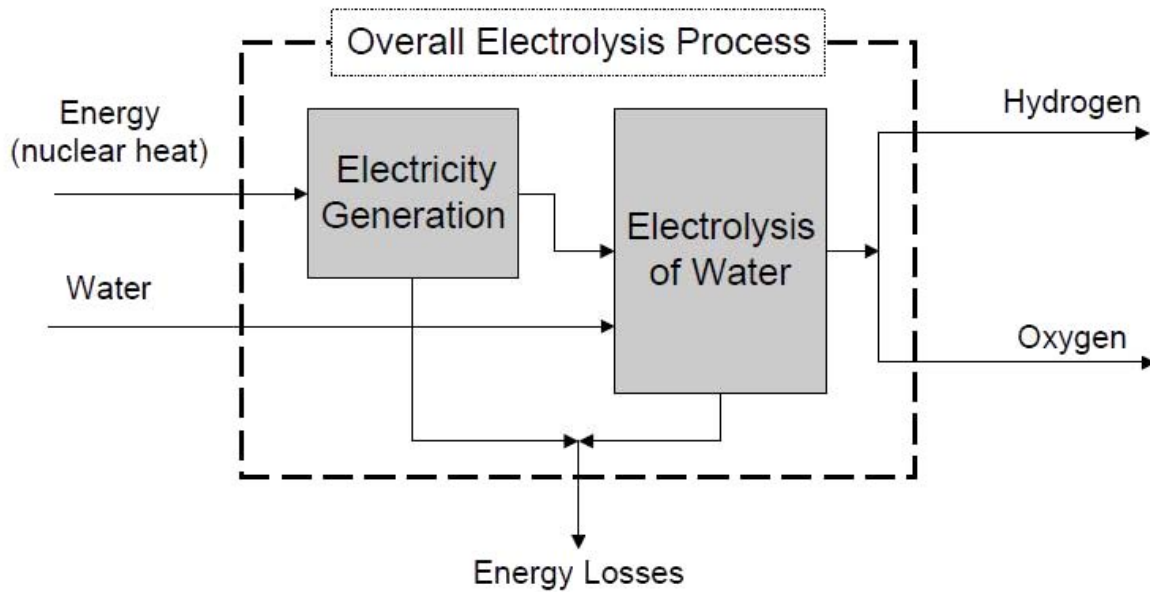
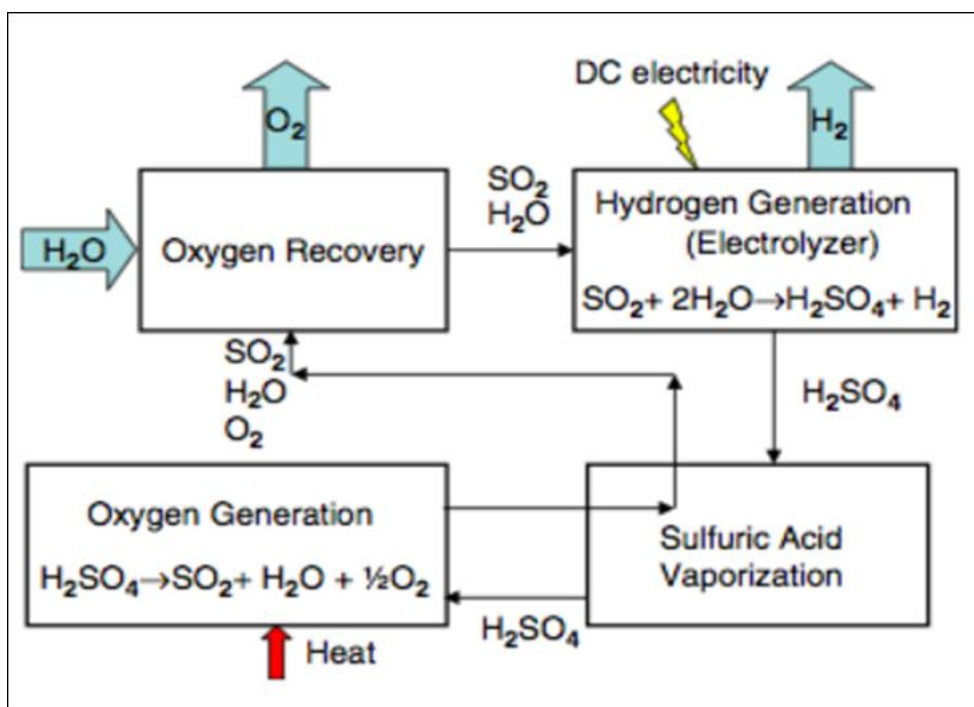


Figure 4: Electrolysis process block diagram

Both variations of water electrolysis feature low operating temperatures at atmospheric pressure as well as a reasonable amount of energy required to charge the anode and cathode. Alkaline electrolyzers require 100-150°C while SPE electrolyzers require 80-100°C. Both methods of water electrolysis are documented to require 1280-2133 MW electrical power requirement to obtain the desired hydrogen production rate of 682,560 kg/day. Though this electrical power requirement is not inconceivable, a hydrogen production process that requires a lower electrical power requirement would be preferred. The efficiency of the ES process alone is 75%, however, coupling this process to the 45% efficiency of nuclear energy results in an overall energy efficiency of 25-45%[6]. Furthermore, the hydrogen production rate of water ES is far lower than what is required by the biofuel process. The most powerful electrolyzer can produce just 1,048 kg/day of hydrogen, thus requiring 651 electrolyzers running in parallel to reach the production quota of 682,560 kg/day. Though this is not an impossible task, the prospect of scaling up water electrolysis to achieve the production rate is not desirable if another solution already capable of producing the necessary amount of hydrogen is available while using less electricity than this process.

3.2.3 Westinghouse Sulfur Process

The “hybrid” Westinghouse Sulfur Process (WSP) electrolyzer features four distinct steps of which one is thermochemical and one is electrochemical. Oxygen is generated from H_2SO_4 in a thermo-chemical reaction requiring 800°C. The resulting SO_2 , H_2O , and O_2 pass through the sulfuric acid vaporizer, and onto the oxygen recovery step where O_2 is removed. SO_2 and H_2O continue onto the electrochemical hydrogen generation, where a bias of -1.5 V produces H_2SO_4 and H_2 . The hydrogen is removed from the system, H_2SO_4 passes back through the sulfuric acid vaporizer, and the process begins again at the thermochemical oxygen generation step [4]. This is shown as a basic block diagram process in Figure 5.



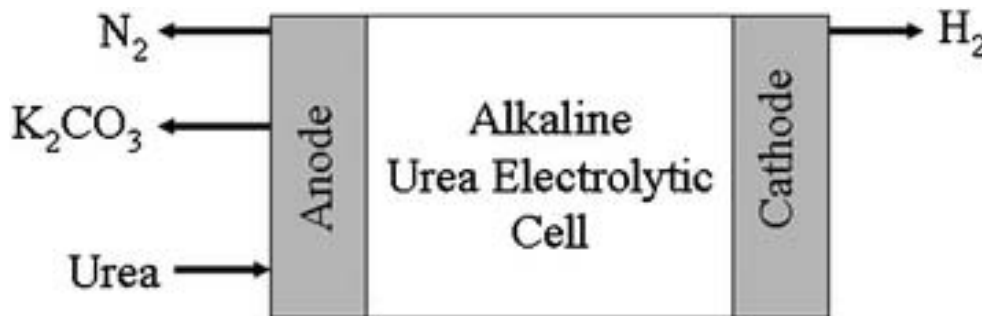
Courtesy of Edward J. Lahoda. Used with permission.

Figure 5: The Westinghouse Sulfur Process for hydrogen production [4].

Though the process looks elegant, it was one of the first designs dismissed primarily due to the sulfuric acid that would present and would introduce significant material corrosion concerns to the plant. In addition to the operating temperature of 800 C required by this process in a highly acidic environment, the coincidence of these two problems resulted in the rejection of the WSP as a method of hydrogen production.

3.2.4 Hydrogen from Urine

Urea from natural human waste contains hydrogen. Most importantly, these hydrogen atoms are only weakly bonded to the rest of the molecule and can be easily removed through the use of an inexpensive nickel catalyst [36]. The basic process is shown in Figure 6.



Bryan K. Boggs, Rebecca L. King, and Gerardine G. Botte. *Chem. Commun.*, 2009, 4859-4861. Reproduced by permission of The Royal Society of Chemistry.

Figure 6: Schematic representation of the direct urea-to-hydrogen process [36].

However, the amount of urine needed is prohibitive. It would take many gallons per hour to achieve the rate needed so transporting and storing the urine would become problematic. Furthermore, over time urea hydrolyzes into ammonia which is not as easy to use. Thus, the process would also have to work quickly. While the cost for the actual process, the storage and transport considerations for this hydrogen production process begin to become significant factors in overall costs at large volumes. Long-term storage lacks feasibility because of the hydrolyzation problem and so the idea was decided not to be advantageous.

3.2.5 Hydrogen from Bacteria

There are four main ways to produce hydrogen through biological processes: biophotolysis of water using algae and cyanobacteria, photo-decomposition of organic compounds by photosynthetic bacteria, fermentative hydrogen production from organic compounds, and hybrid systems using photosynthetic and fermentative bacteria [50].

Dark fermentation hydrogen production was determined to be the most commercial viable bacterial method. Dark fermentation is essentially the same process as algal biomass production in large open ponds followed by a dark fermentative stage. This method would yield close to 12 mol of H_2 for each molecule of glucose metabolized [69]. However, the high cost for the very large volume of raw material required coupled with the risk of system failure from biological contamination led to the rejection of this method [69, 85].

3.2.6 High Temperature Steam Electrolysis

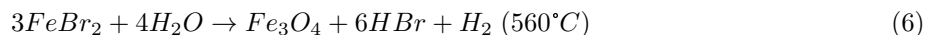
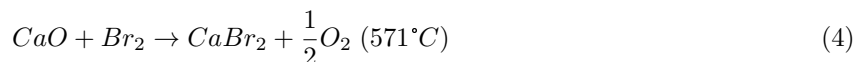
One of the more promising technologies is High Temperature Steam Electrolysis (HTSE). Similar to the electrolysis of liquid water, HTSE uses a cathode and an anode to split water molecules into hydrogen and oxygen. HTSE, though, has a huge advantage over liquid water electrolysis in efficiency. The lower enthalpy of formation of steam compared to water means that less electric power is needed to break apart the molecules. Unlike some other processes, the waste heat output by the core can be directly used to aid in heating the steam. The efficiency of the process grows with temperature becoming very efficient for high temperature reactors.

HTSE uses very simple chemistry and does not create any dangerous byproducts other than the hydrogen itself. The lack of CO_2 output at any stage of the process means that in addition to not polluting, it is also carbon neutral. There are materials concerns with steam at high temperature becoming highly corrosive, but these can be met with further research into ceramic materials.

While being very efficient and clean, HTSE has a problem when it comes to production volume. It has yet to be shown to be viable at the production rates required, and any increase in capacity would require scaling up existing models by orders of magnitude. For that reason, it was not as attractive an option at first, but was reconsidered later and work was done to prove its viability for this facility.

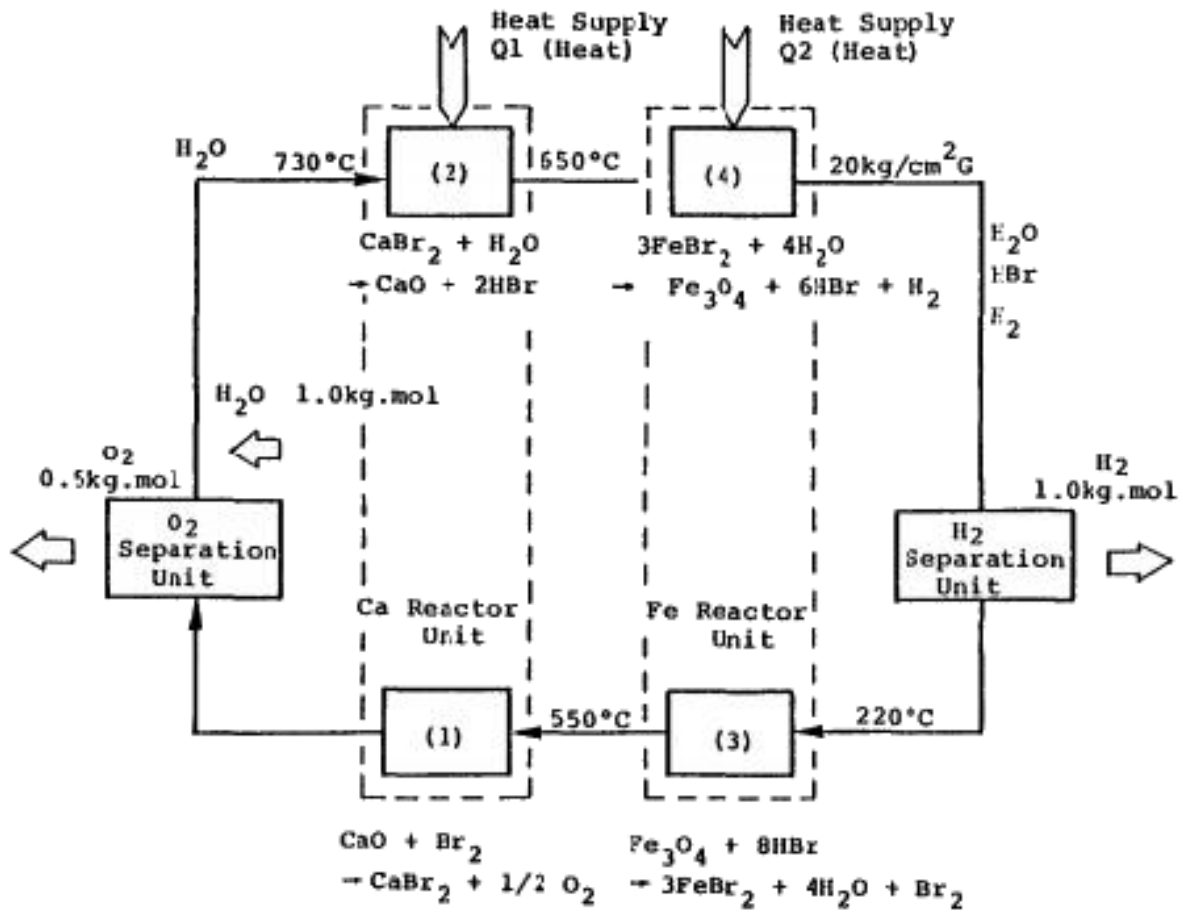
3.2.7 Br-Ca-Fe UT-3

The UT-3 process involves solid-gas reactions to produce hydrogen [156] using the reactions in Equations 3-6 at the temperatures indicated in parentheses [82].



High temperature steam cycles through two calcium and two iron reactors and is split into hydrogen and oxygen, as show in Figure 7.

The UT-3 process has been well demonstrated, and has been cited as both an economically and technically viable approach for commercial hydrogen production [31]. The UT-3 process can be scaled somewhat confidently for our hydrogen production needs, though more sophisticated simulations of this hydrogen production process would be required to confirm the analytical scalings to desired hydrogen production quotas are valid.



Courtesy of Elsevier, Inc., <http://www.sciencedirect.com>. Used with permission.

Figure 7: Schematic system arrangement of UT-3 process [31].

4 Biofuels

4.1 Main Goals of Biofuels

The biofuel plant's goal was to produce the greatest amount of fuel possible while utilizing the available resources of hydrogen from the hydrogen production plant and electricity and process heat from the nuclear power plant.

4.2 Design Parameters

Biofuels had two major decisions to make in designing a biofuels plant: what kind of renewable biomass feedstock to use and with what production process would the feedstock be converted. A literature search was made with these two overall questions in mind and the options were evaluated.

Concerning the choice of biomass, parameters of greatest importance were energy density, availability, costs, and competition with food sources. The energy density of a crop refers to how much energy can be derived from a given mass, and can be approximated by the lower heating value (LHV) of a crop in MJ/kg. For two crops treated with the same process, a greater LHV roughly translates to more or higher quality fuel production. Availability of a biomass is also important because there must be enough plant material available to produce biofuels on a commercial scale year-round. The design search allowed for the fact that some crops may not be widely grown at the current time, but had the potential to be grown on a large scale if their demand increased. Although not the most important factor, production and transportation costs also were examined to avoid expensive choices. Finally, crops were also evaluated based on their usefulness as a food crop because of the negative public perception associated with using food sources to create liquid fuels [96].

In choosing a production process, the technical feasibility, process efficiency, temperature of reaction, ability to utilize hydrogen resources, maintenance requirements, environmental impact, and final product of the biofuels plant were all examined. The need for hydrogen in a design was especially important because the hydrogen production facility, which would be coupled to the biofuels facility, was more economically feasible as a supplier to the biofuels plant than as a separate seller of hydrogen. The temperature required was also restricted by the process heat that would be available from the nuclear core, which would reach a maximum temperature of about 650°C. Feasibility and efficiency were maximized while maintenance and environmental impact were minimized as much as possible. The type of fuel which would be made also had to be chosen based on the quantity, demand, and associated revenue which could be generated [39].

4.3 Design Options and Evaluation

Five varieties of biomass and five synthetic fuel designs stood out in the literature search and the ones most suited for the coupled plant design were selected. As seen in Figure 8, there is more than one path to arrive at the desired products. Biomass sources considered were switchgrass, sorghum, energy cane, sugar cane, and corn. The synthetic fuel production processes researched were either biochemical (microbe electrolysis; algae transesterification; fermentation to ethanol) or thermochemical (syngas conversion to ethanol or Fischer-Tropsch fuels). A summary comparison of the various design options, which are explained in greater detail in the following sections, is shown in Table 4. After consideration of the design parameters, syngas conversion and the Fischer-Tropsch process were chosen to create biogasoline and biodiesel using switchgrass feedstock, steam, electricity, and hydrogen.

4.3.1 Possible Sources of Biomass

Biofuel production required a biomass source to first be selected. A comparison of fast-growing biomasses in Table 5, however, shows that many potential biomasses are also food sources. From the non-food sources, switchgrass was selected as the biomass because of its very high energy density, reliability, and the potential for scaling up to industrial levels of growth in North America [147], as illustrated in Figure 9. Switchgrass is rich in lignocellulose, which releases a large amount of energy when converted into syngas (a mixture of carbon monoxide and hydrogen) via gasification [90]. It is desirable to grow the switchgrass on site because transportation of biomass is extremely uneconomical. Although the current cost per ton is greater than

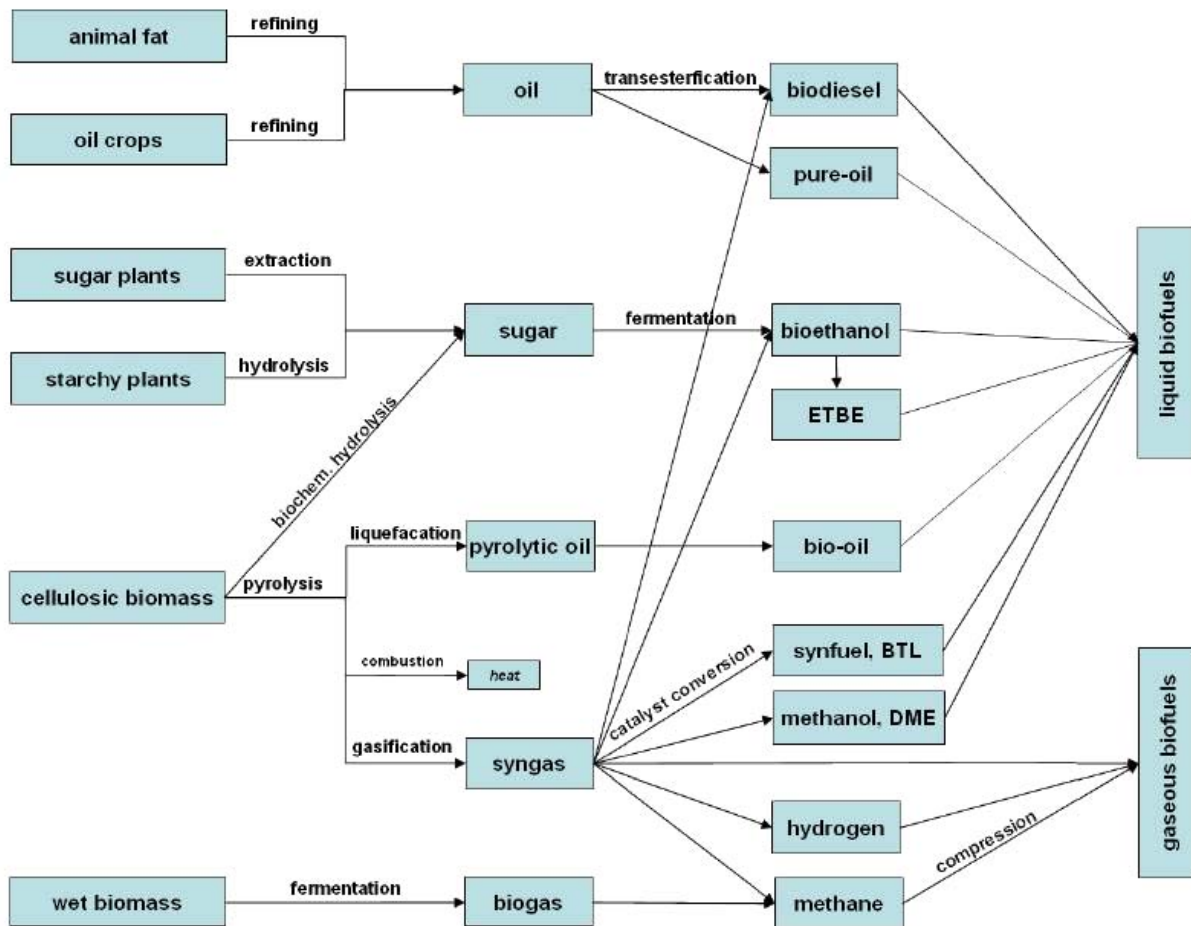
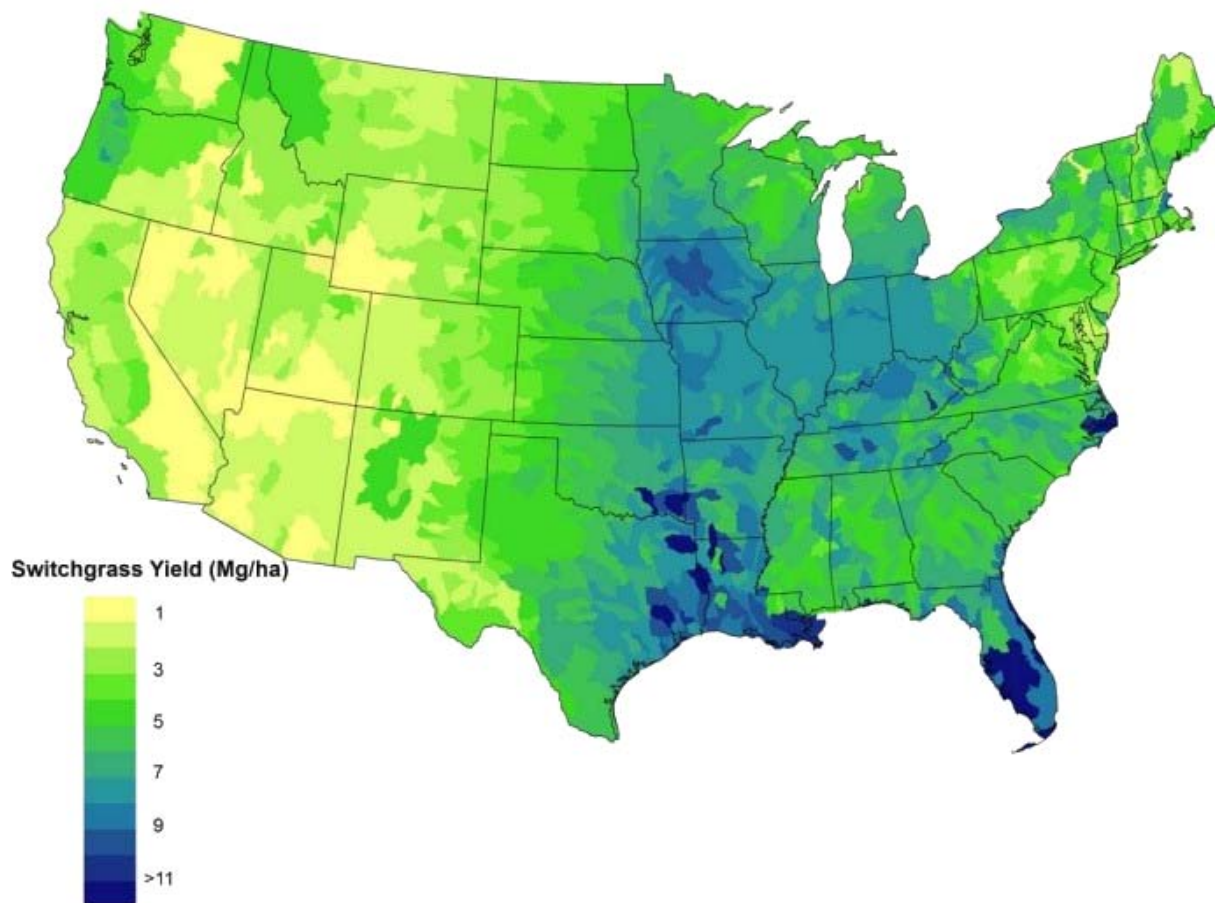


Figure 8: possible production paths for commercial products

Process	Reaction Temp. (°C)	H ₂ Input	Steam Input	Fuel Produced
Algae Transesterification	25-60	no	no	Oil, Diesel, or Ethanol
Microbe Electrolysis to Hydrogen	25-100	no	no	Hydrogen
Fermentation to Ethanol	190	yes	yes	Ethanol
Thermochemical to Ethanol	350	yes	yes	Ethanol
Thermochemical to FT Fuels	350	yes	yes	Gasoline and Diesel Blends

Table 4: Inputs and Outputs Comparison for Biofuel Production Processes

that for the other non-food source of energy cane, this value is derived from the amount of switchgrass currently available, not from the amount that would become available if switchgrass became a widely grown commercial crop [96]. Switchgrass also has high feasibility because it is easy to grow and has been used in many recent studies on large-scale biofuel production [68, 92].



Map courtesy of Pacific Northwest National Laboratory, operated by Battelle for the U.S. Department of Energy.

Figure 9: Simulated potential for switchgrass crop with one harvest per year[147]

Crop	Current Cost per Ton	Feasibility	Food Source?	Energy Density (MJ/kg)	Dry Tonnes per Acre/Year
Switchgrass	\$60	high	no	17	11.5
Sorghum	\$40	medium	yes	16.9	20
Energy Cane	\$34	medium	no	12.9	30
Sugar Cane	\$34	medium	yes	12.9	17
Corn	\$40-50	high	yes	13.4	3.4

Table 5: Comparison of Biomasses for Biofuel Production

4.3.2 Electrofuels to Hydrogen Process

Before the possibility of selling pure hydrogen was ruled out, an electrofuels process was briefly considered as an alternative way to produce hydrogen in tandem with the first hydrogen production plant. The electrofuels process is a biological means of producing hydrogen by applying voltage to a microbial electrolysis cell (MEC) containing carbon-fixing microbes. The MEC allows microbes to surpass the potential needed to produce oxygen and hydrogen gas and to serve as another means for the biosequestration of CO₂. Besides the

redundancy of building two hydrogen production plants operating on different systems in the same location, the electrofuels process was also ruled out because mass production of hydrogen fuel was found to be neither economically feasible nor safe at the present time.

4.3.3 Algae Transesterification Process

A second biochemical process considered was transesterification, where algae are used in chemical reactions to form new alcohols and esters. The benefits of the transesterification process are its high energy density and the low temperature requirement. Algae oil yield per acre is higher than other inputs and the processes involved require only temperatures of up to 60°C [45]. Algae can also capture carbon emissions from industry for reuse. Although transesterification has been highly developed in the United States, including a program from 1978 to 1996 to fund the development of renewable fuel from algae [134], it is still a difficult technology to utilize. Significant research is required to choose the optimal strain of algae with a maximized lipid content in addition to the fact that algae harvesting is difficult. Capital costs for the initial building are also high because the organisms must be protected from contamination. Thus, even the most optimistic predictions put algae production costs at over \$1.40/liter [45]. Additionally, algae transesterification only utilizes electricity, but not the hydrogen or high-temperature process heat resources that are available in this study.

4.3.4 Fermentation to Ethanol Process

Fermentation of biomass to ethanol is another biochemical route for making biofuels. In this process, biological feedstocks are first hydrolyzed (broken down) into basic sugars using a combination of acids and enzymes, then allowed to ferment into ethanol. Fermentation is orchestrated by incubating the sugars in a tank with carbon dioxide at slightly elevated temperatures and pressures. The resulting ethanol is concentrated and purified via distillation. As with algae transesterification, however, significant research is still required to engineer the appropriate yeast or bacteria which can efficiently convert the hemicellulose of biomass into ethanol. This process would require electricity and some process heat from the reactor, but again there is not space for a significant hydrogen input anywhere in the fermentation procedure [39].

4.3.5 Fischer Tropsch Process

Another process considered was the thermochemical Fischer-Tropsch (FT) process to either ethanol or biogasoline and biodiesel. In this process, biomass is combusted under low-oxygen conditions to create a producer gas. This synthetic producer gas, or syngas, is then used in the FT process to produce a distribution of products that include biodiesel and biojet fuels [90]. Finally, the array of products undergo a refining process to separate them into commercially ready alternative fuels. A representative FT process schematic is shown in Figure 10. While temperatures of up to 350°C are needed at various steps in the process, this is still comfortably lower than the temperatures required by the hydrogen plant and within the range that the nuclear core process heat will provide.

FT fuels are already being produced by companies such as Rentech and Choren [39], so they are feasible. The waste emissions of the process is low overall and consists of mostly charred ash from the gasifier, trace acid gases such as H₂S, and some CO₂ emissions [90]. However, as mentioned in the technical memorandum presented by Jechura to the National Bioenergy Center, the CO₂ waste comes primarily from the oxygen molecules of water, which are discarded as the hydrogen molecules are taken to refine F-T fuels [39].

Another advantage of this design is that FT reactions produce a variety of products that can be refined into gasoline, diesel, and jet fuel blends, which have much wider applications than pure ethanol. As the array in Figure 11 demonstrates, biodiesel fuel has the highest volumetric energy density of the possible products [25], costs less per gallon than fossil fuel diesel, helps reduce the US dependence on foreign fossil fuels, and reduces the United States' carbon footprint [30]. Furthermore, if implemented on a large scale, the estimated production costs for high energy density FT fuel could be as low as \$1/gallon [39], which makes it economically competitive.

For all of these reasons, the FT process has been selected as the optimal route for biofuels production. In conclusion, a nuclear power plant will be used to manufacture Fischer-Tropsch fuels in a gasification-based process using switchgrass, steam and electricity from the nuclear core, and on-site produced hydrogen. This

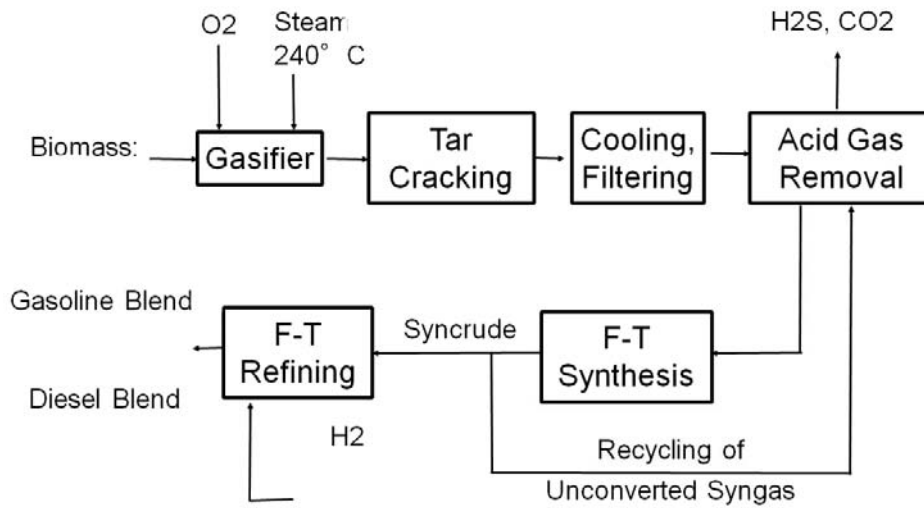


Figure 10: Basic outline of the process turning biomass into biodiesel fuel

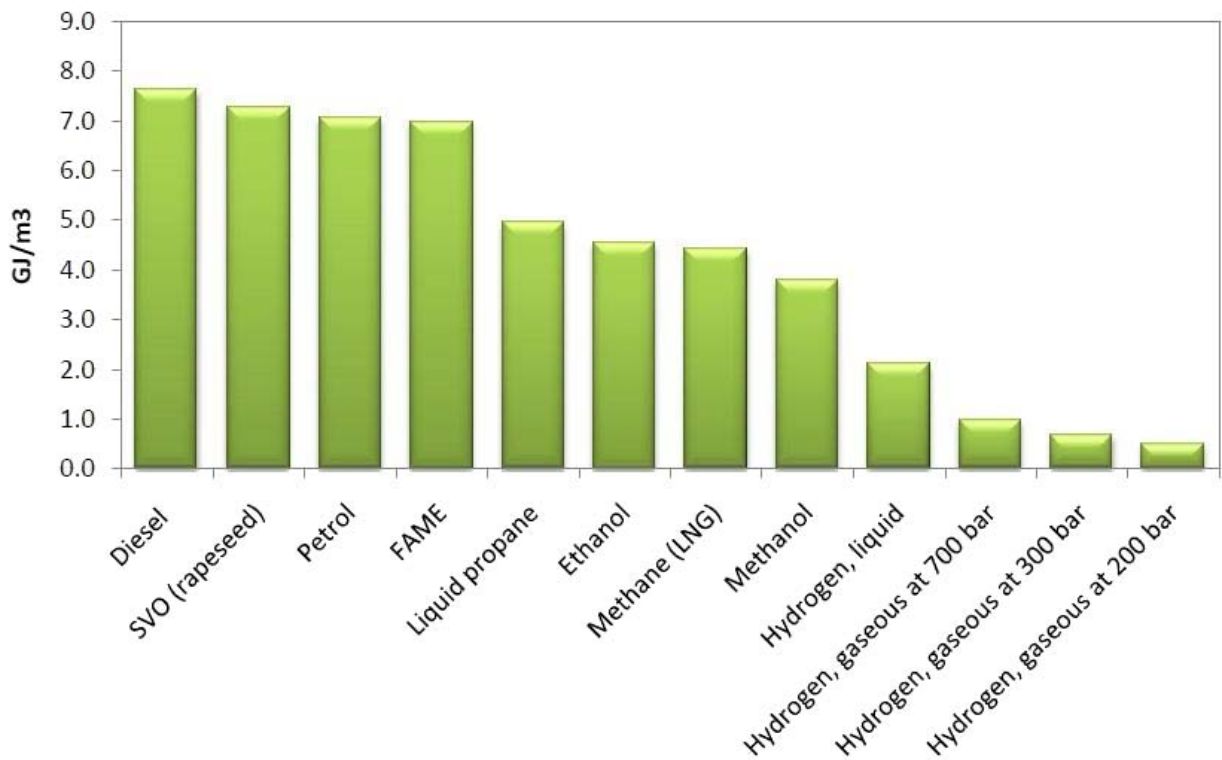


Figure 11: Volumetric energy density of alternative commercial fuels burned for energy[30]

nuclear-power-coupled plant, in contrast to most existing biofuels plants, will have a direct hydrogen source and thus eliminate both the heavy water consumption and the majority of CO₂ emissions, while the energy inputs from the power plant further minimize other costs associated the FT process.

Part III

Results

5 Overall Plant Design

The entire plant layout is shown on the following page. In order to make the design work more manageable, the layout was divided into four control volumes: (1) Core, (2) Process Heat, (3) Hydrogen, and (4) Biofuels.

6 Core

6.1 Process Overview

6.1.1 Core Overview

The final design calls for a 3575 MWt lead-bismuth eutectic (LBE) cooled fast reactor with a secondary supercritical CO₂ (S-CO₂) system. The core utilizes uranium mononitride (UN) as its fuel and a ferritic/martensitic steel (T91) [67] with a 100 micron corrosion resistant layer as its cladding material [138]. The core is composed of 12 rings of hexagonal shaped assemblies as shown in Figure 12. The inner ten rings house 253 fuel assemblies of 100 fuel pins each and 18 boron carbide (B₄C) control rods. The 11th ring is composed of a magnesium oxide (MgO) reflector and the 12th ring is composed of B₄C shield assemblies. The pool type design was chosen to permit as much natural circulation of the LBE as possible, supplemented by pumps for full power operation. The primary heat exchangers (HXs) are located at the top of the reactor vessel and use shell-and-tube technology. The outlet temperature for the coolant is 650°C and the inlet temperature is 484°C.

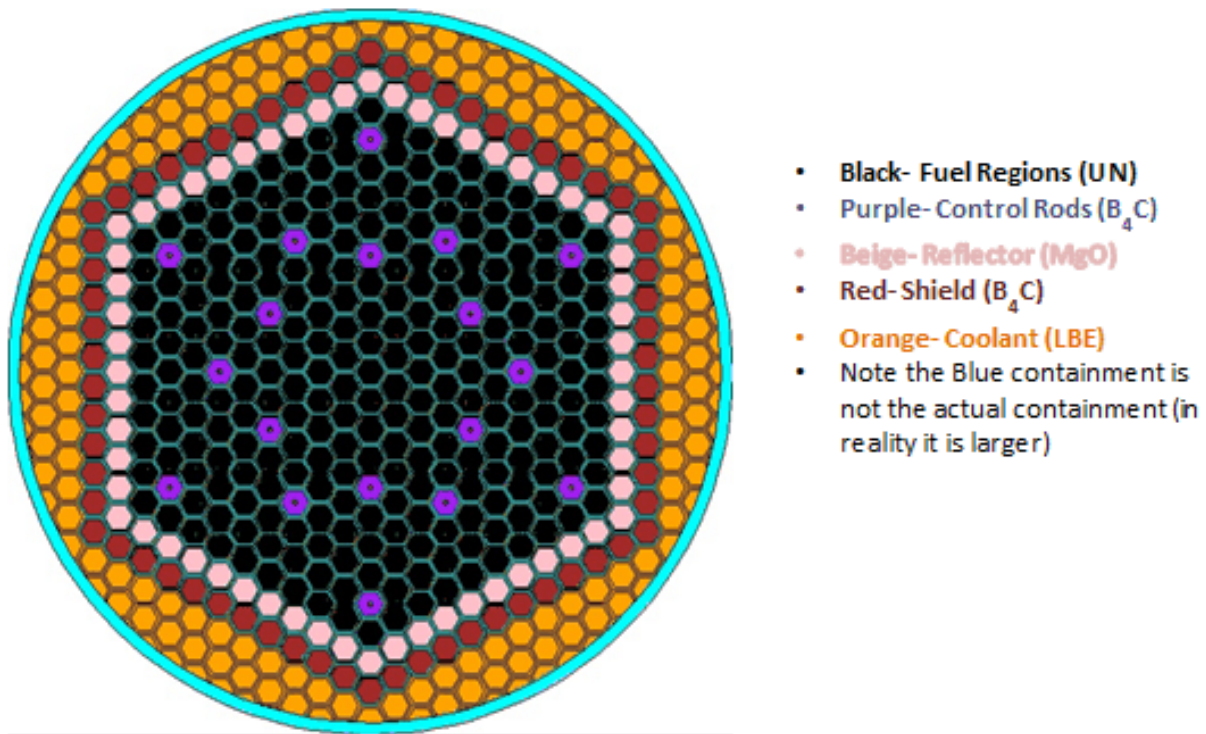


Figure 12: Radial view of the core showing the layout of the fuel assemblies, control rods, reflector, and shield.

6.1.2 Secondary Overview

The secondary loop consists of a S-CO₂ Brayton cycle, which extracts heat from the primary LBE loop by means of three heat exchangers. A small amount of this heat is transferred to the process heat group with a separate HX. The S-CO₂ drives a series of two 250 MW turbines per loop (of which there are three for a total of six turbines) with an intermediate compressor to ensure supercriticality is maintained. The S-CO₂ is then fed through a reheater and a condenser where it reaches its minimal temperature of 100°C. It is then recompressed, reheated, and pumped back to the primary heat exchanger to begin the cycle anew. The total cycle efficiency is calculated at 41.7% and produces at least 1 GW of electric power.

6.1.3 Table of Important Parameters

General		Primary	
Max Thermal Power	3575 MW	Primary Coolant	Lead-Bismuth Eutectic
Total Electric Power	1500 MW	Full Power Operating Mass flow Rate	143,600 kg/s
Grid Electric Power	1250 MW	Primary Coolant Velocity	2.5 m/s
Neutron Spectrum	Fast	Max Natural Convection Mass flow rate	90,000 kg/s
Outlet Temperature	650°C	Max Nat Convect Power	2240 MWt
Inlet Temperature	484°C	Heated Prim Coolant Area	5.66 m ²
Operating Pressure	Atmospheric	Secondary	
Fuel		Secondary Coolant	Supercritical CO ₂
Pitch	2 cm	No. of Secondary loops	3
Fuel Pellet Diameter	1 cm	No. of Turbines @ Full Power	6 (rated at 250 MW each)
Pin Diameter	1.25 cm	No. of Primary HE's	3
Pitch to Diameter Ratio	1.6	Gap + Cladding	
Fuel Material	UN	Gap material	Lead-Bismuth Eutectic
Active Fuel ht. @ BOL	1.9m	Gap thickness	1.14 mm
q' BOL	74.3 kW/m	Protective material	Stainless steel Fe- 12% Cr - 2% Si
Pin Height	4 m	Clad Material	T91 stainless steel
Peak Fuel Temperature	1862°C	Protective thickness	0.01 mm
Max Power Level transient before melt	75% Power Increase	Clad thickness	0.9 mm
Fuel Melting Temperature	2800°C	Fuel Assembly	
Max Fuel Enrichment	15%	Shape	Hexagon
Minimum Fuel Enrich	10%	Hexagon Pitch (flat to flat)	20 cm
Fuel Thermal Conduct	21 W/mK	Protective material	Stainless steel Fe- 12% Cr - 2% Si
Depletion/Kinematics		Fuel Assembly material	T91 stainless steel Fe-9%Cr-1%Mo-1%Nb
Burnup	TBD	Protective thickness	0.01 cm
Temp Coeff of React	TBD	Clad thickness	1.78 cm
Void Coeff of React	TBD	Gap between assemblies	0.4 cm
Core Refueling Frequency	TBD	No. of assemblies	253
		Pins per assembly	100

Figure 13: Table of important parameters for the reactor, still to be done are depletion calculations and kinematics

6.2 Primary System Design

6.2.1 Fuel

The fuel material chosen was uranium mononitride (UN). UN has some significant advantages over uranium dioxide (UO_2), the typical fuel for commercial nuclear reactors. It has a similarly high melting point as UO_2 , but has a substantial increase in thermal conductivity [143]. The increase in conductivity is necessary because of the higher temperatures the coolant is operating at and because of the high power density of the core (when compared to current commercial plants). Conservatively assuming a one meter active fuel height (current projections put the critical value near two meters), the maximum centerline fuel temperature for UN is $1,862^\circ\text{C}$ as compared to $6,600^\circ\text{C}$ for UO_2 .

When using UN as fuel, a drawback is the requirement that the isotope nitrogen-15 is used instead of the much more abundant nitrogen-14. The natural abundance of N-15 is 0.366%. The requirement to enrich the nitrogen adds significant fuel costs. However, there is less need to enrich the uranium when comparing to UO_2 , because N-15 is a better moderator and there is an increase in uranium in the fuel due to increased density and change in stoichiometry. Therefore, there is an advantageous offset in the cost and proliferation risk when using the UN due to the decrease in uranium enrichment.

6.2.2 Criticality Calculations

To calculate the criticality of our core, a model was constructed to run in Monte Carlo N-Particle (MCNP) code. The code for the final version (with the rods fully withdrawn) can be seen in Appendix A. The final results showing k-effective versus rod position can be seen in Figure 14.

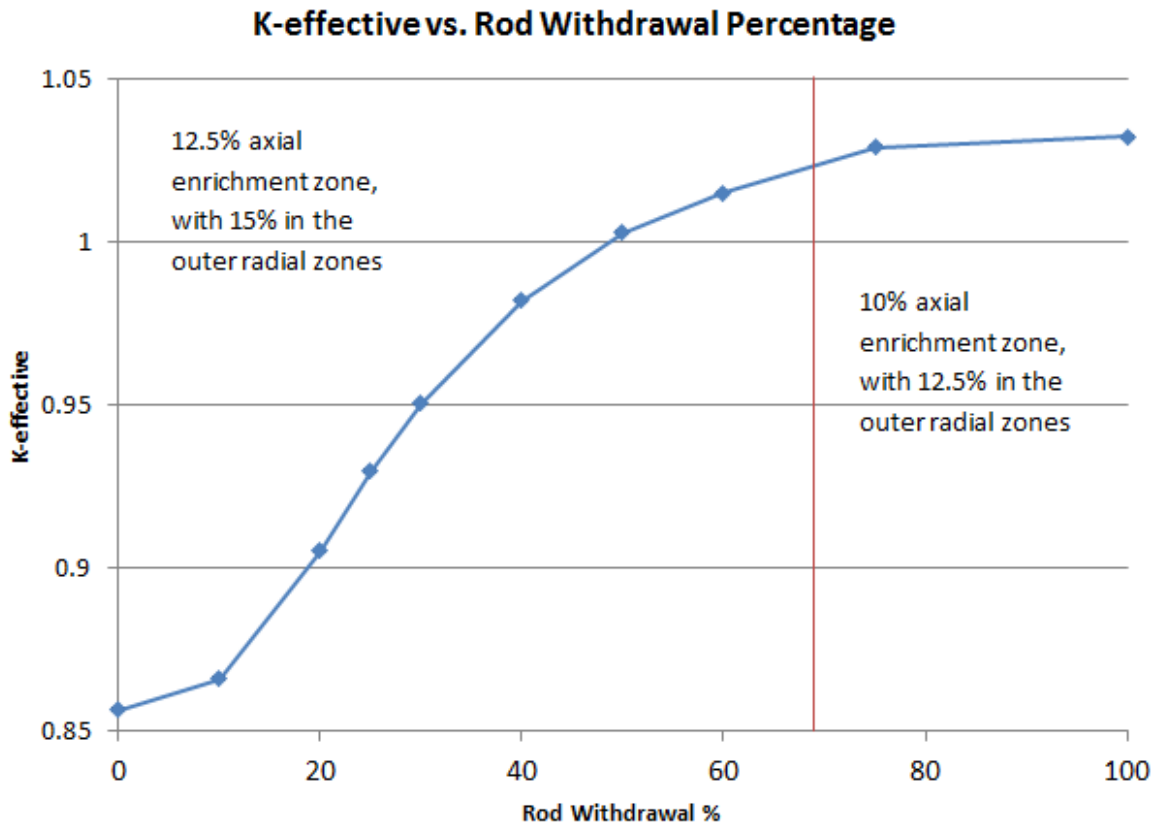


Figure 14: K-effective versus rod position for final core model

Some notable points on this figure are the two zones. In the lower 2/3 of the core the enrichment is

increased by 2.5%. The upper zone is slightly less enriched to lower the worth. Having a lower worth at the top of the core is useful because reactors do not want to operate with the rods fully withdrawn for safety reasons, hence the top part of the core is typically shadowed and the fuel is not being used. Another point is that the calculated critical rod position is slightly less than 50% withdrawal. As described in following sections, thermal analysis was done with a 1 m active fuel height which then added additional conservatism into the calculations.

6.2.3 Shutdown Margin

A requirement of all nuclear reactors in the United States is that with the most reactive control blade, or paired control blades, fully withdrawn with the reactor in a cold, xenon free situation, the core can be shutdown by at least 1% [154]. As can be seen in Figure 14, the reactor with the blades fully inserted is shutdown by nearly 15%. Therefore, with one, or even two, blades fully withdrawn the reactor can meet the shutdown requirement with plenty of margin remaining as all k-effective values were calculated for a cold, xenon-free condition.

6.2.4 Thermal Analysis

A key test of any reactor is to ensure that at full power the fuel is not molten. Furthermore, checks are usually done for light water reactors to ensure that there is sufficient margin to boiling and that the water in a fuel channel does not dry out. An advantage of using LBE is that the boiling point is 1,670°C which is over two and half times the operating temperature. Such a high boiling point removes the risk of boiling and dry-out in this reactor design. A thermal analysis was conducted with an axially varying linear heat rate that follows a sinusoidal shape. Values used for different thermal conductivities of the materials can be seen in Figure 15.

Material	T91/Protective Steel	UN	LBE
Thermal Conductivity	30 W/mK	21 W/mK	$\frac{86.334 + 0.0511 T}{2.45 T}$ (t is in kelvin)

Figure 15: Thermal Conductivities for different materials in a fuel pin

For all thermal analyses, a per pin mass flow rate of 5.676 kg/s was used. These results can be seen in Figure 16.

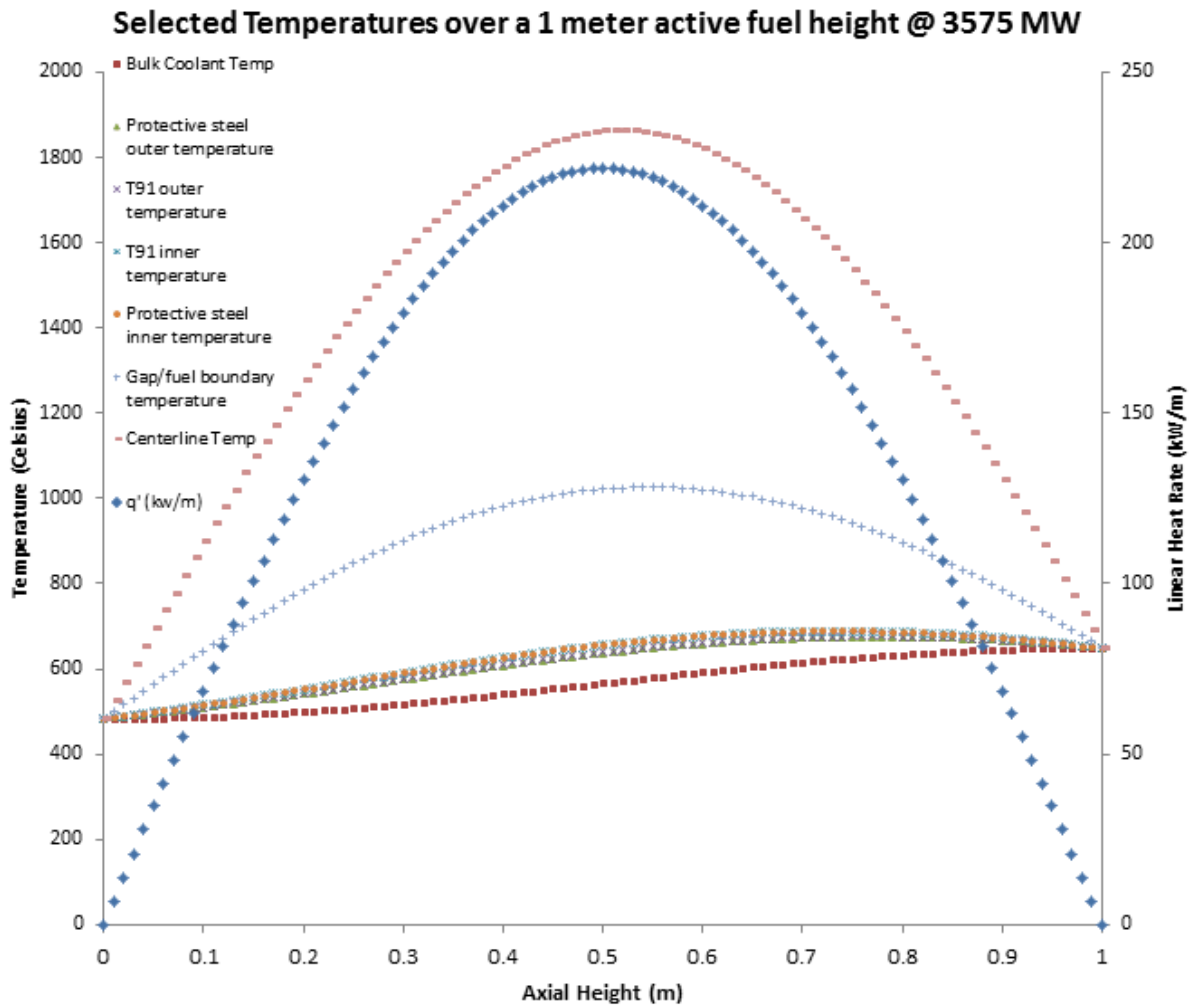


Figure 16: Temperatures at different locations in the fuel pin with varying axial height. This is shown with the axially varying linear heat rate (in blue).

As can be seen in Figure 16, the fuel operates nearly 1,000°C below the melting point of UN. Furthermore, the max cladding temperature remains below 700°C at all points. The LBE also remains substantially below its boiling point. Figure 16 also represents a conservative analysis because it was done with the active fuel height set to only 1 m. Had the active fuel height been raised (at beginning of life (BOL) this is 1.9 m) the operating temperatures become even more favorable.

6.2.5 Depletion Analysis

In order to estimate the lifetime performance of the core, it was initially thought that calculations would be made using the ERANOS fast reactor code, developed at CEA, France. This code is suitable because it can provide rapid computation of burnup, reactor kinetics, and other important values by solving the diffusion or transport equations for a 2D or 3D model of the core and has been well benchmarked against Monte Carlo codes, including MCNP. Unfortunately, the code was unable to be run properly in the time available for design. Instead, the literature was used to take a conservative estimate of the fuel inventory and burnup over the lifetime of the core. A 2400 MWt LFR had been designed in detail, including burnup analysis, by a group at MIT with a BOL fuel composition of ~71/14/15% U/TRU/Zr averaged over three zones[150]. This core was found to remain critical for 1,800 days, with $K_{eff} = 1.02$ at BOL and the control

rods fully withdrawn. Given that our LFR design has a K_{eff} closer to 1.04 at BOL with control rods fully withdrawn and a greater inventory of fertile material, it seems likely that this core could sustain criticality for at least 1,800 days, if not longer. The real limitations to core lifetime are due to cladding creep. The cladding temperature will exceed 600°C which will cause the onset of creep, limiting the lifetime of the fuel to around 460 days. This is less than a typical LWR refueling cycle and does not fully exploit the fuel. Future work will have to focus on reducing these temperatures or changing to higher temperature claddings, such as oxide dispersed alloys as they have limited creep though fail at the same maximum temperature. This will allow the core to make full use of the fuel and improve the economics of a once through cycle.

It was decided not to use a depleted or natural uranium blanket as a reflector around the core because this would likely lead to a concentrated build up of plutonium and proliferation concerns. Instead it was decided to use a magnesium oxide reflector and breed new fuel using the fertile material inside the fuel pins. Work at MIT has shown that this material significantly improves breeding which allows an increase of the lifetime of the fuel by up to 50%, though burnup of the cladding and other structural materials is still a limitation [97]. The reactor designed by the MIT group [150] analyzed the core inventory after 1,800 days and an average discharge burnup of 77 MWd/kf . They estimated that there would not be a significant increase in the Pu inventory (only 1.7% across the entire core) though there was up to a 3.1% increase in the outer zones. It will be important in the future to check what percentages of this Pu are Pu-239 and Pu-241 to ensure they do not exceed 90% of the total plutonium and present a significant proliferation risk. Taken together, these studies suggest there will not be a dangerous build up of Pu in our reactor core design though this remains to be verified using ERANOS.

One promising result was the burning of minor actinides in the fuel at BOL. The amount of minor actinides decreased by 24.1% from 1255 MH kg to 953 MH kg after 1,800 days. This suggests the possibility of using minor actinides as fuel in future iterations of our reactor design which would give the reactor an economic boost as well as allowing it to become part of the United States' nuclear waste solution.

6.2.6 Core Reactivity Feedback Parameters

When calculating core kinetics and safety factors, estimations again had to be made from the literature due to an inability to calculate these directly using the ERANOS code. Again, the LFR analyzed by the MIT group was used due to its similar size to our design[150]. The Doppler coefficient of an LFR is expected to be negative due to the hard spectrum and was found to be -0.111 ± 0.030 c/K . The coolant temperature coefficient was found to be positive but again quite small, 0.131 ± 0.052 c/K . Lead exhibits a small insertion of positive reactivity with decreased density accounting largely for this positive coefficient[150]. The scattering cross section of lead also increases with higher temperatures, thus increasing moderation and leakage. However, when similar calculations were made over an SFR core, the use of an MgO reflector reduced this temperature coefficient due to the reduction in fuel enrichments that were possible[97]. These calculations will have to be verified for this design using a code like ERANOS.

6.2.7 Natural Circulation and Flow Analysis

One of the benefits of an LBE cooled reactor operating at relatively high temperatures is that it is possible for the coolant in the core to be entirely driven by natural circulation. It was unclear whether this would be possible with this design due to the large increase in the core size, but first order calculations were made to estimate the contribution of natural circulation in order to reduce the load on the circulation pumps. Initially, it was only important that to check the feasibility of using natural convection to drive the coolant and it was assumed that there would be no significant temperature loss between the heat exchanger and the core and that the reactor pressure vessel (RPV) was an adiabatic chamber. Figure 17 shows how this simple model would then look. Note that there is a third LBE/CO₂ heat exchanger going into the page.

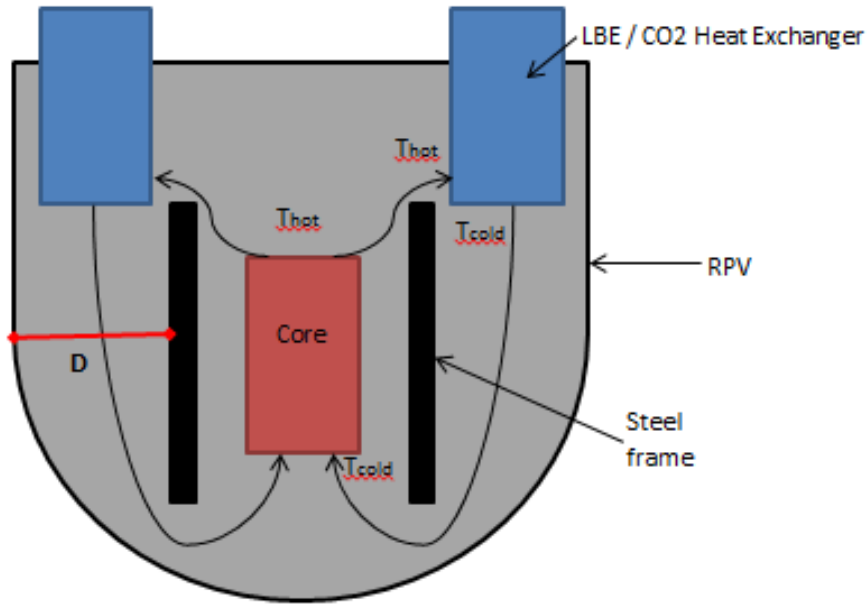


Figure 17: Sketch of model for LBE flow calculations

The core channel and the down channels between the steel frame walls were modeled as pipes with diameters equal to their width. The width between the core channel and the edge of the RPV is labeled on the left as D in Figure 17 and is one of the variables that may be changed in order to further aid natural convection. Given that the pitch to diameter ratio is quite large at 1.6, the rod bundles were approximated as annular flow for the purposes of calculating the friction factor [141, 86]. The pressures in the core channel and one of the down channels were then balanced and a function for the mass flux found using Equation 7.

$$G \approx \frac{2D^2(\rho_{hot} - \rho_{cold})}{23.95\eta} \quad (7)$$

Figure 18 shows a plot of the mass flux through the core for a given temperature rise across the core, an outlet temperature of 650°C , and a given width D . The horizontal line shows the mass flux of $25,371 \text{ kg/s-m}^2$ required to cool the core at full power.

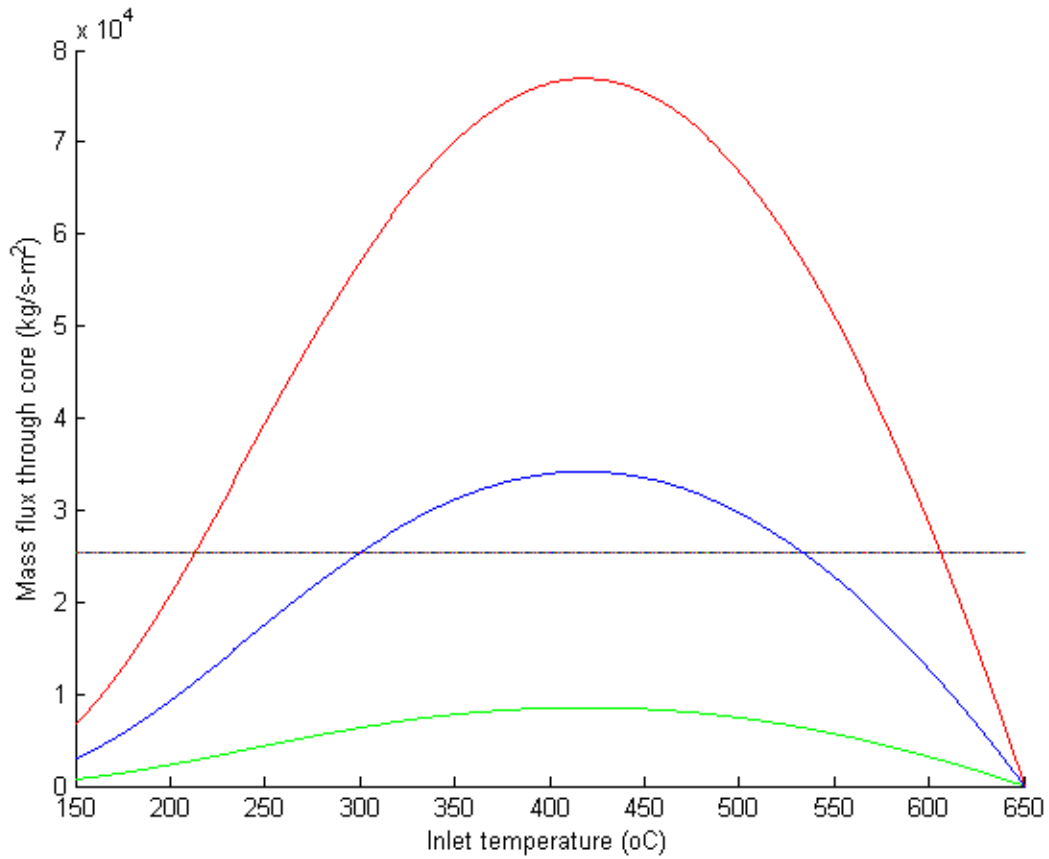


Figure 18: Mass flux through down channel given an outlet temperature of 650°C for varying inlet temperatures and values of D . Green represents $D = 1$ m, blue represents $D = 2$ m, and red represents $D = 3$ m.

The reactor will operate with an inlet temperature of 480°C and with a temperature rise of about 170°C so from Figure 18, it is proven that natural circulation can drive a significant amount, if not all, of the coolant flow in the core. Depending on the chosen width, D , the remaining flow will be provided by pumps. Figure 19 shows how the Reynolds number changes for the flow in the down channel with varying inlet temperatures and widths. In the cases where $D < 2$ m, the flow remains laminar, but above that, it transitions to turbulent flow.

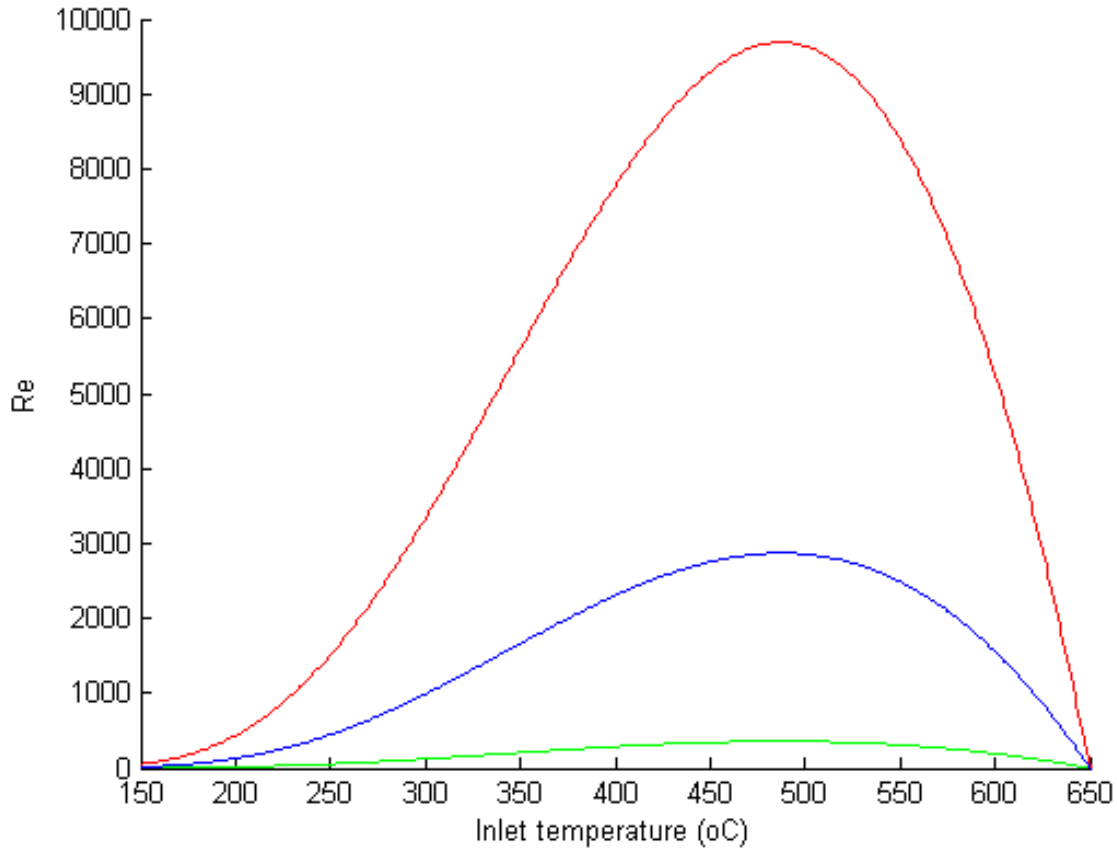


Figure 19: Variation in Reynolds number for flow through down channel given an outlet temperature of 650°C for varying inlet temperatures and values of D. Green represents D = 1 m, blue represents D = 2 m, and red represents D = 3 m.

This will increase the pressure loss in the system and reduce natural convection. In the case where for D = 3 m, the mass flux is closer to 35,000 kg/s-m². This is still sufficient to meet the needs of the core, but is less than half of what a laminar regime could provide.

As discussed previously, in order to avoid corrosion of the walls the velocity of the LBE must remain at or below 2.5 m/s, so this is the LBE velocity being used to cool the core. As such, D must be optimized to only just meet the required mass flux. Given the simplicity of this model, it was assumed that some losses are neglected so in order to compensate for this, a mass flux of 28,500 kg/s-m² was targeted. This is achieved by setting D = 1.9 m (when approximating to the nearest decimeter). Figure 20 shows the mass flux plot for this setup with changing inlet and outlet temperatures. Analysis will have to be conducted in order to decide whether it is worth allowing the reactor to remain at higher temperatures during shutdown in order to maintain this natural circulation or if pumps can drive the entire flow.

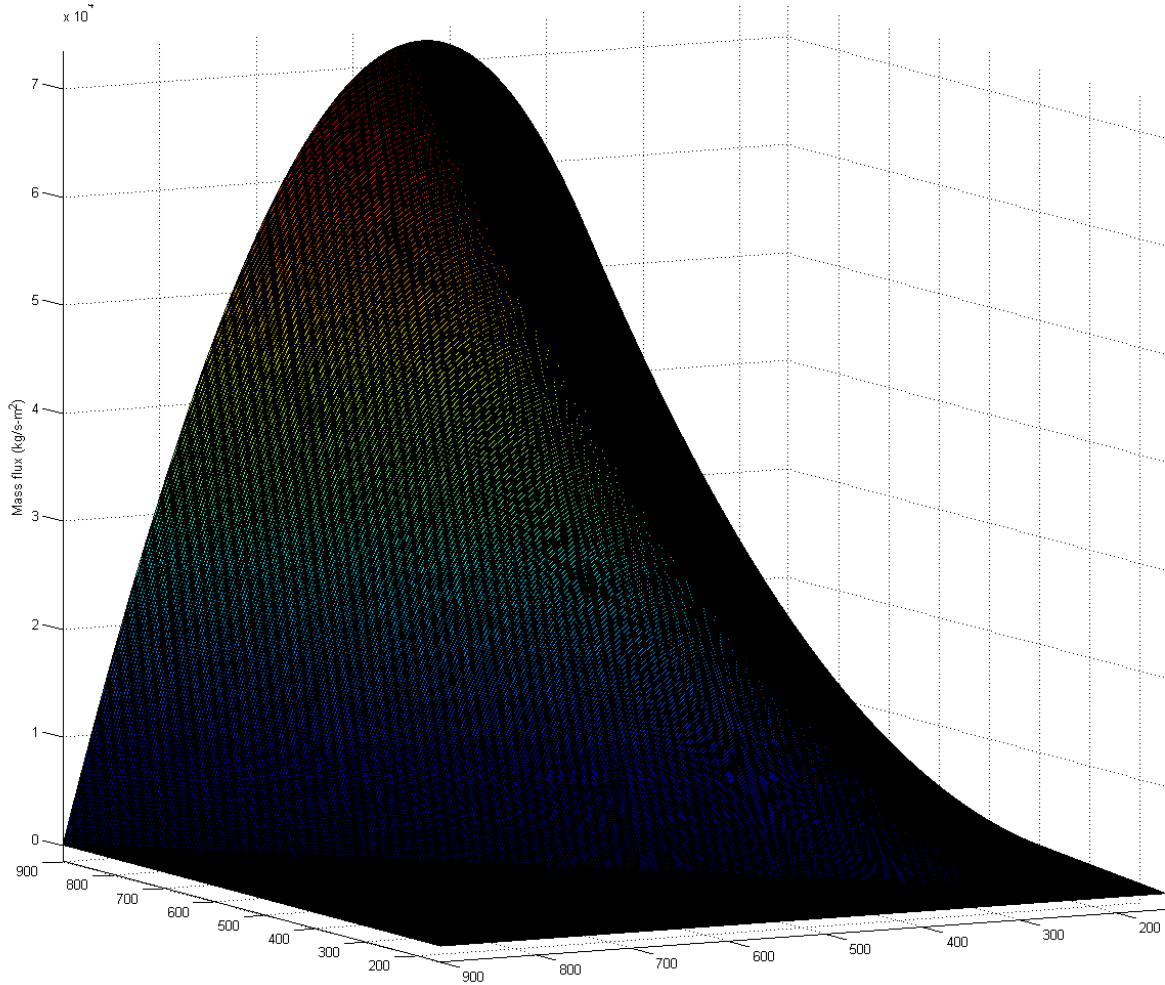


Figure 20: The axis going up the screen is mass flux (kg/s-m^2), the axis on the lower left side of the screen is inlet temperature ($^{\circ}\text{C}$), and the axis on the lower right side is outlet temperature ($^{\circ}\text{C}$).

This plot can also be used to predict the behavior of the coolant during accident situations. Fortunately, due to the high boiling point of LBE, it is unlikely that voids will form and the density of LBE drop significantly. However, at significantly high temperatures, the flow may transition to a turbulent regime thus reducing the mass flux. In general, the natural circulation should suffice as long as a temperature rise across the core of about 150°C is maintained. Undercooling is therefore a large concern and a secondary heat dump in the RPV is going to be necessary. This could also allow an operator to sustain natural circulation at lower core powers during shutdown by providing heat to the core from the PCM storage and then moving it to this secondary heat dump. A final point of consideration during accident analysis will be deciding how long a high flow of LBE caused by high temperatures in an accident could be sustained without damaging the pipes due to erosion.

6.2.8 Safety Systems

Another advantage of using a LBE-cooled fast reactor is its many inherent passive safety features. The difference in inlet and outlet temperatures of the reactor allows for a significant natural convection mass flow rate of $90,000 \text{ kg/s}$. Natural circulation should be able to provide sufficient shutdown flow provided the decay heat remains high; for long shutdowns heating will be provided by process heat storage to keep the LBE above its melting temperature. This will also help maintain the ΔT across the core needed for natural circulation. LBE also provides a significant heat sink with large margin to boiling, essentially

eliminating the issue of coolant boiling. Reactor Vessel Auxiliary Cooling Systems (RVACs) will be able to provide additional heat removal, in case of loss of a heat sink in addition to a large inventory of primary coolant. Because of the large margin to melting, pressurization of the core is not needed and it can run at atmospheric pressure. Scenarios were analyzed to see what would happen in the case of a transient power raise. Up to a 75% increase in power could be taken before the fuel reached its melting point. As temperature is raised, the thermal conductivity of the LBE also goes up, which aids in heat removal. Another analysis was used to determine at full power if the bulk coolant temperature would cause fuel melting. Temperatures of up to 1,400°C could be withstood by the fuel before melting. However, at such temperatures the LBE gap would boil and the cladding would fail. Nevertheless, this analysis shows the resiliency of the fuel material. It is recommended that to maintain the strength of the T91 clad, the temperature should ideally remain below 700°C. At normal operating temperatures, the clad always remains below 700°C and will still remain below that value even with a 10% increase in power. Beyond this point, the creep effects on the T91 begin to accelerate the clad and it loses much of its lifetime. As it is, T91 can only be operated at 650°C for a limited amount of time (less than two years) and in order to enhance safety and provide better longevity, a new clad will need to be chosen.

6.3 Secondary System

A basic overview of the core's secondary system can be seen in Figure 21 with node values shown in Figure 22.

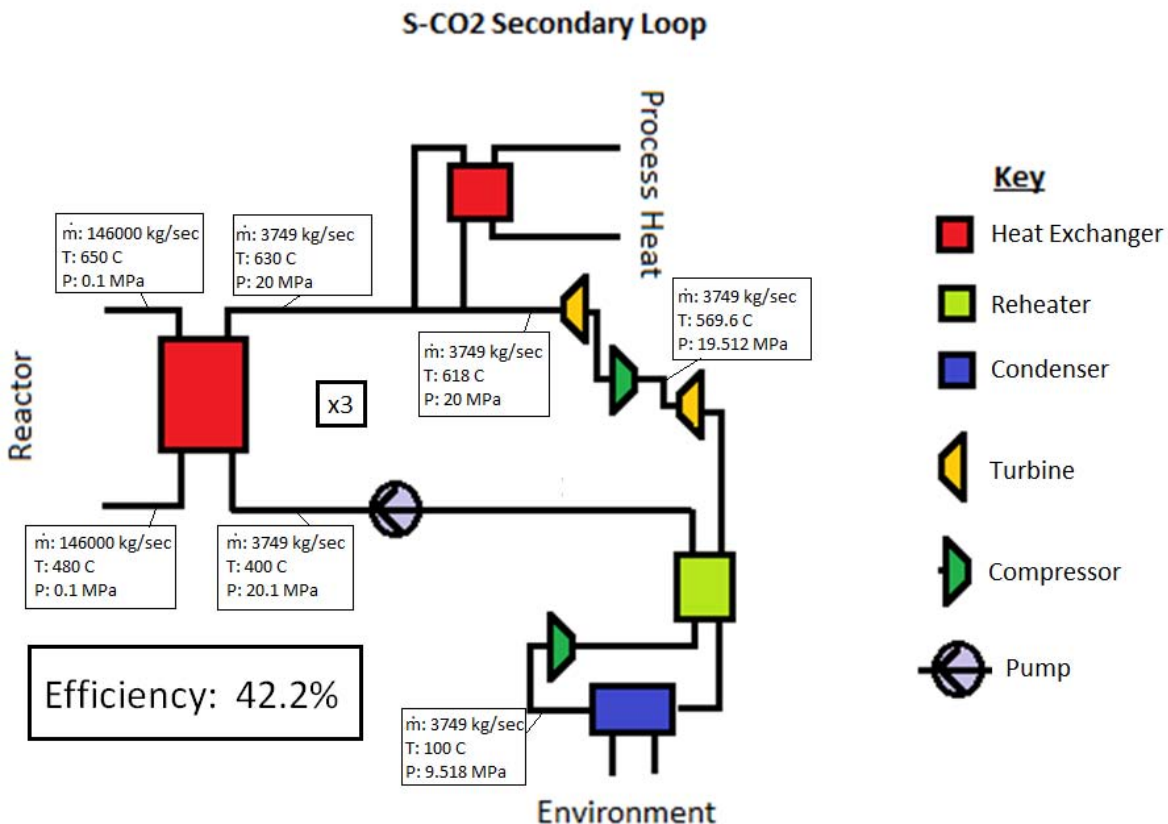


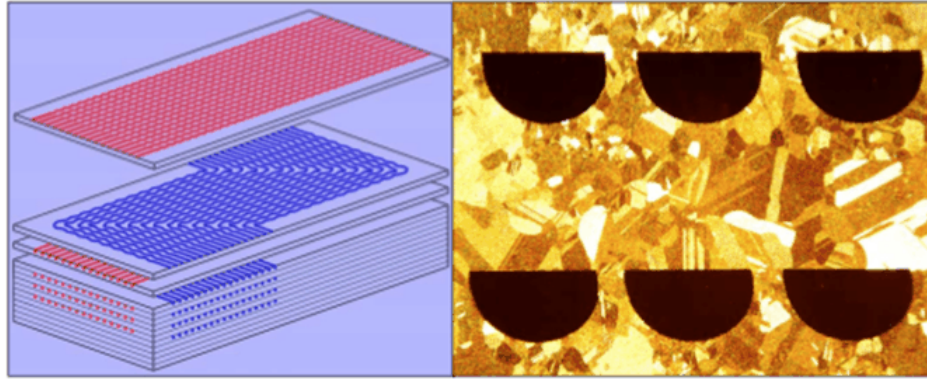
Figure 21: Overview of the secondary system of the reactor

Node Number	Temperature (Celsius)	Pressure (MPa)	Mass Flow (kg/sec)
1 (LBE)	650	0.1	146000 (all flow)
2 (LBE)	480	0.1	146000 (all flow)
3	630	20	3749
4	630	20	3449
5	630	20	300
6	478.5	20	300
7	618	20	3749
8	554.1	9.756	3749
9	570.7	21.463	3749
10	504.9	10.470	3749
11	219.2	10.470	3749
12	100	10.470	3749
13	150.8	23.034	3749
14	400	23.034	3749
15	400	23.100	3749
16 (Water)	20	0.1	13715
17 (Water)	30	0.1	13715

Figure 22: The nodal values of temperature, pressure, and mass flow for the secondary system

6.3.1 Heat Exchanger

In selecting the heat exchangers (HXs) for the reactor, several geometries were considered and compared using data from the STAR-LM reactor conceived by Argonne National Laboratory. The design of the STAR-LM reactor design also consists of a LFR with a S-CO₂ secondary cycle. As a result, the relative trends associated with the STAR-LM secondary system were assumed to be analogous to the trends that would be observed in the production of this LFR design. The initial objective was to use a Printed Circuit Heat Exchanger (PCHE) design as the in-reactor heat exchanger. The PCHEs are produced by the British company, HEATRIC, which is a division of Meggitt (UK) Ltd.[38]. These heat exchangers consist of flat plates with semi-circular flow channels that are stacked and adhered together through diffusion bonding. A schematic of this type of heat exchanger is shown below in Figure 23.



© Heatric. All rights reserved. This content is excluded from our Creative Commons license. For more information, see <http://ocw.mit.edu/fairuse>.

Figure 23: Printed Circuit Heat Exchanger (PCHE) Design

The PCHE design allows for efficient heat transfer between working fluids (results in 44.1% cycle efficiency if used as the in-reactor heat exchanger). Additionally, PCHEs are extremely compact with a height of 2.76 m, which is a fraction of the heights of other HX types. This decrease in size could lead to cheaper and more deliberately compact system designs that would use a fraction of the materials in comparison to other design options.

The largest obstacle with using the PCHE design for the in-reactor heat exchanger results from the reactor coolant. While a PCHE could be made to facilitate the heat exchange from the LBE to the S-CO₂, the flow channels for the LBE would need to have a significantly larger diameter than the diameter of the flow channels for the S-CO₂ due to the greater viscosity and frictional factor for the LBE. Consequently, a simpler design for the in-reactor heat exchanger was chosen.

From the possible HX designs, a basic shell-and-tube heat exchanger was chosen because of its simplicity and ease of manufacturing compared some of the other designs, including the straight annuli tube HX. In order to maximize the heat transfer and flow of LBE through the shell-and-tube heat exchanger, two geometries of the tubes within the heat exchanger were considered: a rectangular, in-line geometry and a triangular, staggered geometry (both shown below in Figure 24).

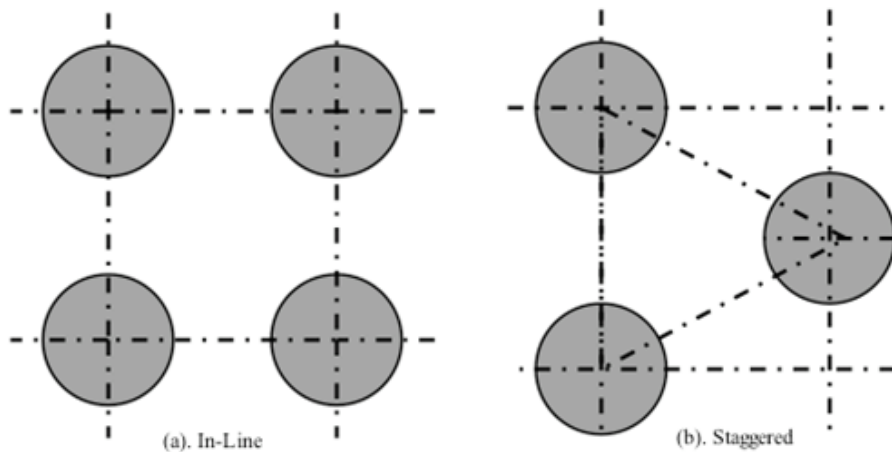


Figure 24: Geometry options for the in-reactor shell-and-tube heat exchanger.

Due to the viscosity of the LBE, the staggered geometry of the tubes allowed for a greater amount of flow through the sub-channels and thus resulted in better heat transfer between the LBE and the S-CO₂ so

this design was ultimately chosen [140].

For the recuperator (a regenerative HX) in the secondary cycle that preheats the S-CO₂ before it returns to the in-reactor heat exchanger, the PCHE heat exchanger design was chosen. This design is more advantageous than a shell-and-tube HX at this point in the system because the heat exchange between S-CO₂ to S-CO₂ does not have the same viscosity and friction concerns that exist between the LBE and S-CO₂. The aforementioned benefits of the compact PCHE design made it the best choice for the recuperator component of the secondary system.

6.3.2 Condensers and Compressors

The compressors used increase the pressure by a factor of 2.2 and use about 42 MW of power to operate. Compressors are placed both in between the turbines (to ensure the pressure keeps the S-CO₂ supercritical) as well as after the condenser to help bring the pressure back to its maximum value in order to complete the cycle. The condenser uses an environmental water source (i.e. river, ocean) to decrease the temperature of the S-CO₂ before it is recompressed and reheated to be fed into the primary heat exchanger. Using a minimum temperature of 100°C guarantees that the supercritical temperature (~31°C) is met with sufficient margin. The mass flow of water required to cool to this temperature was determined to be 13,715 kg/s, well within reason for existing condensers already in use.

6.3.3 Accident Scenario Analysis

The main two accident scenarios that are essential to explore in this design are a loss-of-heat-sink (LOHS) event without a scram in the core and a loss-of-generator-load (LOL) event without a scram.

LOHS event without a scram

Following this event, the temperatures throughout the system will begin to rise because the reactor is still producing heat without it being properly removed. As a result, the coolant density will begin to decrease, which coupled with the Doppler effect in the fuel, will induce a decrease in reactivity in the core. As time progresses following this event, heat will continue to be generated, but the rate at which this heat generation will occur will begin to decrease with time. Since the heat will not be properly removed by the secondary cycle, the Reactor Vessel Auxiliary Cooling System (RVACS) will be responsible for the majority of the heat removal. During this time, the system temperatures will continue to increase due to the decay heat produced by the core, which will result in a greater amount of negative reactivity being inserted in the reactor. Over time, the rate of heat removal by the RVACS will exceed the heat generation rate from decay heat, and the temperature of the system will begin to decrease, causing an increase in positive reactivity. Consequently, the system will experience oscillations in the power level as well as in the temperature over time, but the actual power level will remain low compared to the level at full power [107].

LOL event without a scram

A LOL accident is considered to be one of the most severe accidents that may occur in the secondary S-CO₂ Brayton cycle, although the system's response does not pose significant safety concerns overall. In this accident scenario, the assumption is that the generator is separated from the grid. Initially, it is estimated that since the turbine energy that would normally be sent to the grid cannot be transferred, the response of the secondary cycle will be to try to minimize the amount of departure from the normal function. However, the rotational speeds of the turbine will increase drastically. Immediately following the LOL event, the S-CO₂ Brayton cycle control system will open the turbine bypass valve, which must occur at an extremely rapid rate (from fully closed to fully open in less than 0.5 seconds). Once this valve opens, the flow rate of the S-CO₂ will decrease. Following this event, the temperature of the LBE coolant in the reactor will increase, introducing a negative reactivity insertion into the core, which reduces the power level in the core [107].

6.4 Economics

Another important aspect of assessing the feasibility of this LFR design with a secondary Brayton cycle loop is determining whether the reactor could be economically competitive with other power plants. In particular, it is of interest to examine the cost comparison between this system and a typical light-water reactor (LWR). In a paper written by V. Dostal, M. J. Driscoll, and P. Hejzlar, it is shown that estimating the cost of components in the secondary cycle of this reactor is particularly difficult because there are limited examples of these components actually in use, and therefore, the cost estimate is primarily founded on expert opinions [54]. Dostal, et al. [54] utilized the data associated with the helium Brayton cycle in order to provide an approximate cost comparison, which will also be done in this economic analysis. Ultimately, Dostal et al. assert that, “The supercritical CO₂ cycle is more efficient than the steam cycle and its operating and maintenance costs are not expected to exceed those of the steam cycle. Therefore, if the capital cost of the supercritical CO₂ cycle is lower than that of the steam cycle the electricity generation cost will be lower as well” [54]. In a comparison between the cost of the turbo-machinery for a helium Brayton cycle and the cost of the turbo-machinery in a S-CO₂, it was found that the cost of the S-CO₂ cycle would be less than that of the helium cycle. An overview of the cost comparison between the two can be found in Table 6.

Turbomachinery	Conservative	Best Estimate	Cons.	Best Est.	Cons.	Best Est.
Temperature (°C)	550	650	700	550	650	700
Efficiency (%)	41.0	45.3	47.0	43.1	47.1	48.9
Power (MWe)	738	815	846	776	848	880
Temperature Ratio	0.925	0.932	0.940	0.925	0.932	0.940
Power Ratio	0.01	0.960	0.983	0.931	0.985	1.008
Pressure Ratio	0.730	0.730	0.730	0.730	0.730	0.730
He Turbine (K\$)	78,000	78,000	78,000	78,000	78,000	78,000
CO₂ Turbine (K\$)	47,455	50,945	52,614	49,035	52,272	53,952

Table 6: Summary of turbine costs [54]

The reheater in the secondary loop’s (a HEATRIC PCHE) cost can be estimated using the weight of the heat exchanger. It is estimated that for stainless steel PCHE units, the cost is \$30/kg, while the cost for titanium units is \$120/kg [54]. In order to determine the fraction of metal in the PCHE, Equation 8 can be used where f_m is the fraction of metal per cubic meter, d is the diameter of the semicircular channel, P is the channel pitch, and t is the thickness of the heat exchanger plate [54].

$$f_m = 1 - \frac{\pi d^2}{8Pt} \quad (8)$$

In order to obtain the volume of metal used in the PCHE per cubic meter of its volume, Equation 8 must be used with the parameters of the unit to obtain the fraction of metal per cubic meter. This result can then be multiplied by the total volume of the unit to find the total mass of metal. The total cost of the unit can then be calculated using the appropriate \$/kg number.

To summarize the estimations between a steam cycle (coupled with a high-temperature gas reactor HTGR), a helium cycle, and a CO₂ cycle, a comparison was made between the total capital cost of the cycle as well as the capital cost per kWe associated with the cycle. This comparison can be found in Table 7.

This summary of fractional costs of various S-CO₂ cycles demonstrates that this design may be economically competitive with other secondary cycles. As a result of the compact size and efficiency of the S-CO₂ Brayton cycle, the potential cost reduction of the secondary cycle may help to offset the overall capital cost per kWe of a system coupled with the lead fast reactor (LFR) design [148].

Turbo-machinery	Temperature (°C)	Costs	vs. Steam Cycle	vs. Helium Cycle
Conservative	550	Capital Cost/kWe	0.865	1.0553
		Total Capital Cost	0.922	0.896
Conservative	650	Capital Cost/kWe	0.784	0.956
		Total Capital Cost	0.922	0.897
Conservative	700	Capital Cost/kWe	0.755	0.922
		Total Capital Cost	0.922	0.897
Best Estimate	550	Capital Cost/kWe	0.822	1.004
		Total Capital Cost	0.921	0.896
Best Estimate	650	Capital Cost/kWe	0.753	0.919
		Total Capital Cost	0.922	0.897
Best Estimate	700	Capital Cost/kWe	0.726	0.886
		Total Capital Cost	0.922	0.897

Table 7: Fractional costs of the different supercritical CO₂ cycle designs [54]

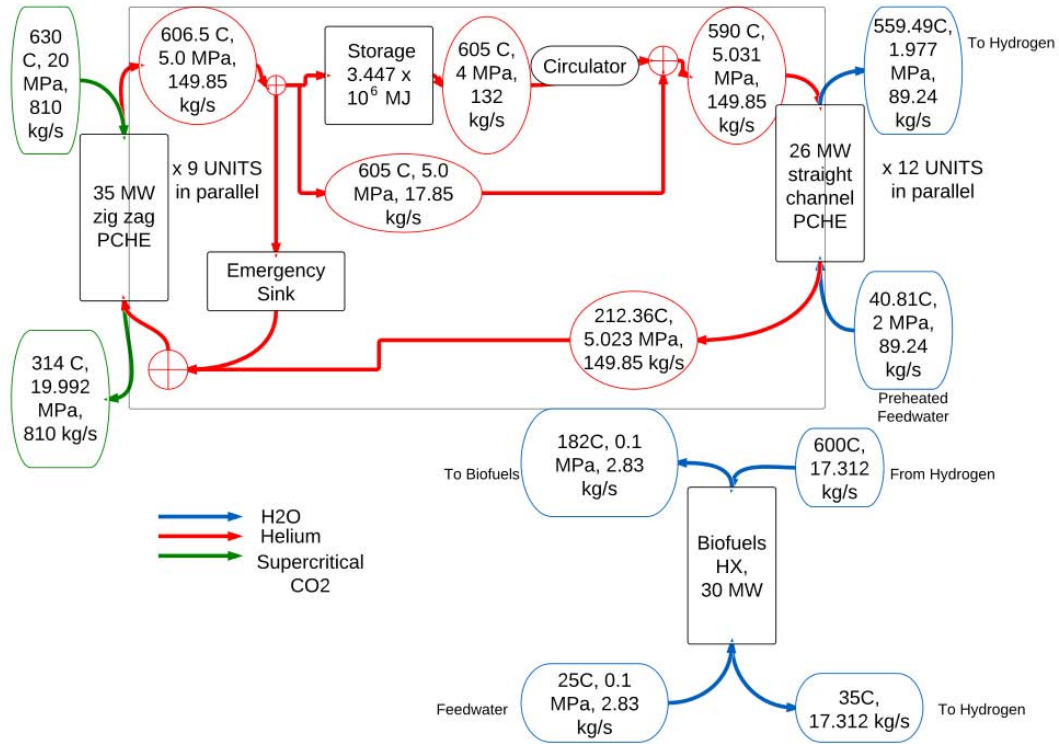


Figure 25: An overview of the process heat system

7 Process Heat

7.1 Process Overview

The process heat system is shown in Figure 25. Helium is the primary working fluid and is shown in blue in the figure. S – CO₂ and water are shown in green and red respectively. 149.85 kg/s of He circulate through the system.

The Process Heat system draws heat from the high temperature S – CO₂ to heat helium up to 606.55°C. This process takes place in the 9 PCHE1 heat exchangers connected in parallel to the S – CO₂ loop. 132 kg/s of the He flow then passes through heat storage and 17.85 kg/s is re-routed around it.

The helium going through the heat storage device experiences a pressure drop. A circulator located soon after the exit from heat storage is used to raise the pressure of the helium back to 5 MPa. Maintaining the low density working fluid at a high pressure improves its heat transfer properties. The He, now at 590°C passes through the 12 PCHE2 heat exchangers connected in parallel at the hydrogen plant. The PCHE2 heat exchangers are used to produce steam at 1.977 MPa and 559.49°C for high temperature steam electrolysis for the production of hydrogen.

Cooler He, now 212.36°C, returns to the PCHE1 heat exchangers where it is heated back up to 605.55°C.

An emergency heat sink is connected parallel to the PCHE1 heat exchangers to rapidly remove heat from the process heat system in the event of a reactor scram.

Not on the primary He loop (shown in red) is a ceramic heat exchanger that will be located at the hydrogen plant. This heat exchanger will be used to draw heat from the high temperature hydrogen and oxygen streams to produce steam at 182°C and 0.1 MPa for the Biofuels plant.

Following sections describe operating conditions and individual components of the process heat system in detail. Also presented in conclusion is a summary of the process heat system costs.

7.2 Heat Exchangers

7.2.1 Choice of Material and Working Fluid

In choosing a working fluid, key factors to consider are practicality, heat capacity, and viscosity. As Table 8 shows, helium has the most attractive working fluid properties for the system under consideration. PCHEs were chosen as two of the four heat exchangers (HXs) in the process heat system. PCHEs have a maximum operating pressure and temperature of 60 MPa and $\sim 900^\circ\text{C}$ [55] respectively. High achievable operating temperatures and pressures were decisive factors in the selection of PCHEs for drawing heat from the S-CO₂ and heating water at the hydrogen plant.

Fluid {5MPa; [200°C, 700°C]}	Heat Capacity [J/kg-K]	Viscosity [Pa-s]	Boiling Temperature (°C)
Carbon Dioxide (CO ₂)	[1,079.5, 12,37.8]	$[2.337 \times 10^{-5}, 4.064 \times 10^{-5}]$	263.94
Water/Steam (H ₂ O)	[4,476.1, 2,351.5]	$[1.35 \times 10^{-4}, 3.678 \times 10^{-5}]$	14.28
Helium (He)	[5,188.9, 5,190.6]	$[2.740 \times 10^{-5}, 4.533 \times 10^{-5}]$	-264

Table 8: Potential Working Fluid Properties [18]

The heat exchangers at the hydrogen plant that will make use of streams of superheated steam, hydrogen, and oxygen are yet to be designed and will be subject of future work. Table 9 shows a summary of the PCHE operating parameters. The following sections discuss each PCHE in further detail. The impact of various design parameters on PCHE volume, pressure drop, operating cost and capital cost is presented. Axial temperature, heat flux profiles, and cost estimations are shown and fouling related problems are discussed. A design strategy for the biofuels heat exchanger is outlined and future work is described.

	unit	PCHE1	PCHE2
Number of units		9	12
Heat rate/unit	MW	35	26
Total heat rate	MW	315	312
Location		S-CO ₂ loop	Hydrogen plant
PCHE type		zigzag channel	straight channel
Hot fluid		S-CO ₂	He
Flow configuration		counterflow	counterflow
Cold Fluid		He	H ₂ O
T hot in	°C	630	600
T cold in	°C	199.6	40.81
T hot out	°C	314.73	212.36
T cold out	°C	605.07	559.48
P hot in	MPa	20	5
P cold in	MPa	5	2
delta P hot	kPa	8.043	9.812
delta P cold	kPa	23.749	13.874
mass flow hot	kg/s	90	12.68
mass flow cold	kg/s	16.65	7.4371
v cold inlet	m/s	7.2625	0.0243
v hot outlet	m/s	1.0621	4.1990
Re hot		6,487.67	1,646.55
Re cold		1,177.35	492.34
htc hot	W/m ² -K	2398	850.01
htc cold	W/m ² -K	2,271.98	25,314.58
htc total	W/m ² -K	1,087.71	735
volume	m ³	0.9172	1.3
length	m	0.30699	1.09
d hot	mm	2	2
d cold	mm	2	2
pitch hot channel	mm	2.65	2.65
pitch cold channel	mm	2.65	2.65
number of hot channels		293,888	186,368
number of cold channels		293,888	93,184
plate thickness	mm	1.6	1.6
number of hot plates		1,312	832
number of hot plates		1,312	416

Table 9: Summary of PCHE results

Helium has the highest heat capacity of the examined working fluids, while its low viscosity makes pumping feasible by minimizing frictional losses and pump work. Its extremely low boiling temperature of -264.15°C means there is no chance of two phase flow entering the system, which could potentially damage fragile equipment like compressor blades. Another advantage of He is the fact that it is a noble gas and therefore chemically inert, which significantly reduces the prospect of a contaminated or corrosive working fluid. Although the price and availability of helium is questionable due to recent shortages [17], this non-technical reason was neglected for the purposes of this study.

In order to choose a HX material, one must consider the tensile strength, thermal conductivity, and coefficient of thermal expansion. Additionally, it is desirable to know a material's corrosion resistance, the ease with which it can be manufactured, and the anticipated lifetime. Alloy 617, a nickel-chromium-cobalt-molybdenum alloy, and Alloy 230, a nickel-chromium-tungsten-cobalt alloy, were investigated and the results of the research conducted are shown in Table 10.

	Alloy 230[14]	Alloy 617[15]
thermal conductivity, k at 650°C	21.4 $\frac{W}{m-K}$	23 $\frac{W}{m-K}$
tensile strength at 650°C	675 MPa	627 MPa
mean coefficient of thermal expansion	15.2 $\frac{\mu m}{mC}$ for 25-800°C	15.1 $\frac{\mu m}{mC}$ for 20-760°C

Table 10: Potential Materials for PCHE

To be rigorous, a calculation of maximum stress was performed using Equation 9 where p is the design pressure, r_{out} is the plate thickness, and r_{in} is the channel radius [54].

$$\tau_{max} = \frac{p}{2} \cdot \frac{r_{out}^2 + r_{in}^2}{r_{out}^2 - r_{in}^2} - 1 \quad (9)$$

For a PCHE with a plate thickness of 1.6 mm, a channel diameter of 2 mm, and experiencing a pressure of 20 MPa, the maximum stress is 21.57 MPa. However, the sharp edges of the semi-circular PCHE channels require the calculation of a radius of curvature for the channel edge at which the design stress of Alloy 617 is not be exceeded.

Equation 10 can be used to calculate the increase in stress due to the presence of a crack [144]. We treat the sharp edge of the semi-circular channel as the crack here, ρ is the radius of curvature of the crack and a is the crack length which is taken here to be the radius of the channel.

$$\sigma_{max} = \sigma \left(1 + 2\sqrt{\frac{a}{\rho}} \right) \quad (10)$$

Using Equation 10, we find that for radii of curvature less than 100 μ m, the design stress of Alloy 617 is exceeded. A radius of curvature 200 μ m produces a stress of 114MPa which is below the design stress of Alloy 617. It is proposed that PCHEs be fabricated such that the edges of the semi-circular channels have radii of curvatures 200 μ m or greater.

Actual operating pressures that the PCHE heat exchangers will encounter throughout the system range from atmospheric (\sim 0.1 MPa) to 20 MPa. System temperatures range from room temperature (\sim 20°C) to 606.5°C. By comparing results from Equation 9 with Table 10, it is evident that heat exchangers fabricated from either of these alloys would operate well below the design stress at all points within the system. Alloy 617 was ultimately chosen due to the demonstrated feasibility of their use in manufacturing PCHE heat exchangers [160].

7.3 PCHE Design

The impact of channel diameter, mass flow rate, and channel configuration (straight or zigzag channels) on the PCHE volume was studied. Table 11 outlines the impact of design choices on the PCHE volume and pressure drop across the HX. A discussion of design choices and their impact on the operating parameters is presented in Appendix of this report. A summary of the findings along with the implications of design choices on costs is discussed in this section.

Parameter	Change in parameter	Volume	Pressure drop	Capital cost	Operating cost
channel configuration	straight	↑	↓	↓	↓
	zigzag	↓	↑	↓	↑
hot fluid mass flow rate	↑	↓	↑	↓	↑
channel diameter	↑	↓	↑	↓	↑
number of PCHE units	↑	↓	↑	↑	↓

Table 11: Impact of design parameters on PCHE volume and pressure drop

The volume of a PCHE is sensitive to several design parameters. A straight channel configuration results in lower Reynolds numbers, lower Nusselt numbers, and poorer heat transfer for both the hot and cold fluids.

All other design parameters remaining unchanged, the PCHE volume for a straight channel PCHE is larger than that of a zigzag channel PCHE. Similarly, a higher mass flow rate for the hot fluid and a smaller channel diameter improve heat transfer and result in a reduction in the PCHE volume. For the same total power, having a larger number of PCHE units increases the total heat exchanger volume, but reduces the pressure drop.

The capital cost of the PCHE is inversely proportional to the PCHE volume. A lower PCHE volume results in a lower cost of fabrication as well as lower materials costs [54]. Operating costs are proportional to the hot fluid mass flow rate and pressure drop across the PCHE unit. A larger mass flow rate of the hot fluids reduces the amount of hot fluid available for electricity production and the associated addition of pumps and compressors further increases the capital cost of the plant.

In summary and as seen in Table 11, a higher mass flow rate, smaller channel diameter, and zigzag channel configuration minimize the PCHE volume, but adversely impact the pressure drop.

7.4 Process Heat PCHEs

The following sections present and describe the heat flux and temperature profiles of the process heat PCHEs. Small fluid channel velocities were chosen to minimize fouling and reduce pressure drops wherever possible.

7.4.1 PCHE1

As indicated in Table 9, PCHE1 is located at the S-CO₂ reactor loop and consists of 9 units of 35 MW zigzag channel PCHEs with a counterflow configuration. Zigzag channels were chosen for PCHE1 to increase flow turbulence, improve heat transfer, and reduce the heat exchanger volume. Zigzag channels, however, increase the pressure drops by making the flow more turbulent. A zigzag channel design was feasible for PCHE1 due to the friction factors for S-CO₂ and helium being lower than that of water. As helium passes through PCHE1, it is heated from 199.6°C to 605.07°C.

Axial Temperature Profiles

The temperature profiles of S-CO₂, He, the S-CO₂ channel wall, and the He channel wall are shown in Figure 26. The fluids in PCHE1 units do not undergo phase changes and the heat transfer mechanism is single phase forced convection. The highest wall temperature is 594.7 °C. Alloy 617 has been selected for heat exchanger fabrication because it has been proven acceptable for temperatures up to 982°C [1].

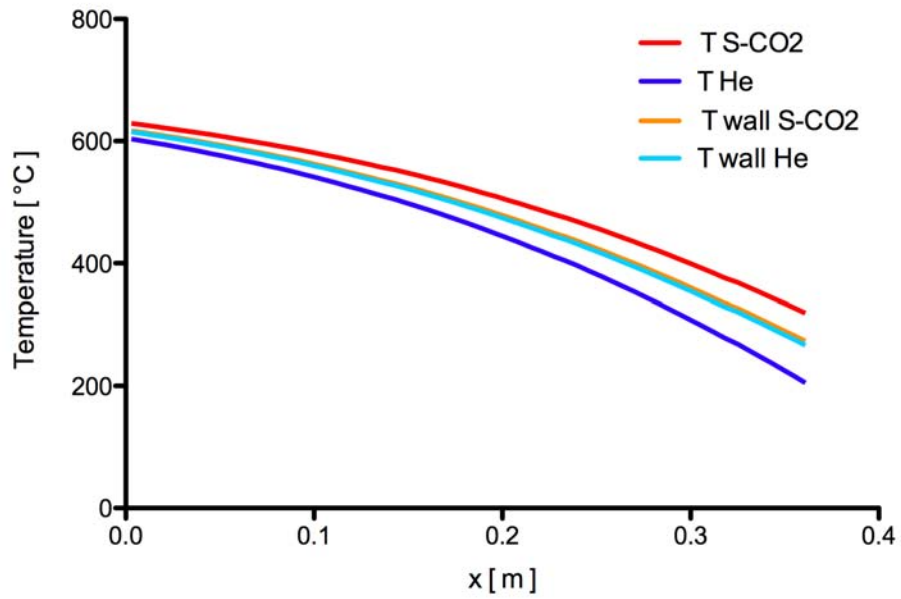


Figure 26: Axial temperature profile of the hot and cold fluid and hot and cold channel walls

Axial Heat Flux Profile

The axial heat flux profile for PCHE1 is shown in Figure 27. The heat flux is highest at the S-CO₂ inlet and He outlet (where $x = 0$) and decreases with an increase in the temperatures of the cold fluid (He). As a result of both fluids being in a single phase, there are no abrupt changes in the heat flux or heat transfer deterioration due to a transition from single to two-phase flow or due to surpassing critical heat flux.

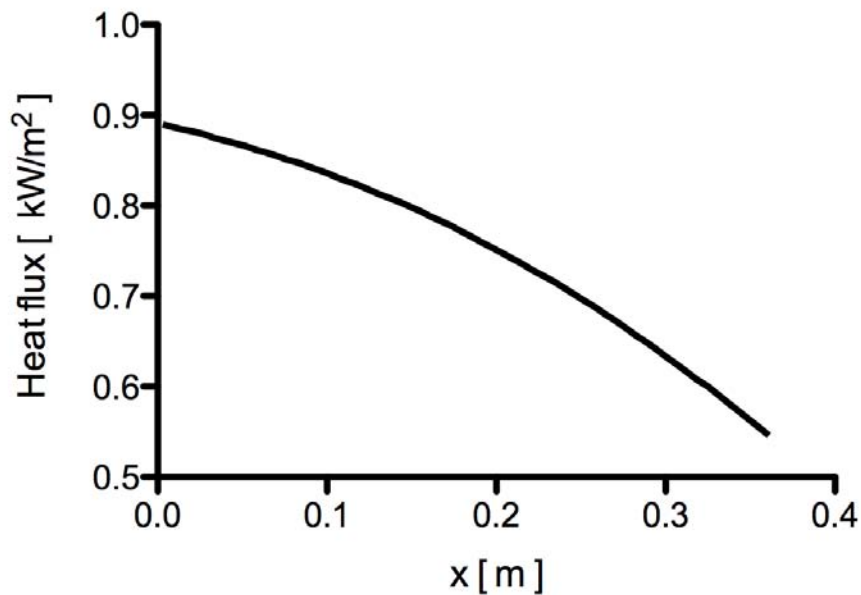


Figure 27: Heat flux profile for PCHE1

7.4.2 PCHE2

PCHE2, located at the Hydrogen plant, consists of 12 units of 26 MW, straight channel PCHEs with a counterflow configuration. Straight channels were chosen for PCHE2 to reduce the pressure drop on the water side. The HX with He in PCHE2 is used to heat water from 40.81°C to 559.48°C.

Flow Quality and Mass Flux

Flow stratification in a horizontal tube results in a critical heat flux value of zero on the vapor side [137]. Equation 11 [61] and Equation 12 [110] were used to calculate the minimum H₂O mass flux needed to prevent flow stratification.

$$G_{min} = \frac{\sqrt{gD\rho_g(\rho_f - \rho_g)}}{x} \left(\frac{1}{0.65 + 1.11X_{LT}} \right)^2 \quad (11)$$

where

$$X_{LT}^2 = \frac{(dP)_{fric}^l}{(dP)_{fric}^v} = \left(\frac{\mu_f}{\mu_g} \right)^{0.25} \left(\frac{1-x}{x} \right)^{1.75} \left(\frac{\rho_f}{\rho_g} \right) \quad (12)$$

The minimum mass flux as a function of flow quality is shown in Figure 28. In order to prevent flow stratification, a channel mass flux of 50 kg/m²-s was chosen for water.

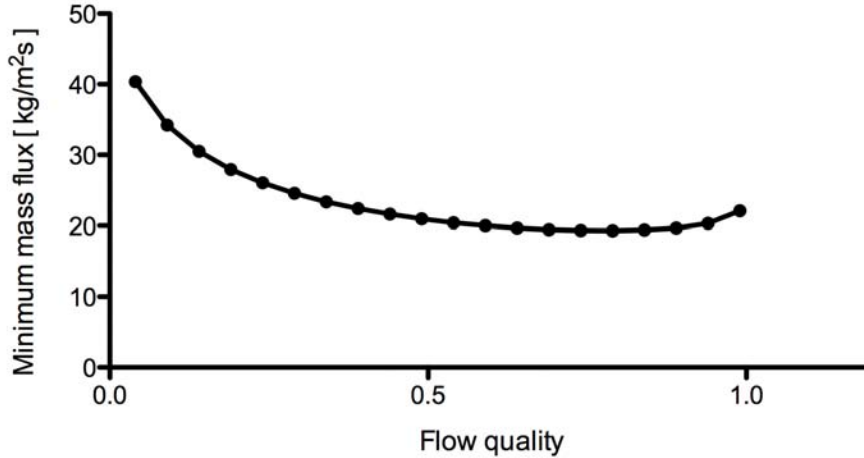


Figure 28: Minimum mass flux and flow quality in PCHE2

Axial Temperature Profile

The axial temperature profiles of He, H₂O, the He channel wall, and the H₂O channel walls are shown in Figure 29. PCHE2 also has a counterflow configuration which means that the He and water flow in opposite directions. The PCHEs were modeled using a nodal model implemented in Fortran [54].

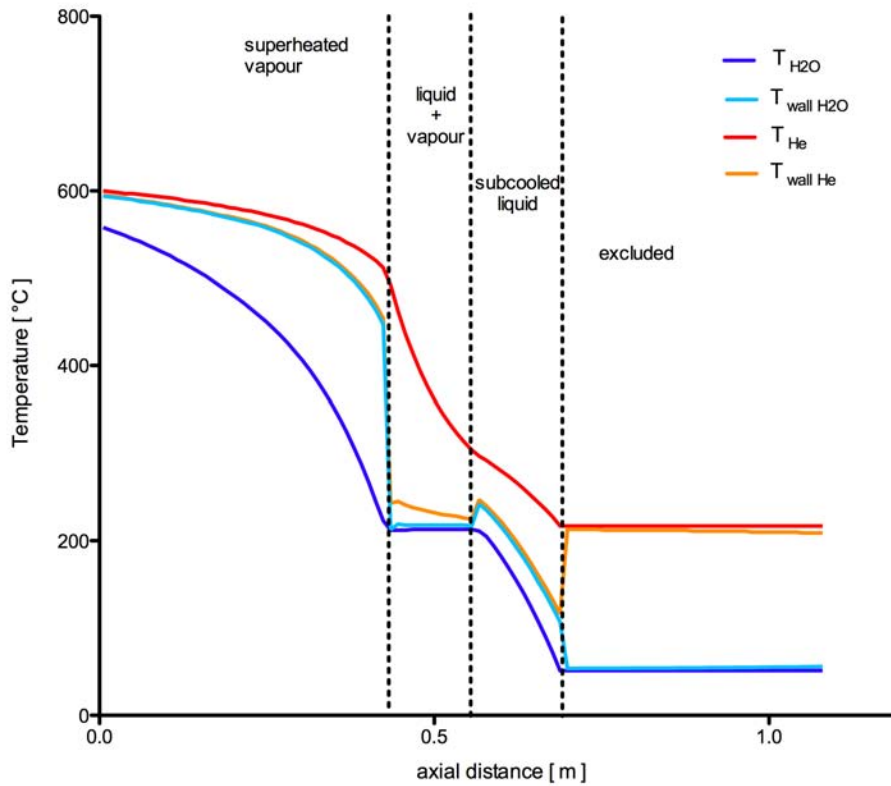


Figure 29: Axial temperature profile of PCHE2

The region marked as 'excluded' on Figure 29 is believed to be an artifact of the code due to the extremely small temperature changes that take place in this axial region. The region has been excluded from the PCHE2 geometry, however, this does not affect the inlet or outlet temperatures of either fluid. Besides the excluded region, the H₂O temperature profile is indicative of:

1. superheated vapor with single phased forced convection at the He inlet and H₂O outlet;
2. two phase flow with nucleate and transition boiling;
3. and sub-cooled liquid with single phased forced convection at the He outlet and H₂O inlet.

The sharp gradient of the He temperature in the two phase region is indicative of the high heat transfer coefficients for nucleate boiling. The large temperature swings seen in this HX are likely to result in a reduced heat exchanger design life due to thermal stresses. Future work on this HX will involve investigating heating H₂O in PCHEs arranged in series, instead of in a single PCHE. Shell-and-tube heat exchangers will also be investigated further as a potential alternative design choice.

Axial Heat Flux Profile

The axial heat flux profile for PCHE2 is shown in Figure 30. The heat flux in the sub-cooled region (which begins at 0.68 m and continues to the left on the x-axis) is seen to decrease as the water approaches nucleate boiling. This can be explained using the temperature profiles in Figure 29. In moving away from the He outlet and H₂O inlet, the temperature gradient across the hot and cold fluids decreases. This decrease in the temperature gradient manifests itself as a lower heat flux. However, with the creation of bubbles and the onset of nucleate boiling, the heat transfer properties are greatly improved and the heat flux increases and reaches a maximum near the end of the two phase region.

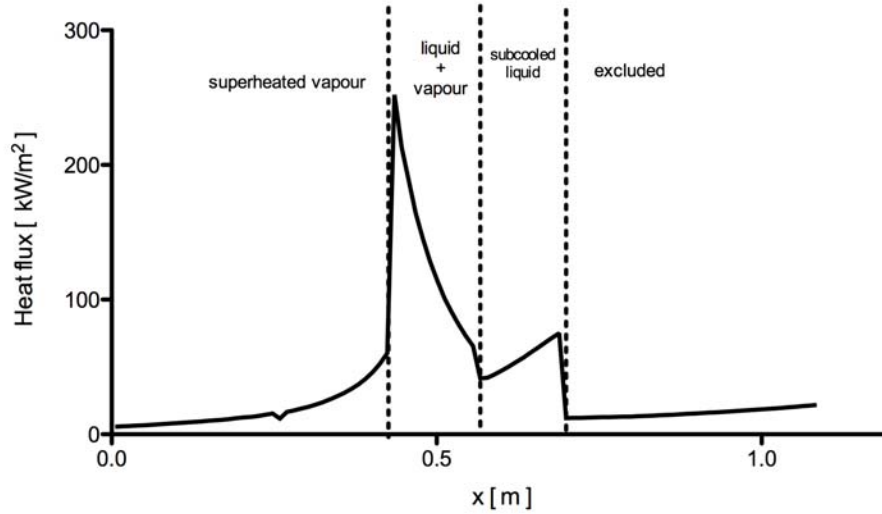


Figure 30: Heat flux profile of PCHE2

The heat flux for single phase forced convection in the superheated vapor decreases on approaching the He inlet and H₂O outlet. This can again be attributed to a decreasing temperature gradient across the hot and cold channels.

In Figure 30, the largest heat flux, 252 kW/m², is seen to occur near the end of the two phase region at a flow quality between 0.85 and 0.9. According to the Groeneveld look-up tables, at a pressure of 2 MPa, mass flux of 50 kg/m²-s, and a flow quality between 0.85 and 0.9, the critical heat flux is between 658 kW/m² and 373 kW/m²[65]. Although the CHF values in the Groeneveld lookup tables are for circular channels, they are well above the largest heat flux in the 26 MW PCHE. Therefore, the operating conditions for PCHE2 provide a significant margin to CHF.

Future work should address determining correction factors for the semicircular PCHE channels in order to precisely compute values for CHF.

7.4.3 PCHE Conclusions

A zigzag channel configuration was chosen for PCHE1 and a straight channel configuration for PCHE2. Straight channels were chosen for PCHE2 in order to minimize pressure drops on the water side. The ideal configuration for PCHE2, however, would be a zigzag channels for He and straight channels for H₂O. This design was unable to be completed in the design timeframe given due to limitations of the computational model. Future work should explore this option and also that of carrying out the heat exchange between He and H₂O in multiple stages of PCHEs or in shell-and-tube HXs. A Matlab model for sizing a counter flow shell-and-tube HX with He in the shell and H₂O in tubes is being developed and will be available for future studies.

7.5 Fouling

Fouling adversely affects both the performance and the design life of a heat exchanger. Deposition of impurities in the flow passages results in a reduction of the equivalent diameter and reduction of the heated perimeter. This increases the pressure drop across the heat exchanger and lowers its heat rate [80].

Fouling is exacerbated by high fluid velocities, rough surfaces and impurities in the fluid. PCHE1 is a S-CO₂/He HX and PCHE2 is a He/H₂O HX. Although small amounts of impurities will be present in both He and S-CO₂, the PCHE channels for these fluids are likely to experience less fouling than those containing water [78]. The addition of chlorine to the feedwater and the use of 200 μm strainers can counter biofouling [109]. Addition of chlorine however, might create the problem of separating chlorine from the steam before using the steam for high temperature electrolysis for hydrogen production.

Table 12: Steam/hydrogen and oxygen streams from the hydrogen plant

Property		Unit
Inlet temperature	836	C
Outlet temperature	71	C
H ₂ O mass flow rate	17.57	kg/s
H ₂ mass flow rate	7.9	kg/s
O ₂ mass flow rate	62.6	kg/s
Heat rate from H ₂ O/H ₂ stream	158.21	MW
Heat rate from O ₂ stream	49.29	MW

PCHE fouling studies indicate no change in HX effectiveness, but a 55% higher pressure drop for operating times of 500-660 hours [109]. However, an 18 month fuel cycle will require 12,960 PCHE operating hours. The pressure drop related effects of fouling can therefore be mitigated by installing redundant PCHE units for both PCHE1 and PCHE2, rerouting flow, and carrying out chemical cleaning on the offline system during the reactor fuel cycle. The other option is to increase the pumping and compression inputs to counter the effects of larger pressure drops. However, choosing the latter option will require quantifying thermal effectiveness deterioration over PCHE operating times of the order of 12,960 hours, which is not a simple task.

7.6 Heat Exchanger at Biofuels Plant

Two heat exchangers may be used to extract heat from the steam + H₂ and O₂ streams. Another option would be to not utilize the heat from the fluid streams at the hydrogen plant. This would require the use of condensers that dump this heat to the atmosphere or a body of water. This would also increase the energy requirement of the Biofuels plant. A rigorous cost-benefit analysis of the different design options is needed here and may be the subject of future work.

The following section describes prospective materials and proposes a methodology for designing the HXs as well as possible limitations.

Prospective Materials

Several experimental studies focused on strength, oxidation resistance, and thermal fatigue have been conducted to evaluate the use of reaction bonded silicon carbide (RBSiC) and siliconised silicon carbide (SiSiC) as materials for HX fabrication. These experimental studies evaluated the use of RBSiC and SiSiC by fabricating and testing a cross flow HX for recovering waste heat from combustion products of a gas fired furnace. While both materials demonstrated good oxidation resistance, exposure to reducing environments caused the formation of pits on the SiC surface. Furthermore, both SiC materials evaluated are capable of withstanding exposure to 1200°C. However, in comparison to Alloy 617, which will be used for fabricating PCHE1 and PCHE2, both ceramics have lower thermal conductivities. RBSiC demonstrated superior temperature strength and oxidation properties[103].

Heat Rates Extractable of Fluid Streams from the Hydrogen Plant

Table 12 shows the properties of the fluid streams at the Hydrogen plant. These streams may be used to produce steam at 182°C for use at the biofuels plant. The thermal efficiency of high temperature gas furnaces can be increased by recovering heat from the combustion products before exhausting them to the atmosphere. As indicated earlier, proposals for heat recovery include the use of ceramic heat exchangers fabricated using RbSiC or SiSiC.

Choosing a Heat Exchanger Design

We propose that both shell and tube designs as well as cross flow ceramic HX designs be evaluated for this purpose. The former have lower effectivenesses but are cheaper to fabricate, the latter due to higher

effectivenesses require the use of fewer materials but are also likely to have higher fabrication costs. Further, the narrower channels of a cross-flow heat exchanger are likely to create fouling problems.

If it is found that the shell and tube HX is the design of choice, it is proposed that smaller shell and tube units be fabricated and connected in parallel with an adequate number of redundant units. This would allow periodic maintenance while keeping the Process Heat system online.

Proposed Design Methodology

We propose developing matlab codes for evaluating both the cross-flow and shell and tube designs.

For each design, it is proposed that a hot and cold channel be selected as the unit cell. The matlab model should split the channel into several nodes, use appropriate fluid properties at each node and keep track of fluid temperatures and nodal heat transfer rates. This methodology is similar to that employed by the model used in this work for designing Process Heat PCHEs.

The heat extractable from either of the streams is sufficient to produce the steam required for the biofuels plant. However, use of the steam/hydrogen stream adds complexity to the design problem as the slip ratio for this stream can no longer be approximated as being equal to 1 once the steam condenses.

The considerations outlined here should inform future work for designing this heat exchanger.

7.7 Heat Sink

7.7.1 Purpose, Location, and Components

In the event of a core shutdown, heat will still need to be removed from plant components, therefore, helium will still be pumped for some time. The emergency heat sink forms a loop with the PCHE at the core and exists in parallel to the loop containing heat storage and the heat exchangers for the biofuels and hydrogen facilities. Valves directing helium out of the core heat exchanger and into the heat storage facility would redirect the flow into this heat sink where it would interact with a plate type heat exchanger that has seawater from the Gulf of Mexico as its cold fluid. Such a heat exchanger should be derivative of the marine heat exchangers of Sondex Inc [19], as well as made of titanium to prevent seawater corrosion. After losing heat to the seawater, the helium will be pumped back to the core heat exchanger.

7.7.2 Heat Rate and Design

Based on the decay heat calculation [88] shown in Equation 26, the 3575 MWt nuclear reactor is expected to produce a decay heat of 120 MW after 30 seconds, with 40 MW of decay heat being produced one hour after shutdown. In one hour after a shutdown from full power, the core has produced 179 GJ of decay heat which averages to around 50 MW.

$$Q_{dot}(t) = Q_{dot,0} \cdot 0.066 \cdot t^{-0.2} \quad (13)$$

Obviously not all of this decay heat is going through the process heat system. A more realistic analysis takes the maximum heat from the core PCHE as $Q_{dot,0} = 35 \text{ MW} \cdot 9 \text{ units} = 315 \text{ MW}$. Average heat in the one hour after shutdown is 5 MW. Following the lead of the San Onofre Nuclear Generating station in southern California, the maximum allowable temperature difference between the seawater inlet and outlet temperatures was set at 19°F (10°C) [22]. Given water's heat capacity of approximately $4190 \frac{\text{J}}{\text{kg-K}}$ in the temperature range of interest and the heat transfer rate seen in Equation 27, a seawater flow rate of 120 kg/s, or 455 gallons/s is needed.

$$Q_{dot} = m_{dot} \cdot c_p \cdot \Delta T \quad (14)$$

7.7.3 Environmental Concerns

The Environmental Protection Agency's Clean Water Act Section 316 *Thermal Discharges* states that the location, design, construction, and capacity of cooling water intake structures must reflect the best technology available for minimizing adverse environmental impact [2]. The goal of limiting thermal pollution can be approached in multiple ways. Heat treatments that reduce fouling should be performed gradually to drive

away marine life - otherwise the local fish would experience a thermal shock and some would die. Limiting the seawater temperature increase, taking in colder water from deep, offshore locations, and utilizing diffusers at the outlet to recombine the seawater and reach thermal equilibrium quicker are all steps that help preserve the local environment.

7.8 Process Heat System Costs

7.8.1 PCHE

The cost of a PCHE is proportional to the metal fraction f_m . The metal fraction for PCHE1 and PCHE2 was calculated using Equation 28 and was found to be 62.95% [54].

$$f_m = 1 - \frac{\pi d^2}{8Pt} \quad (15)$$

Following the calculation of f_m , a methodology similar to Dostal's [54] was used to estimate the capital cost of the PCHEs. These capital costs are outlined in Table 18. The cost of Alloy 617 was not available at the time of this calculation and a \$30/kg value of steel as quoted by Heatric [54] was used for this cost estimation. Alloy 617 costs have been requested from Huntington Metals and these cost calculations will be updated when the Alloy 617 costs become available.

HX	Material	Volume (m ³)	Weight (kg)	Cost (K\$)
PCHE1	Alloy 617	8.2548	69,010.128	2,070.30384
PCHE2	Alloy 617	15.6	130416	3,912.48

Table 13: PCHE capital cost

7.8.2 Circulator

The circulator will have to be custom built so the exact price is not known, but currently manufactured circulators that accomplish similar goals cost around \$250,000.

7.8.3 Piping

The cost per meter of the entire piping apparatus (from Alloy 625 all the way out to the Gemcolite 2600) is approximately \$36,507. Therefore, the total cost for 40 m of piping (the total amount that will be in the system) is around \$1.46 M.

7.9 Heat Storage Details

Heat will be stored in order to be able to keep the LBE molten for an extra two weeks after the core stops producing enough decay heat to do so on its own. A latent heat thermal energy storage system was chosen instead of sensible heat, as it can release heat at a constant temperature and can store more energy per unit mass of storage material [52]. Some widely used categories of phase change materials (PCMs) include paraffins, salt hydrates, and metals. The PCM selected must have a melting point in the desired operating temperature range of the system [27]. This was the most important criteria in picking a PCM for the system, as the operating temperature is dependent on the heat provided by the core and demanded by the hydrogen and biofuels plants.

The location of the storage device is to be directly after the heat exchanger with the core secondary loop where the temperature of the system is approximately 500-600°C. Molten salts - namely, chlorides and carbonates - were therefore examined as potential PCMs as the range of melting temperatures for molten salts was most appropriate for this system [73] and other categories of PCMs melt at a lower temperature than is desirable. Lithium chloride, LiCl, was eventually chosen as it is possible to push the operating temperature of the system just above the melting point of LiCl, allowing sensible heat storage past the melting point to be neglected.

7.9.1 Lithium Chloride

LiCl was chosen as the PCM as its melting point of 605°C was most appropriate for the process heat system. This is also matched to the outlet temperature of the core secondary loop (606.5°C). A list of the relevant properties of LiCl can be seen in Table 14. The heat capacities and latent heat of fusion were calculated using the Shomate equation for LiCl [18].

Property	Value
Melting Point	605°C [24]
Δh° of Fusion	470 kJ/kg [18]
c_p (solid)	1.132 kJ/kg-K [18]
c_p (liquid)	1.538 kJ/kg-K [18]
k (thermal conductivity)	0.534 W/m-K [112]
Density	2,068 kg/m ³ [18]

Table 14: Relevant physical properties of LiCl

As can be seen from Table 14, the heat capacity of LiCl is significantly less than the latent heat of fusion. Heating the salt from 603°C to 604°C therefore stores less than 0.1% of the energy that heating from 604°C to 605°C because of the phase change at 605°C.

The heat capacity of the solid is important because, initially, the LiCl will need to be heated up from room temperature (~20°C) to 605°C. This involves storing heat as sensible heat, so it is better for the heat capacity of LiCl to be smaller as it will involve less time and energy to heat the LiCl up to its melting point. This will take around 660 kJ/kg of LiCl, which is significant compared to the 470 kJ/kg stored in the phase change. However, it is only important to the system design that there is negligible sensible heat storage after the melting point. When the reactor is shut down and the primary loop needs the stored energy to keep the lead bismuth molten, the latent heat, which is a higher quality heat than the sensible heat, is available immediately, as opposed waiting for the material to cool before reaching the melting point. The sensible heat stored between the melting point and the operating temperature of 606.5°C can be ignored as it is less than 0.5% of the energy stored as latent heat.

7.9.2 Alloy 20

Because the PCM melts, it cannot have direct contact with the helium flowing through the system as this could result in flow of the molten PCM and contamination of the loop. Therefore, the PCM must be contained in a cladding. It is important to select a material that is chemically compatible with the PCM. The use of a molten salt means corrosion is a potential problem [151] because molten salts are good conductors of

electricity. Alloy 20, a nickel-chromium-molybdenum alloy, was chosen as the containment material in order to alleviate this problem as it is compatible with LiCl [119] due to its extreme resistance to chloride ion corrosion [12]. The chemical composition of the alloy can be seen in Table 15.

	Minimum (%)	Maximum (%)
Nickel	32.5	35.0
Chromium	19.0	21.0
Molybdenum	2.0	3.0
Manganese	none	2.0
Copper	3.0	4.0
Silicon	none	1.0
Carbon	none	.06
Sulfur	none	.035
Phosphorus	none	.035
Niobium	none	1.0
Iron	balance	balance

Table 15: The composition of Alloy 20. Adapted from [11].

7.9.3 System Design

A custom heat exchanger was designed for the purpose of storing heat in the LiCl. The design, which was inspired by plate type heat exchangers, can be seen in Figure 31.

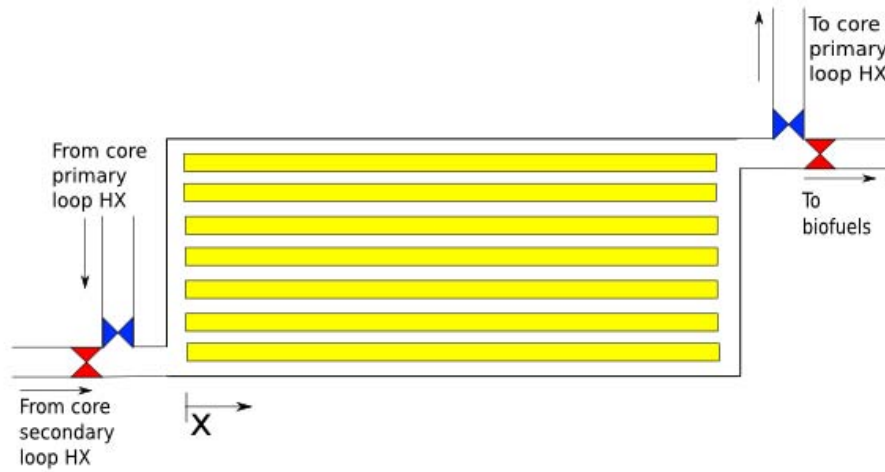


Figure 31: The basic design of the storage heat exchanger

The LiCl will be stored in slabs, stacked on top of each other with gaps for the helium to flow through, and contained by Alloy 20. A more detailed view can be seen in Figure 32.

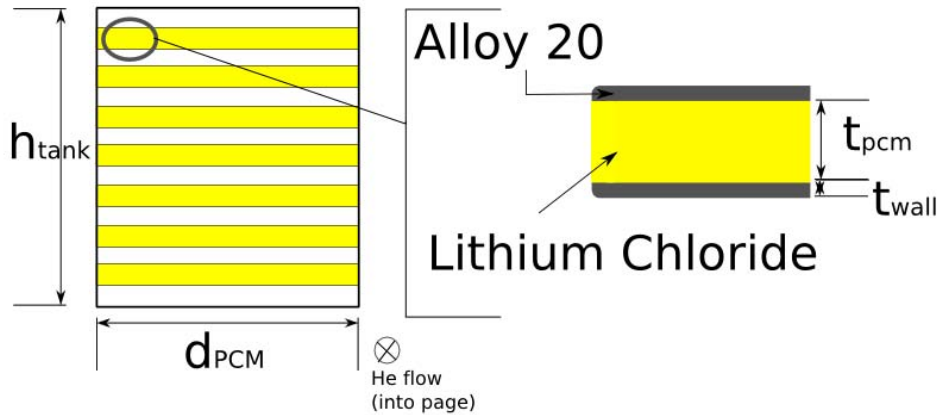


Figure 32: A view of the cross-sectional flow area of the storage heat exchanger.

The overall dimensions of the tank will be 20 m long, 18 m wide, and 11.41 m tall. There will be 10 slabs of LiCl, with each being 20 m long, 18 m wide, and 1.13 m tall. Each slab will be contained by Alloy 20, with a thickness of 1 cm (dimension t_{wall} in Figure 32). The gap between slabs will be 1 cm. There will be a total of 11 gaps, allowing the helium to flow both over and under the top and bottom slabs of LiCl.

Assumptions

The heat exchanger was designed such that each of the slabs of LiCl could be treated equally. A number of assumptions were made (refer to Figure 32 for dimensions):

1. Above the melting point, heat is stored in the LiCl only as latent heat; sensible heat is neglected. Only energy stored as latent heat will be used for energy storage.
2. No convection occurs within the LiCl; heat transfer within the LiCl occurs through conduction only.
3. $t_{PCM} \ll L_{PCM}$; the end effects of each slab can be ignored.
4. The helium temperature is isothermal for any given value of y .
5. During shutdown, the LBE enters the shell-and-tube heat exchanger at 140°C; heating it to 150°C is sufficient to keep it molten throughout the primary loop.
6. The storage will be used to keep the LBE molten for up to two weeks.
7. The average mass flow rate of the LBE during shutdown is 1,900 kg/s.
8. There are no transmission losses between the storage heat exchanger and the shell-and-tube heat exchanger with the primary loop.

Storage Layout: Charging

When the storage system is being charged, the hydrogen and biofuels plants will be valved off from the main loop so the helium cycle through the core heat exchanger and the storage device only. Figure 33 shows this layout graphically. A preheater will use electricity from the grid to heat the incoming helium to 705°C, allowing the charging time to be drastically reduced from on the order of years to on the order of days.

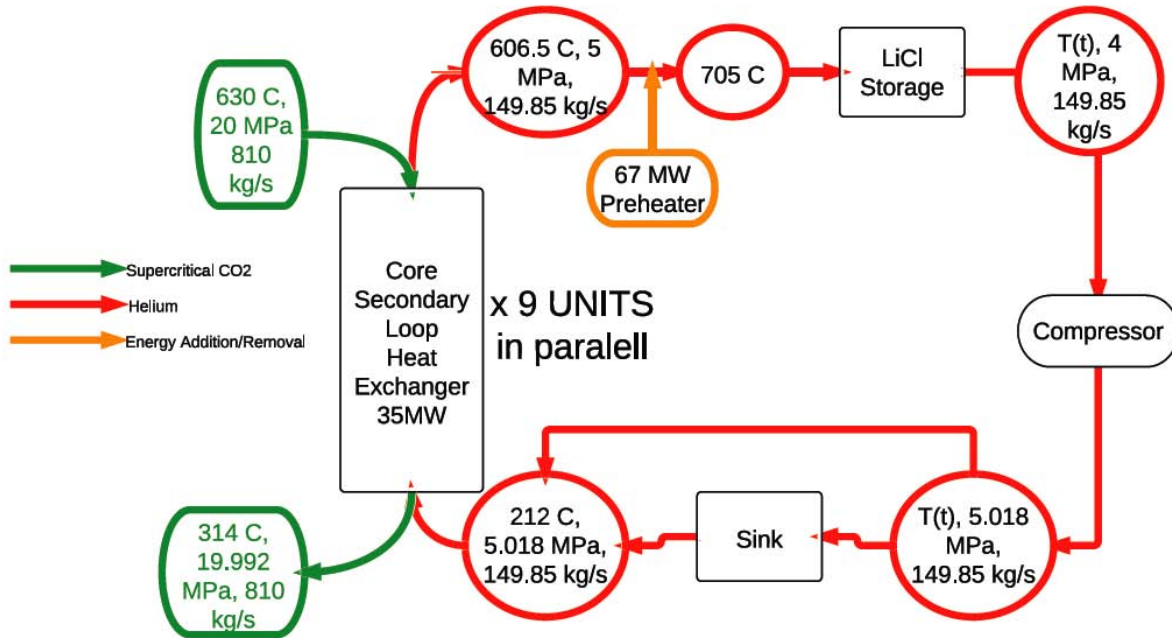


Figure 33: The charging layout for the storage heat exchanger.

Storage Layout: Discharging

When the system is discharging, the main loop will be valved off and the valves to the primary loop will open as shown in Figure 34. Helium will flow through the loop between the storage heat exchanger and a shell-and-tube heat exchanger with the core's primary loop.

[40].

$$\Delta p_{fric} = \int f \frac{x}{D_e} \frac{G^2}{2\rho} dx \quad (16)$$

To find the friction factor, f , the roughness of the slabs was estimated using the value for roughness of stainless steel alloys [43]. The roughness and Reynold's number were used to find the value of f on Moody's chart [108]. The value of f was found to be 0.035. The pressure drop due to friction was calculated to be 0.778 MPa.

The form losses can be calculated according to Equation 17 where k_{form} is the form loss coefficient and v_1 and v_2 are the velocities directly upstream and downstream of the location of interest, respectively [40].

$$\Delta p_{form} = \int k_{form} \frac{G^2}{2\rho} dx + \rho \frac{v_2 - v_1}{2} \quad (17)$$

The form acceleration losses, the pressure drop due to the velocity, and density change were calculated for the inlet and the outlet. The density was calculated using Equation 18 where $R_{specific}$ is the specific gas constant of helium, $2080 \frac{J}{kg-K}$.

$$p = \rho R_{specific} T \quad (18)$$

The form acceleration losses were calculated to be -0.001 MPa, which are negligible compared to the friction drop.

If the pipes are constructed so that there are no abrupt changes in pipe shape and area, the contribution due to the form loss coefficient should be small, although not negligible, in comparison to the friction coefficients. An estimate of 1 MPa will be used as the total pressure drop across the storage heat exchanger. Due to this large pressure drop, a circulator will be located directly downstream of the storage device to raise the helium back up to its normal operational pressure of 5 MPa.

Charging Time

The preheater will create a greater difference in temperature between the melting point of LiCl and the temperature of the heating fluid. For this geometry of flat slabs of LiCl, the distance between the phase front and the heating surface can be described using Equation 19 where k is the thermal conductivity of the LiCl in W/m-K and Δh_f is the latent heat of fusion in J/m³ [104].

$$s_{charge}(t) = \sqrt{2t \cdot \frac{k \cdot (T_{melt} - T_{surf})}{\Delta h_f}} \quad (19)$$

Setting s to equal 0.565 m (half the thickness of the PCM as the phase front will be propagating in from both sides), the time required to fully charge the PCM is equal to 2.9×10^6 s, or 33 days and 12 hours. However, this complete charging time won't be needed every time the plant is started up; the PCM will be insulated such that it stays warm for at least a month during the refueling period, as this insulation is necessary for the purpose of keeping the LBE molten a month after shutdown.

Discharging

The heat flux density (power/unit area) of the storage device can be calculated using Equation 20 where q'' is the total power divided by the total surface area, k is the thermal conductivity of the LiCl in W/m-K and s is the distance between the phase front and the surface of the LiCl [104]. This derives from the thermal resistance model of heat transfer.

$$q''(t) = \frac{k \cdot (T_{melt} - T_{surf})}{s} \quad (20)$$

The temperature of the helium can be solved as a function of x as seen in Equation 21 where $\beta = \frac{\pi h D_e}{m_{dot} c_p}$ [23].

$$\frac{T_0 - T(x)}{T_0 - T_{He,in}} = e^{-\beta x} \quad (21)$$

T_0 is 605°C as this is the temperature of the PCM when melted. The temperature difference of the helium will thus be equal to the power absorbed divided by the mass flow rate and heat capacity. Using Equations 20-21, an appropriate helium inlet temperature (and therefore outlet temperature) can be solved for that will allow for the correct amount of power to be drawn from the storage during discharge.

Combining Equations 20-21 and integrating over both the length of the PCM (20 m) and the time for discharge (1,209,660 s) gives Equation 22.

$$\int_0^{1209660s} \int_0^{20m} \frac{k_{LiCl}(T_{melt} - [T_{melt} - T_{He,in}]e^{-\beta x})}{\sqrt{2t \frac{k_{LiCl}[(T_{melt} - T_{He,in})e^{-\beta x}]}{\Delta h_f}}} \cdot dx \cdot dt = \frac{E_{stored}}{n_{slab} w_{LiCl}} \quad (22)$$

The total energy stored is divided by the width of the LiCl slabs because the total power density was integrated only in one dimension: the length of the LiCl slab. By plugging in the known values, the inlet temperature of the helium that allows the storage to be discharged over two weeks can be found. The inlet temperature of the helium was found to be 419.73°C; this inlet temperature removes all the latent energy from the storage over the course of two weeks.

As the phase front moves, for a constant helium inlet temperature, the power drawn from the storage will change. The outlet temperature of helium and the power exchanged to the LBE will therefore also vary with time. Thus, it will be necessary to vary the mass flow rate of the LBE in order to keep the change in temperature of the LBE equal to 10°C. Integrating the power exchanged in the LBE-helium heat exchanger over the two week discharging period must give the total energy used from storage during discharge as shown in Equation 25.

$$\int_{0s}^{1209660s} m_{dot}(t) \cdot c_{p,LBE} \cdot \Delta T \cdot dt = E_{stored} \quad (23)$$

The mass flow rate of the LBE at any given time should be equal to the power being released by the storage at that time divided by the heat capacity of LBE and the change in temperature of the LBE (10°C). The power being released by the storage at any given time can be found by integrating only over x in Equation 22, and then multiplying by the number of slabs and the width of the slabs:

$$q(t) = \left[\int_0^{20m} \frac{k_{LiCl}(T_{melt} - [T_{melt} - T_{He,in}]e^{-\beta x})}{\sqrt{2t \frac{k_{LiCl}[(T_{melt} - T_{He,in})e^{-\beta x}]}{\Delta h_f}}} \cdot dx \right] \cdot n_{slabs} \cdot w_{LiCl} \quad (24)$$

As everything in this equation is known, the mass flow rate of the LBE as a function of time can be evaluated:

$$m_{dot}(t) = \frac{q(t)}{c_{p,LBE} \cdot \Delta T_{LBE}} = \frac{9.986 \cdot 10^6}{\sqrt{t}} \quad (25)$$

This function is plotted in Figure 35.

Safety

If one of the slabs were to burst, the helium loop would be contaminated with molten LiCl. While the PCM cladding was chosen to be resistant to corrosion with LiCl, the piping material and the heat exchangers in the rest of the main loop were not. Contamination of the rest of the loop could also result in LiCl solidifying in the pipes because the temperature of the helium drops below the freezing point of the LiCl as it moves through the heat exchangers to the biofuels and hydrogen facilities.

Therefore, it is important that if a slab opens and molten LiCl is exposed to the helium that the storage device is isolated and the helium flow is rerouted around the storage device. The pressure throughout the interior of the slabs and the flow of the LiCl within the slab should be monitored; if a slab were to burst, the pressure will drop and molten LiCl will flow towards the leak, revealing that the slab has begun to leak.

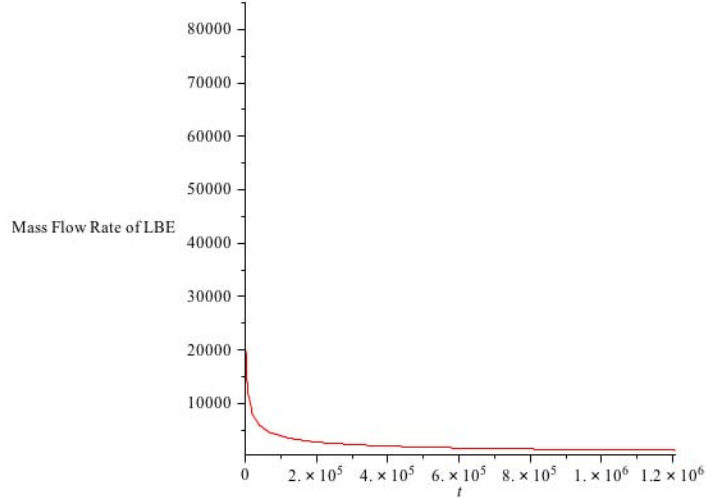


Figure 35: The mass flow rate of the LBE as a function of time when the storage device discharges.

In such an event, the storage device can be valved off and the helium flow directed to another pipe flowing towards the hydrogen and biofuels plants (which has been incorporated into the process heat design as seen in Figure 25). This will also result in less of a pressure drop as the pressure drop of the storage heat exchanger is large compared to that of the piping. Therefore, in the event that the storage is valved off, the circulator that is located directly after storage should be shut off.

7.9.5 Heat Storage Summary

Result	Value
Mass of LiCl	8.41×10^6 kg
Volume of LiCl	4068 m ³
Total Stored Energy (Latent)	3.9539×10^6 MJ
Pressure Drop (friction)	0.778 MPa
Pressure Drop (form acceleration)	-0.001 MPa
Total Pressure Drop (Estimate)	1.0 MPa
Reynolds Number - Helium	7,152.2
Charging Time	33 days, 12 hours
Discharging Time	2 weeks
Helium Inlet Temperature (Charging)	705°C
Helium Inlet Temperature (Steady State)	606.5°C
Helium Inlet Temperature (Discharging)	419.73°C
Mass Flow Rate (Charge/Discharge/Steady)	132 kg/s

Table 16: A summary of the heat storage results

7.10 Circulator

The circulator should be located in the area with the greatest pressure drop in the system in order to recuperate the helium pressure. For this design, a circulator will be placed at the 1 MPa drop immediately following the heat storage system as shown in Figure 25. Here, the pressure needs to increase from 4 MPa back up to 5 MPa, therefore, the circulator will need to have a compression ratio of 1.25. Since the mass flow rate is high (149.85 kg/s) in addition to the pressure ratio, there are no currently manufactured circulators on the market to place in this system. A custom circulator [87] is a possibility for this plant. This hybrid circulator is expected to use around 4 MW due to its large mass flow rate and pressure ratio.

7.11 Heat Sink

7.11.1 Purpose, Location, and Components

In the event of a core shutdown, heat will still need to be removed from plant components, therefore, helium will still be pumped for some time. The emergency heat sink forms a loop with the PCHE at the core and exists in parallel to the loop containing heat storage and the heat exchangers for the biofuels and hydrogen facilities. Valves directing helium out of the core heat exchanger and into the heat storage facility would redirect the flow into this heat sink where it would interact with a plate type heat exchanger that has seawater from the Gulf of Mexico as its cold fluid. Such a heat exchanger should be derivative of the marine heat exchangers of Sondex Inc [19], as well as made of titanium to prevent seawater corrosion. After losing heat to the seawater, the helium will be pumped back to the core heat exchanger.

7.11.2 Heat Rate and Design

Based on the decay heat calculation [88] shown in Equation 26, the 3575 MWt nuclear reactor is expected to produce a decay heat of 120 MW after 30 seconds, with 40 MW of decay heat being produced one hour after shutdown. In one hour after a shutdown from full power, the core has produced 179 GJ of decay heat which averages to around 50 MW.

$$Q_{dot}(t) = Q_{dot,0} \cdot 0.066 \cdot t^{-0.2} \quad (26)$$

Obviously not all of this decay heat is going through the process heat system. A more realistic analysis takes the maximum heat from the core PCHE as $Q_{dot,0} = 35 \text{ MW} \cdot 9 \text{ units} = 315 \text{ MW}$. Average heat in the one hour after shutdown is 5 MW. Following the lead of the San Onofre Nuclear Generating station in southern California, the maximum allowable temperature difference between the seawater inlet and outlet temperatures was set at 19°F (10°C) [22]. Given water's heat capacity of approximately $4190 \frac{\text{J}}{\text{kg-K}}$ in the temperature range of interest and the heat transfer rate seen in Equation 27, a seawater flow rate of 120 kg/s, or 455 gallons/s is needed.

$$Q_{dot} = m_{dot} \cdot c_p \cdot \Delta T \quad (27)$$

7.11.3 Environmental Concerns

The Environmental Protection Agency's Clean Water Act Section 316 *Thermal Discharges* states that the location, design, construction, and capacity of cooling water intake structures must reflect the best technology available for minimizing adverse environmental impact [2]. The goal of limiting thermal pollution can be approached in multiple ways. Heat treatments that reduce fouling should be performed gradually to drive away marine life - otherwise the local fish would experience a thermal shock and some would die. Limiting the seawater temperature increase, taking in colder water from deep, offshore locations, and utilizing diffusers at the outlet to recombine the seawater and reach thermal equilibrium quicker are all steps that help preserve the local environment.

7.12 Piping

There are three locations that helium piping will need to be installed:

1. from the core heat exchanger to heat storage (5 m),
2. from heat storage to the biofuels heat exchanger (5 m),
3. and from the biofuels heat exchanger back to the core heat exchanger (30 m).

The temperature of the working fluid (helium) as it is exiting the heat exchanger with the secondary loop will be at 606°C. The average high and low temperatures for Southern Texas are 27°C and 17°C, respectively [41]. This high discrepancy in temperatures requires two layers of insulation. Gaseous helium flow also requires a flow liner to reduce friction. Due to the high pressure of this system (5 MPa), there needs to be a pressure boundary pipe in place as well. The layout for the pipe is shown in Figure 36.

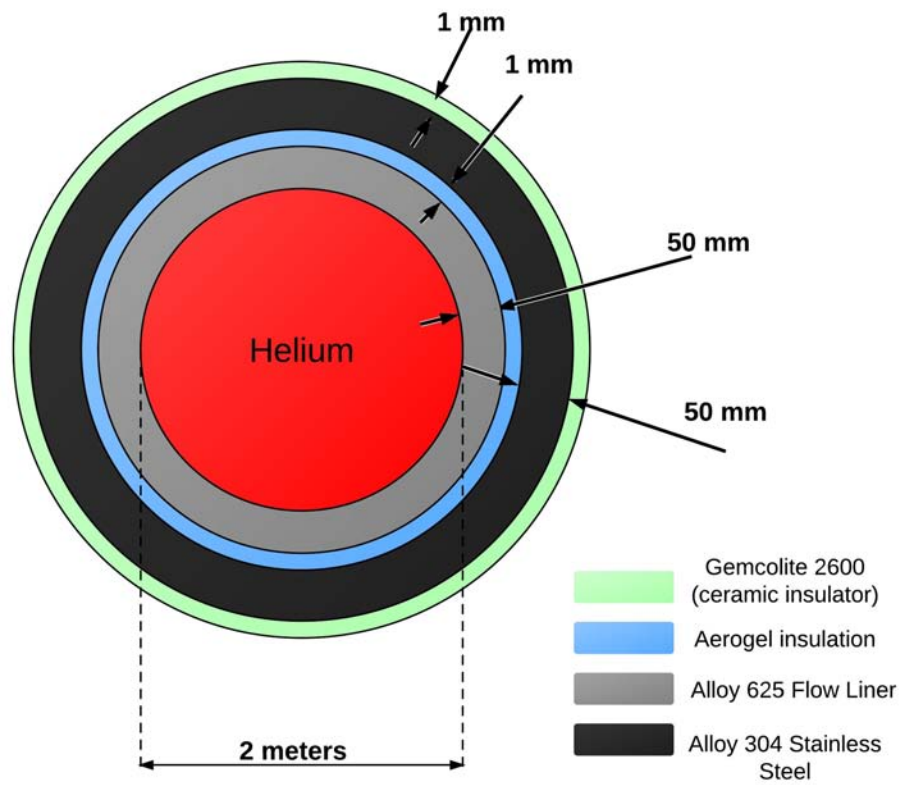


Figure 36: Helium Pipe Layout. Adapted from [87]

Length of Pipe (m)	Temperature Drop ($^{\circ}\text{C}$)	Pressure Drop (Pa)
5	0.007 (negligible)	56.87
30	0.041 (negligible)	2047.28

Table 17: Losses through helium transport pipes

The helium gas flows in the inner circle with a mass flow rate of 149.85 kg/s. The next layer is an Alloy 625 [71] flow liner of a thickness of 50 mm. The next layer is an aerogel layer [106] 1 mm thick. Following the aerogel layer is a 50 mm thick Alloy 304 stainless steel layer [47]. The outer layer that interacts with atmospheric conditions is a ceramic insulator from RSI called Gemcolite 2600 [75] of thickness 1mm.

The applied hoop stress on this 50 mm thick Alloy 625 is approximately 81 MPa [152]. The design limit for Haynes manufactured Alloy 625 is around 350 MPa [71] so this is well below design limits and a safe thickness to use.

Using accepted equations for temperature and pressure losses, known properties about each of the materials, and calculated parameters in the process heat system, the losses in Table 17 were found.

7.13 Process Heat System Costs

7.13.1 PCHE

The cost of a PCHE is proportional to the metal fraction f_m . The metal fraction for PCHE1 and PCHE2 was calculated using Equation 28 and was found to be 62.95% [54].

$$f_m = 1 - \frac{\pi d^2}{8Pt} \quad (28)$$

Following the calculation of f_m , a methodology similar to Dostal's [54] was used to estimate the capital cost of the PCHEs. These capital costs are outlined in Table 18. The cost of Alloy 617 was not available at the time of this calculation and a \$30/kg value of steel as quoted by Heatric [54] was used for this cost estimation. Alloy 617 costs have been requested from Huntington Metals and these cost calculations will be updated when the Alloy 617 costs become available.

HX	Material	Volume (m^3)	Weight (kg)	Cost (K\$)
PCHE1	Alloy 617	8.2548	69,010.128	2,070.30384
PCHE2	Alloy 617	15.6	130416	3,912.48

Table 18: PCHE capital cost

7.13.2 Circulator

The circulator will have to be custom built so the exact price is not known, but currently manufactured circulators that accomplish similar goals cost around \$250,000.

7.13.3 Piping

The cost per meter of the entire piping apparatus (from Alloy 625 all the way out to the Gemcolite 2600) is approximately \$36,507. Therefore, the total cost for 40 m of piping (the total amount that will be in the system) is around \$1.46 M.

8 Hydrogen

8.1 Introduction

After evaluating multiple methods of hydrogen production discussed earlier, the two best options for this hydrogen production facility were determined to be the the UT-3 production process and high temperature steam electrolysis (HTSE). The UT-3 hydrogen production process is attractive because it has been proven commercially for large-scale production of hydrogen [32] and had manageable material concerns compared with other thermo-chemical water splitting methods such as the sulfur-iodine process [157]. The other leading approach, HTSE, is attractive due to the simplicity of the process relative to the UT-3 method: an electric potential is maintained to separate steam into its constituents, hydrogen and oxygen. Also, HTSE does not produce environmentally harmful byproducts and thus satisfies one of the primary initiatives to minimize greenhouse gas emissions from this facility. However, the primary motivation for the decision to utilize the UT-3 process was that HTSE had not been demonstrated on the scale of hydrogen production required for the biofuel production plant, 7.9 kg s^{-1} , and scalings of steady-state electrical power requirements for a large scale HTSE hydrogen production plant were not definitive. A description of the UT-3 hydrogen production plant design and the reasoning for the eventual abandonment of this approach in favor of the HTSE process is provided in Appendix E.

However, since the UT-3 process inherently requires substantial surplus steam, or another high heat capacity fluid, to carry reactants and products throughout the cycle, the amount of electrical power required to heat the reacting and excess steam from temperature available, 560 C, to 760 C was ultimately impractical relative to the electrical output of the lead-bismuth reactor implemented in this design; substantial additional electrical power would have to be imported to this UT-3 hydrogen production plant. Therefore, HTSE was reconsidered as a viable option. Though the temperature of steam required for efficient steam electrolysis is also upwards of 800 C, the efficiency of separating steam at that temperature along with no longer requiring excess steam as a working fluid of a system proves the electrical requirements of this type of hydrogen production plant to be more practical than a UT-3 plant. In an effort to further reduce electrical power requirements in this HTSE plant, a design using regenerative heating is proposed to minimize the electrical power requirements required to raise steam from 560 C to 800 C. Ultimately, utilizing stacked solid oxide electrolyzer cells, an energy efficient HTSE plant has been implemented in this design to supply the biofuel production plant with the necessary hydrogen input rate of 7.9 kg s^{-1} .

8.2 High Temperature Steam Electrolysis (HTSE)

8.2.1 HTSE Production Plant

Mass Flows and Thermal Energy Calculations A high temperature steam electrolysis system has been designed with recuperative heating in an effort to minimize the steady-state electrical requirements for a hydrogen production rate of 7.9 kg s^{-1} required by the biofuel production plant. The design, along with mass flows and power requirements is presented in Figure 37.

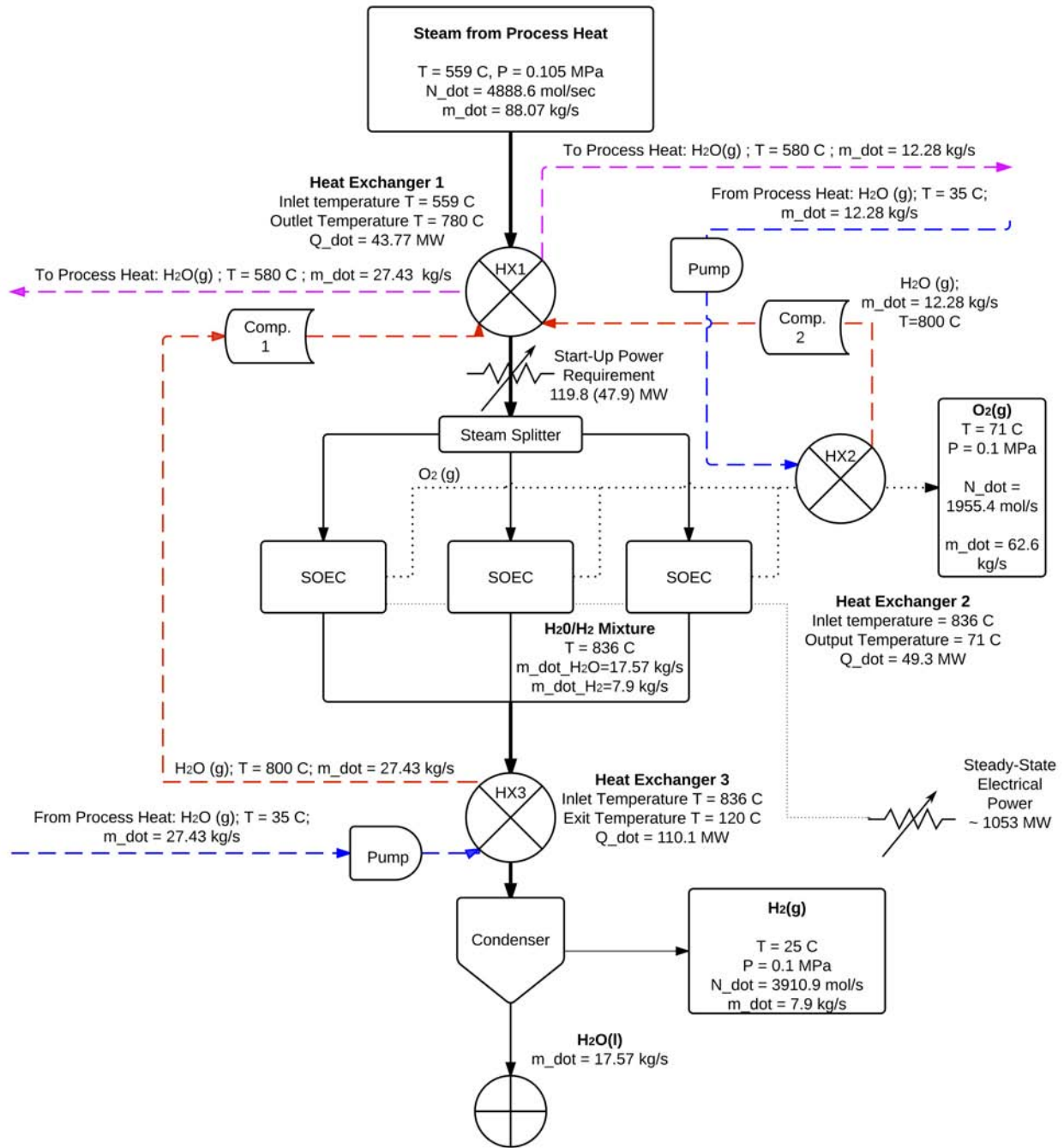


Figure 37: HTSE Hydrogen Production Plant

Steam is provided by process heat system at a temperature of 559 C and pressure 0.105 MPa, with a mass flow of 88.07 kg s⁻¹. The temperature of the steam from process heat is limited by the output temperature of the lead-bismuth reactor; however, a temperature of 800 C is required for high temperature electrolysis to be an efficient means of hydrogen production [59]. Thus, the mass flow of steam coming from the process heat system must be heated to 800 C before entering the water splitting solid oxide electrolyzer cells (SOEC) to achieve necessary steam conversion efficiencies.

Using simple energy considerations, the power required to raise this mass flow of steam to 800 C is found using

$$\dot{Q} = \dot{m}(h_{H_2O,800C} - h_{H_2O,559C}) = 47.9MW$$

Thus, initially before the recuperative heating system is in operation, the steam will be raised to 800 C through electric heating. Assuming a 40% efficiency of electric heaters, the initial electrical requirement for heating 88.07 kg s⁻¹ of steam from 559 C to 800 C was found to be 119.8 MW. This required electrical power is the desired power to offset through recuperative heating process that will be discussed.

Steam at 800 C enters a steam splitter, which will partition the 88.07 kg s⁻¹ mass flow into a parallel structure of SOECs, which has been depicted in the flow chart as three parallel SOEC units. However, the number of solid electrolyzer units in parallel will be much larger, and the precise value will need to be determined in future study. Assuming a steam conversion of 80% in the SOECs, which seems reasonable from other mathematical models of the SOEC process, [77] the mass flows of the exiting $H_2O(g)/H_2(g)$ mixture and $O_2(g)$, which are passively separated in the SOECs, are found stoichiometrically using the known water electrolysis process, is presented in Table 19.

Material	Mass Flow (kgs ⁻¹)
$H_2O(g)$	17.57
$H_2(g)$	7.9
$O_2(g)$	62.6
<i>Total</i>	88.07

Table 19: SOEC Outlet Mass Flows

The temperatures of the output steams are increased by 36 C due to the operation of the SOECs at areal current densities of 7000 A m⁻². This relatively large current density leads to a documented increase in temperature during the electrolysis process [77] which enables the possibility of recuperative heating since the output stream temperatures are higher than the required input steam temperature of 800 C. Thus, during startup, this plant will rely solely on electric heating to raise the temperature of steam from 559 C to 800 C, but once recuperative heating begins, the electrical requirement can be greatly offset using reclaimed thermal power from the output streams of the plant. The separate exit streams of $H_2O(g)/H_2(g)$ and $O_2(g)$ are passed through two heat exchangers with secondary loops of water and steam in order to cool the exit products before sending the streams to the biofuel production plant, thus reclaiming the energy that would be lost from the system otherwise. Heat exchanger system 3 reduces the temperature of the $H_2O(g)/H_2(g)$ from 836 C to 120 C to avoid substantially different flow rates between gaseous hydrogen and liquid water, and 836 C to 71 C for $O_2(g)$ for and the resulting power extracted by heat exchangers (2) and (3) are present in 37.

Thus, the amount of power removed from the exiting streams of products is 159.4 MW. Two secondary systems using a two phase liquid-to-steam heat removal cycle are implemented to claim this recoverable power. Water from external sources enters the heat exchanger systems (2) and (3) at 35 C, and is heated through a series of heat exchangers to 800 C. Though it would be desirable to heat the exiting secondary steam flow to 836 C, the practical exit temperature is limited to 800 C by finite heat exchangers. Even though the total recoverable power is greater than the required thermal power to raise the incoming stream of steam at 559 C to 800 C, due to temperature constraints between 800 C and 580 C for the secondary system in heat exchanger 1, only 19.78 MW out of the 43.77 MW required thermal power to raise steam from 559 C to 780 C thermal power can be transferred from the secondary streams to the input stream, raising the temperature to 661 C. The remaining power required to raise the temperature of input steam from 661

C to 800 C is supplied through constant electrical power, while once again assuming 40% efficiency, would be 70.24 MW. Thus, overall, the recuperative heating cycles reduce the electrical power requirement for this plant by 49.6 MW while still assuming a 40% electrical heater efficiency.

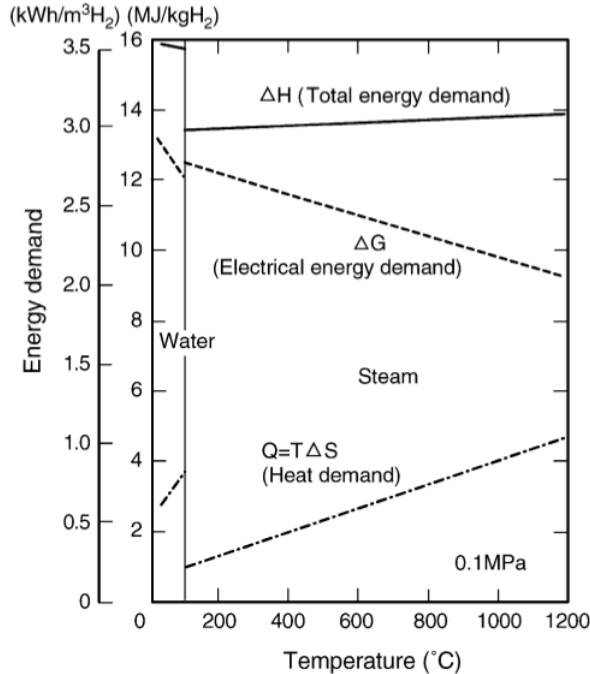
Through the recuperative heat process, heat exchanger system 1 transfer 19.78 MW from the recuperative heating loops to the inlet stream of steam, raising the temperature of the steam flowing at 88.07 kg/s from 559 C to 661 C. However, there is a total of 159.4 MW available from the recuperative heating system, thus, there is a surplus of power in the secondary streams exiting heat exchanger system 1 at 580 C of 139.6 MW. The recuperative heating output steam, which correspond to mass flow of 39.66 kg s⁻¹ at 580 C, are sent to process heat for their utilization to power the biofuel plant. Once the excess energy is extracted from the secondary steam by the process heat system, the now liquid water at 35 C is returned to the hydrogen production plant and cycles, forming closed secondary recuperative heating loops. Thus, not only is recuperative heating offsetting our electrical requirement for the hydrogen production plant by 49.6 MW, it is also powering the biofuels production plant.

Lastly, the cooled $H_2O(l)/H_2(g)$ that exits heat exchanger 3 at 120 C is cooled further in the condenser to acceptable room temperature conditions for leftover water rejection at the end of the cycle. The two-phase mixture is separated naturally and the 7.9 kg s⁻¹ of $H_2(g)$ is piped to the biofuel production plant. The oxygen output is not needed for any purpose in the biofuel production plant, and it could either be sold or vented appropriately to the atmosphere. Possible uses of this oxygen, along with the abandoned idea of hydrogen storage that was not longer deemed required for this design, is presented in Appendix F.

SOEC Electrical Power Requirements An estimation for the SOEC power requirement can be found using the following formula used in previous studies which relate the molar hydrogen production rate to the total current in the entire SOEC system [63],

$$\dot{N}_{H_2} = \frac{I}{2F}$$

where F is the Faraday number ($96487JV^{-1}mol^{-1}$). The total molar production rate of hydrogen is 3910.9 mol s⁻¹, and thus corresponds to a current of $I = 754.7$ MA. The electrolyzer cells would seem to operate at roughly 0.54 V compared the the approximately 1 V [26] required for water electrolysis using ratios of the electrical energy requirements depicted in Figure 38. The dotted line depicting the electrical energy demand is a characterization of the magnitude of the electric potential required to split water molecules into hydrogen and oxygen. At the phase transition from liquid to gas, and as steam temperature increases, the amount of electrical power required to split water molecules becomes increasingly smaller. Using steam at 800 C, an approximate electrical power requirement of 402.68 MW is required. Due to the uncertainty in the actual efficiency of these cells relative to the ideal power requirements depicted in Figure 38, further analysis will be required to present a more definitive electrical power requirement for the SOECs. Nevertheless, this calculation of electrical power requirements will be used as a lower bound of the electrical power requirements for this hydrogen production plant. Some studies suggest an electrical power requirement of 3.1 kWh per normal m³ of hydrogen produced in similar planar stacks of SOECs, which would require an electrical power requirement of 983.1 MW for water splitting, coupled with the steady-state power requirements to raise input steam from 661 C to 800C, would lead to a total electrical power requirement for the hydrogen production plant of 1053.3 MW [77]. Though this electrical power requirement is relatively large compared to the theoretical values, this figure is still reasonable on the scale of electricity production of this reactor system. This electrical power requirement will be used a conservative upper bound on the electrical power requirements of this hydrogen production plant that has been demonstrated experimentally. Thus, HTSE appears to be favorable approach to large-scale hydrogen production, and future work involving more sophisticated simulations of HTSE hydrogen production and subsequent optimization will more definitively determine the electrical power requirements for this hydrogen production plant. In addition, it is important to note the hydrogen production plant will be powering the biofuel production plant with the surplus heat removed from outlet streams of residual steam, hydrogen, and oxygen, and thus will offset some of the electrical power requirements that would be required in the biofuel production plant without the recuperative heating system.



Courtesy of Elsevier, Inc., <http://www.sciencedirect.com>. Used with permission.

Figure 38: Power Requirement for Water Electrolysis [121]

8.2.2 Materials and Components

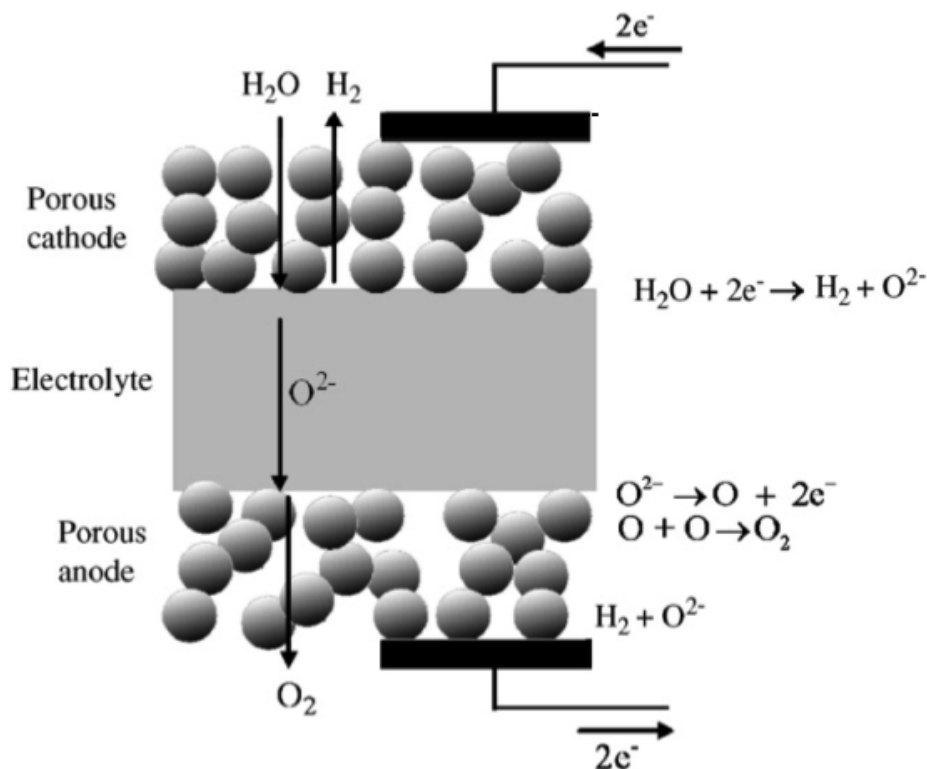
SOEC The fundamental principle behind high temperature steam electrolysis (HTSE) is that as the temperature of the steam increases, the energy required to dissociate the H_2O molecule decreases. Like standard water electrolysis, HTSE can produce large quantities of emissions-free hydrogen while also eliminating the need for expensive chemical catalysts [161]. To split the H_2O molecule, a Solid Oxide Electrolysis Cell (SOEC) is used to apply an electrical potential substantial enough to dissociate O_2 and H_2 .

39 is a schematic of an SOEC cell. The cell unit consists of three distinct sections: a porous, conductive cathode, an oxygen-ion-conducting electrolyte, and a porous, conductive anode. As shown, H_2O is incident on the cathode and undergoes the chemical reaction: $H_2O + 2e^- \rightarrow H_2 + O^{2-}$. The H_2 remains at the cathode while the applied electrochemical potential draws the oxygen through the electrolyte towards the anode. In doing so, the e^- are liberated from the ions allowing the formation of molecular O_2 at the anode. This molecule travels through the porous material and is collected in a stream at the outlet of the cell [7]. The rate of hydrogen production directly corresponds to the temperature of the gaseous H_2O entering the unity as well as current applied to the cathode/anode [161].

SOEC were initially developed in a tubular formation, chosen as the optimal configuration to avoid sealing problems [77]. The SOEC tubes would be repeated to achieve greater hydrogen production resulting in 10-cell and 24-cell configurations [63, 121]. It was found through experimenting that the tube formations required a longer current path, increasing the Ohmic resistance within the cell. The planar formation of SOECs both shortens the current path as well as permits a high packing density, making it the more efficient choice [77]. SOEC units now consists of “stacks” of cells, connected by conductive interconnects and have been operated successfully up to 60 layers [63].

Before exploring the materials used in the SOEC, it is important to identify requirements necessary for efficient H_2 and O_2 separation:

1. The electrolyte must be
 - (a) dense
 - (b) chemically stable



Courtesy of Elsevier, Inc., <http://www.sciencedirect.com>. Used with permission.

Figure 39: SOEC schematic [105]

- (c) have high ionic conductivity (and therefore, high current efficiency, resulting in a high conversion efficiency for the cell)
 - (d) gas-tight, such that recombination of H_2 and O_2 will not occur
 - (e) thin, to minimize the effects of Ohmic resistance
2. Electrodes should have suitable porosity to support gas transportation.
 3. Thermal expansion coefficients should be similar for the electrodes and the electrolyte to minimize mechanical stress within the cell.
 4. Interconnect material must be chemically stable in reducing/oxidizing environments.

Electrolyte Material Yttria-stabilized zirconia (YSZ) is the most common electrolyte material used in SOEC cells. ZrO_2 boasts high oxygen ionic conductivity, good mechanical strength, and a high melting point (~ 2937 K). A necessary dopant (Y_2O_3) is added to provide stabilization for the lattice structure, consequently lowering ionic conductivity. Table 20 summarizes the other options for electrolyte materials. Though not having the highest ionic conductivity, YSZ was deemed to be the best choice overall for mass production of electrolysis cells on the basis of cost and chemical compatibility in reducing environments. [105].

Cathode Material To achieve the chemical and physical stability required of the cathode in a highly oxidizing/reducing environment, the two viable options for SOEC cathodes are noble metals (e.g. Pt) and non-precious metals (e.g. Ni and Co). While both options perform similarly, the high cost of noble metals makes non-precious metal electrodes the more appealing option. Specifically, Ni is selected due to its high electrochemical reactivity as well as its ability to induce hydrogen reduction. The material is combined with the YSZ to form a cement like material used as the cathode [7].

Name	Type	Conductivity (S/cm)	Optimal Temperature (K)	Comments
YSZ	Stabilized zirconia	0.13	1273	Overall best choice
ScSZ	Stabilized zirconia	0.18	1273	Due to intricate production procedure, the cost of ScSZ is exorbitant
LSGM	Doped LaGaO ₃	0.17	973	Requires reduced operating temperature; problematic reaction between LSGM and Ni
GDC	Ceria-based oxides	0.10	1073	Chemically unstable in a reducing environment
SDC	Ceria-based oxide	0.08	1073	Chemically unstable in a reducing environment
BaCeO ₃	Proton-conducting electrolyte	0.08	1073	Low conductivity

Table 20: Summary of options for solid electrolyte materials

Anode Material Like the cathode, only two classes of materials successfully function for use as the SOEC anode: noble metals (less attractive due to cost) and electronically conducting mixed oxides. Lanthanum strontium manganate (LSM) exhibits a similar thermal expansion coefficient to the YSZ electrode and sustains a high potential drop across the SOEC. To date, no other materials are explored for application in the SOEC cell [105].

8.2.3 Material Corrosion

Over time in any construct materials begin to degrade. In the HTSE hydrogen production plant the two main concerns are corrosion of the piping and degradation of the electrolyzer cells. Utilization of corrosion resistant ceramics that can withstand 800 C temperatures could mitigate these concerns and increase the longevity of this plant. Future work will require investigating possible ceramics for this purpose.

Metallic Piping Corrosion At high temperatures many materials exhibit unfortunate processes which lead to structural failures. The high temperature steam necessary for the electrolyzers to run, will inevitably take its toll on any piping and turbines used to transport it. Material expansion, creep, and oxidation are all problems that must be addressed in the design [114]. For these reasons, there is considerable interest in nickel based superalloys which are more resistant to these concerns. In such materials, a protective layer of chromium oxide forms preventing direct contact between the metal and the high temperature oxidizing environment. It has been shown that the Ni-based superalloy Haynes 230 has superior oxidation resistance when compared to other superalloys [42]. This material could be used in the piping and heat exchangers of the plant.

Electrolyzer Corrosion Despite extensive research into longer-lived fuel cells, there is still much work to be done. Problems such as contact between different materials, deterioration of the electrodes, and blocking of reaction sites are all ongoing concerns to the lifetime of the electrolyzer cells. Future research is required to optimize electrolyzer cells to operate as well as possible for extended periods of time, both to ensure proper production rates during scheduled operation, but also to minimize replacement costs that will negatively effect the long-term economics of this reactor system. Current problems to mitigate are as follows. The changes in temperature caused by heating up the electrolyzer will stress the materials as they expand at different rates. Thermal cycles must be reduced as much as possible to minimize thermal stresses that will degrade the performance and structural integrity of these cells. Furthermore, chromium from the interconnects can poison the electrodes reducing the electrical conductivity, and thus research into ceramic coatings can be used to slow this process. The delamination of the electrode-electrolyte interface in the oxygen electrode is another major problem that must be addressed through additional materials research. Silicon poisoning on the electrode coming from the seal of the cells themselves or the steam can also interfere

with conductivity. For this reason demineralized water should be used for the steam and different coatings should be considered in future work [60].

Economics Using estimates from Idaho National Laboratory, the total capital cost would be on the order of 1.3 billion dollars. Given an expected lifetime of the electrolyzer cells of 3 years, the yearly replacement cost for a third of the cells is estimated at around 40 million dollars annually [8].

8.3 Other Design Considerations

8.3.1 Biofuels shutdown

If the biofuels plant shut down unexpectedly, there would be a large amount of hydrogen that would need to be dealt with safely. First, a valve in the first pipe which brings steam from the process heat section into the hydrogen plant would close, so that no more hydrogen would be produced. Second, there would be an emergency system to cycle the hydrogen gas and steam back through the plant. The voltage would be turned off so that the steam would remain steam and not be split into more hydrogen. Small amounts of hydrogen gas would slowly be bled off from the main stream and flared in safe amounts.

8.3.2 Core shutdown

If the reactor shut down unexpectedly, the HTSE plant would lose electricity and the temperature of the steam would decrease. Without electricity, there would be no voltage and electrolysis would not occur. The plant would stop producing hydrogen, but there would be no major safety concerns in the event of an unexpected core shutdown.

8.3.3 Mechanical failures

There will be a redundant compressor to ensure that if a main compressor fails, the hydrogen production facility can continue with routine operations. However, since the compressor condenses steam into water, failure of both compressors would not cause catastrophic failure in any case.

8.4 Conclusions

The HTSE hydrogen production method was ultimately chosen for this design to supply the required 7.9 kg s^{-1} of hydrogen for the biofuel production plant. Steam at 559 C enters the hydrogen production plant from the process heat system and must be heated to 800 C to achieve acceptable steam electrolysis efficiencies. The inlet steam temperature is increased to 800 C using both a recuperative heating system and electrical heating. The oxygen, hydrogen, and unseparated steam products are cooled after increasing to 836 C in the electrolyzer cell system, providing 159.4 MW of total recoverable power. Only 19.78 MW is able to be transferred to the inlet steam due to differential temperature limitations, raising the input steam temperature from 559 C to 661 C, while the remaining 139.6 MW is reclaimed by the process heat system to power the biofuel production plant. The recuperative heating system that would reduce the steady-state electrical power requirements by a significant 49.6 MW and also provides excess heat to power the biofuel production plant. Thus, the recuperative heating system is advantageous for overall energy efficiency of this nuclear reactor system by recovering the thermal power available in the output streams of this hydrogen production plant. The steady-state electrical power requirement to raise the inlet steam from 661 C to 800 C is 70.24 MW. Steady-state electrical power requirements both to heat inlet steam from 661 C to 800 C and to maintain the electric potential in the electrolyzer cells are conservatively estimated at 1053.3 MW, and will likely be able to be reduced with more sophisticated simulations of this hydrogen production plant design and subsequent optimization in future work. It is also important to note that any increase in the available process heat temperature above 559 C will lead to a reduction in electrical power requirements of this design as well, and thus higher reactor output temperatures would be advantageous for more energy efficient HTSE hydrogen production designs.

9 Biofuels

9.1 Process Overview

Various biofuels production designs were considered, with parameters of greatest importance being the biomass cost, availability, and competition with food sources; the carbon emissions, technical feasibility, and capital cost; and the quality, quantity, and commercial viability of the fuel produced. A Fischer-Tropsch (FT) manufacturing plant and refinery using switchgrass feedstock was chosen as the most favorable way to produce synthetic gasoline and diesel. A thermochemical route to FT fuels was selected which uses gasification and gas-clean-up to form a producer gas, or syngas, that is fed into the FT reactor. This approach utilizes the available hydrogen and steam resources, minimizes capital cost and maintenance requirements, and results in a distribution of hydrocarbons that can be refined into gasoline and diesel blends. If implemented on a large scale, the estimated production costs for high energy density FT fuel could be as low as \$1/gallon [39], which also makes it economically competitive. FT fuels are already being produced from biomass by companies such as Rentech and Choren [39], giving them a high feasibility, and the waste emissions of the process - charred ash from the gasifier, trace acid gases such as H_2S , and some CO_2 removal [90] - are low overall.

The proposed biofuels production plant is shown in Figure 40. As seen in the figure, the main sections of the plant include a biomass preparation area, a Silvagas[®] gasifier and tar removal unit, a Rectisol acid gas removal system, a bubble column Fischer-Tropsch reactor, a fractional distillation unit, a Sasol refining unit, and biogasoline and biodiesel storage sites. The majority of the biofuel plant energy will be supplied by excess process heat from the nuclear reactor. Hydrogen for the FT and refining processes will be supplied from the hydrogen production plant, and minor electricity costs will be covered using electricity from the nuclear reactor.

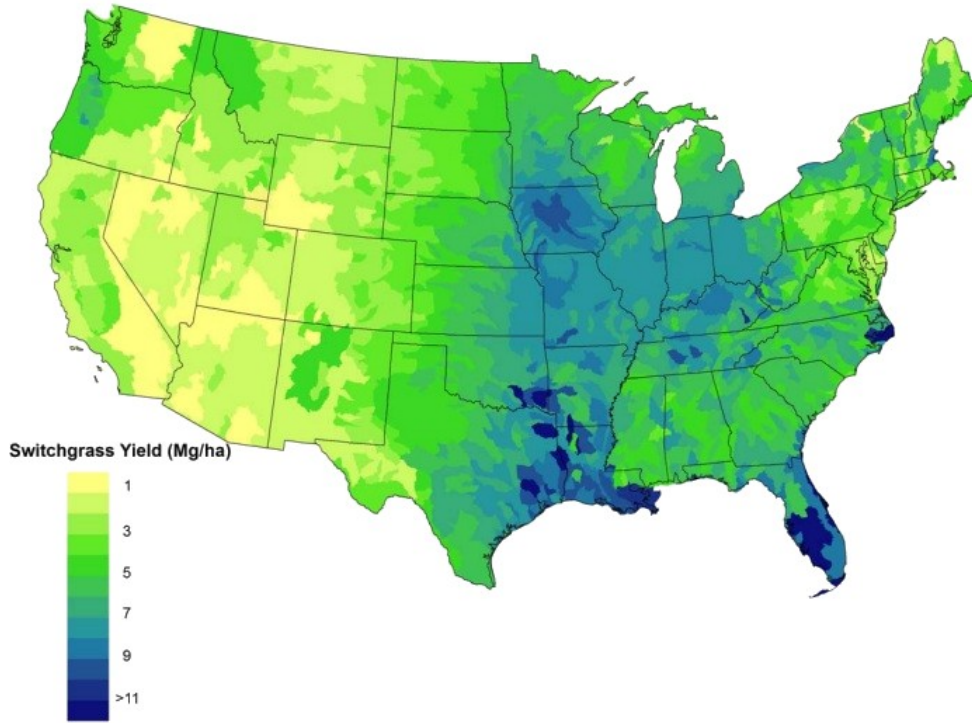
A feedstock flow rate was chosen based on the amount of available switchgrass, process heat, and hydrogen resources. An estimated one million dry metric tons of switchgrass can be grown for a power plant in one year, which has led to designs in the literature that use 3,500 tons/day (tpd) of biomass, so switchgrass availability was not the limiting factor in our plant design. The current biofuels plant design uses 2,903 tpd or 24.38 kg/s of switchgrass.

For power, electricity will be drawn from the nuclear power plant for basic facility needs, while 40 MW of heat energy will be sent from the nuclear reactor to the biofuels plant in the form of H_2O . This energy will be used primarily to warm the air and steam inputs into the Silvagas[®] gasifier, to power the FT reactor, and to heat FT liquids during distillation. The biofuels plant will also supply 19 MW of heat back to the process heat system by cooling the syngas immediately prior to acid-gas removal.

The hydrogen plant will supply H_2 to the refining procedure, which needs 7.9 kg/s for naphtha hydrotreatment, distillate hydrotreatment, wax hydrotreatment, and C_6/C_5 isomerization [53, 51, 93]. All refining will be conducted on-site to meet the targets of the overall design of the complex. The biofuels plant expects to operate at 20 hours a day and will give prior notice whenever possible before shutdowns, since hydrogen production must stop or vent their gas whenever biofuels production pauses. The biofuels plant will further ensure that proper heat dumps are managed whenever production stops and will coordinate with reactor shutdowns to ascertain that the necessary process heat is always available.

9.2 Switchgrass

Switchgrass (*panicum virgatum*) was selected as the optimal bioenergy crop because of its very high energy density, ability to grow in dry climates, reproducibility on poor land, and exclusion from use as a food crop [96, 92, 147]. The places where switchgrass can grow are mapped in Figure 41. Among other alternatives for biomass feedstock, it has a more water-efficient C_4 Carbon Fixation cycle and higher energy density of lignocellulose. Up to one million dry metric tonnes of switchgrass could be grown for a power plant in one year [90], so the amount of biomass needed is limited by other factors such as the amount of heat available for gasification and hydrogen available for refining. It was calculated that an input of 24.38 dry kg/s of feedstock at 20% moisture would be required to fuel the current plant design.



Map courtesy of Pacific Northwest National Laboratory, operated by Battelle for the U.S. Department of Energy.

Figure 41: Sites for switchgrass growth in the U.S.

9.2.1 Densification

Switchgrass production and preparation will be outsourced to farmers and their facilities to take advantage of an extant external network, to remove the logistical burden of maintaining on-site facilities, and to improve the transportation condition of the biomass itself.

First, unprocessed switchgrass bales have a bulk density of around 150 kg/m^3 [128] and are not economical to transport. Fortunately, the microscopic structure of switchgrass (SG) is porous. When large amounts of pressure are applied to small surface areas of biomass, the particles become compressed and fill in these spaces, and then further interact with intermolecular bonding. The moisture serves as a binding agent for the lignin and cellulose, activating the bonding mechanisms of the macromolecules at high pressure. Friction causes heating up to 90°C , which allows the bonds to consolidate upon cooling [81]. The molecular bonding and the secondary structure resulting from that bonding during the application of force maintains the pellets in cohesive units such that loss of material due to disintegration is negligible. A pelletizer at 137 MPa with a screen size of 3.2 mm can produce pellets at 12% moisture with a density of 1000 kg/m^3 [128], which is an order of magnitude higher than the raw material. Immediately after harvesting, such a pelletizer will be employed before switchgrass is shipped to the plant. Bales taken directly from a switchgrass farm will need to be stored in a climate-controlled, dry location. When moisture content is achieved, they will then be hoisted by machine from the holding facility into a large hopper, which will feed directly into a grinder. This will allow for smoother pressing, as the grounded material will then proceed to the pneumatic pelletizer (see Figure 41). The pellets will be then be arranged into a transportable medium. In densified form, the bulk feedstock takes up less volume and allows for trucks to consistently haul more biomass per trip. With fewer trips, the CO_2 emissions during transportation are reduced, and thus the amount of greenhouse gases produced in our process that are also lowered. Accounting for 20% moisture, it was calculated that 30.48 kg/s of pellets were needed as an input, which account for 24.38 kg/s (2903 tpd) of useable biomass.

9.2.2 Transportation to Site

The capital costs of transportation are generally \$0.028/ton/km for rail and \$0.137/ton/km for trucks, with the latter having a greater rate of change per distance traveled but a low initial fixed cost [84]. The plant should be located in a growing region such as Minnesota or Texas (See map in Figure 41) [101] so that shipping of feedstock by truck will be under 200 km and meet optimal pricing. Although there would be a clearer advantage to railway for both long-distance transport and insertion of materials into an continuous process, it poses negative implications for the plant's reaction time to reactor shutdown periods. Land vehicles can be dispatched most efficiently in the event of feedstock shortage and can be readily halted if necessary. They also do not require large changes to existing infrastructure [162].

The input process will rely on an unloading mechanism and a temporary storage system, which cannot be fully automatic and will require some degree of manual labor. The unloading dock will need to consist of several bays and have direct access to an area of low traffic congestion. Pellets from the temporary storage area will be fed to a conveyor belt that leads to a weighing hopper, which will then feed directly into the gasification chamber in fixed amounts for particular durations of the process (see Figure 41).

Considering that gasification proceeds at a temperature of 682°C, there must be considerable distance between the gasification chamber and the holding area, and the conveyors and hoists will need to consist of fireproof material. In the event of a reactor shutdown, the holding area will need direct access to short-term storage. The engineers will need to schedule the reshipment of feedstock with the refueling of the core such that downtime between start-up of the reactor and that of the biofuels facility will be very short. Furthermore, it is possible that shipments may fluctuate with the perennial growing cycle of switchgrass, such that it may be necessary to arrange for backup suppliers in case of emergency shortage. All possible locations of suppliers must be evaluated for typical weather conditions that may prove troublesome to providing a consistent source of feedstock. If this is a decisive factor, then the complex must take footing based on that locality.

Before the biofuels facility can operate, ground transportation must be established between the reactor complex and the energy crop source such that feedstock can be delivered in a controlled and consistent manner. Processing SG into a dense form allows for a more economical transportation option and a very controlled injection into gasification processes, which allows the overall process to be more streamlined and manageable. However, as opposed to the other sectors of the reactor complex, there are external variables that weigh into the availability of this biological resource, which will require considerable foresight and logistical coordination during operation.

9.3 Gasification

The switchgrass will be fed by lockhopper into Rentech's patented Silvagas dual fluidized bed gasifier [58], where the biomass will be converted to syngas. Silvagas was selected because of its commercial availability, its operation at atmospheric pressures, and the advantages of dual fluidized bed gasification: gasification and combustion occur in separate chambers as shown in 42, which prevents N₂ and CO₂ dilution of the syngas. In the combustion chamber, preheated air combusts with switchgrass char and raises the air temperature to 916°C. This heat is transferred to the gasification chamber via a fluidized sand bed with very little air transfer, and the leftover "flue gas" is vented or collected. In the gasification chamber, switchgrass gasifies in the presence of superheated steam and the hot sand bed, forming a syngas of primarily CO, H₂, and CO₂. Unreacted switchgrass and cooled sand is sent back to the combustion chamber, while useful syngas is sent on to gas cleanup and the FT reactor.

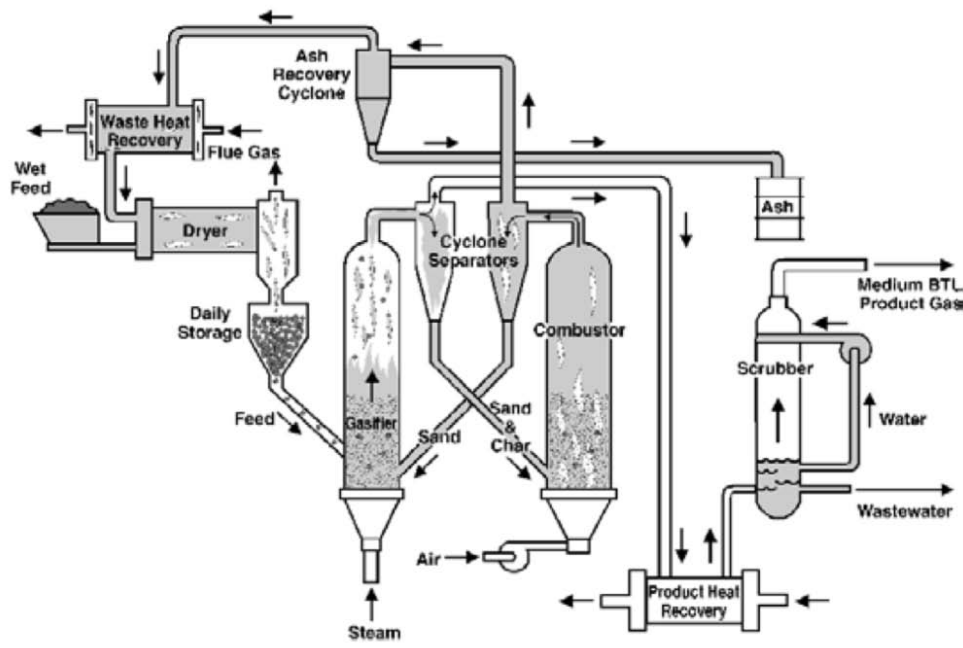
The gasification chamber employs switchgrass input of 24.38 kg/s (dry) and superheated steam input of 4.42 kg/s at 182°C, which react at the high temperature of 682°C supplied by the fluidized sand bed. The main reactions which occur here are the

Boudouard reaction,



water-gas or steam reaction,





© ASME. All rights reserved. This content is excluded from our Creative Commons license. For more information, see <http://ocw.mit.edu/fairuse>.

Figure 42: Schematic of silvagas gasification process

Biomass Type	Switchgrass	Wood
Carbon	49.4%	51.35%
Hydrogen	6.11%	6.10%
Oxygen	44%	42.29%
Sulfur	0.12%	0.09%
Nitrogen	0.64%	0.17%

Table 21: Mass distributions of wood and switchgrass [39]

methanation or hydrogasification reaction,



and gas-shift reaction,

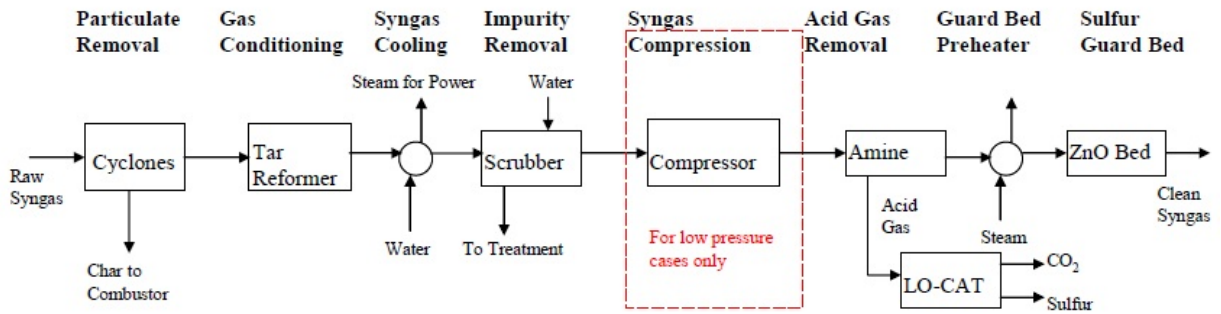


Other reactions are also present, but at slower rates and in smaller amounts. Since the total amount of minor compounds such as sulfur and nitrogen is less than 1% in switchgrass and steam, they do not play a significant role in the gasification reactions. The listed chemical reactions occur at varying rates and approach different equilibrium levels depending on the gasifier design. In the Silvagas process, the carbon conversion rate is about 73% [34], and all the carbon comes from the switchgrass biomass. The composition of syngas formed from wood chips in the Silvagas gasifier is known, and is comparable to the expected syngas composition after switchgrass gasification because of the similarity in composition of the two biomasses [39], as shown in Table 21. After gasification, syngas exits through the top of a cyclone to be purified and then sent to the FT reactor. The final syngas output will be at a temperature of 682°C and a rate of 33.2 kg/s [58].

About 27% of the carbon content does not react [34]. This particulate biomass, called char, is filtered out by the cyclone and sent back to the combustion chamber to be burned. Heated air at 4 kg/s and 354°C, as calculated from the specifications of the Silvagas patent, enters the combustion chamber and combusts with the switchgrass char to generate temperatures of 916°C, which supplies the energy for the gasifier [58].

Compound	% by Volume	Mass Flow Rate (kg/s)
CO	47	10.97
H ₂	18	0.303
CO ₂	14.3	5.25
CH ₄	14.9	1.99
C ₂ H ₄	4.7	1.10
C ₂ H ₆	1.1	0.276
other	< 1	~ 0
Total	100	19.89

Table 22: Composition of Syngas Output from Silvagas Gasifier [118]



© Nexant, Inc. All rights reserved. This content is excluded from our Creative Commons license. For more information, see <http://ocw.mit.edu/fairuse>.

Figure 43: Typical acid gas removal process after gasification of biomass without a combustion chamber

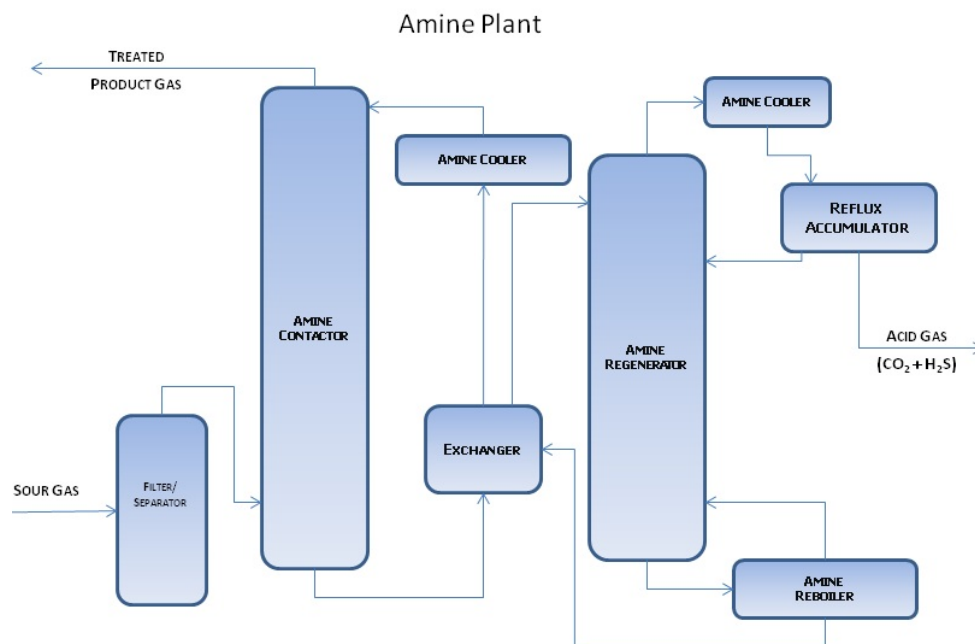
This heat is transferred to the gasification chamber via a fluidized sand bed with very little air transfer. Combustion heats the fluidized sand bed, after which the remaining "flue gas" exits the combustor and is collected for separate disposal.

The composition of syngas leaving the Silvagas reactor is compiled in Table 22 [118]. Other elements such as nitrogen, sulfur, and phosphorus are also present throughout the process in small amounts, but their volumetric flows are not calculated because they compose <1% of the final syngas. Unfortunately, the raw syngas can not yet be sent to the FT reactor because carbon dioxide, and to a lesser extent sulfur, nitrogen, and other trace elements, would poison the FT reaction.

9.4 Acid Gas Removal

Syngas cannot be sent directly to the FT reactor after Silvagas gasification because it contains various elements, such as carbon dioxide and sulfur, which could poison the FT process. In particular, CO₂ must be removed because it interacts with H₂ more quickly than CO does; the presence of CO₂ interactions would lower the energy output of the FT reactor and produce larger, unfavorable particles [115]. Trace elements such as sulfur and nitrogen, while too scarce to be noted in the literature, must also be removed to prevent long-term buildup and damage. A schematic of a typical acid gas removal process can be seen in Figure 43. The major steps are particulate removal, cooling and compression, and acid gas removal. Two steps from the schematic, tar reforming and ZnO bed sulfur removal, can be bypassed because the Silvagas process utilizes a combustion tower coupled to the gasification, which minimizes tar creation. Once the acid gases are removed down to acceptable levels, the syngas is sent to the F-T reactor following a heat addition and depressurization of the syngas to 15 bar at 245°C.

Syngas purification and conditioning begins with the separation of coarse particles in the Silvagas reactor. Initial purification is achieved using cyclones, which are large centrifuges used to separate solid particles from the syngas. These cyclones are used before the cooling of the syngas to prevent condensation and deposition [115]. The solid particles removed are primarily tars, hydrocarbons with C₁₀₊ that are recycled back to the combustor to further be broken down. The remaining raw syngas leaves the cyclones at 682°C, and gas cleanup continues with syngas cooling to 107°C and removal of unreformed tar using a water scrubber.



Courtesy of Plant Process Equipment, Inc. Used with permission.

Figure 44: Amine Acid Gas Removal Process

A mass flow rate of water is used from an outside source to lower the temperature of the syngas to 107°C over three stages. Syngas at 107°C and 1 bar is sent to the Syngas Venturi Scrubber, C-200. This is a patented process that uses moving water to remove ammonia, particulates, and halides from the syngas. The mass flow rate is adjusted to ensure that the syngas is quenched to the desired temperature of 107°C before it can be sent to the compressor [115]. Any remaining condensate in the syngas is removed using a patented machine, the Syngas Compressor KO Drum, V-300. The cooled syngas is compressed to 30.7 bar with a four stage horizontally split centrifugal compressor with interstage coolers at 43°C, which increases the solubility of acid gases, before being sent to the acid gas removal process [115].

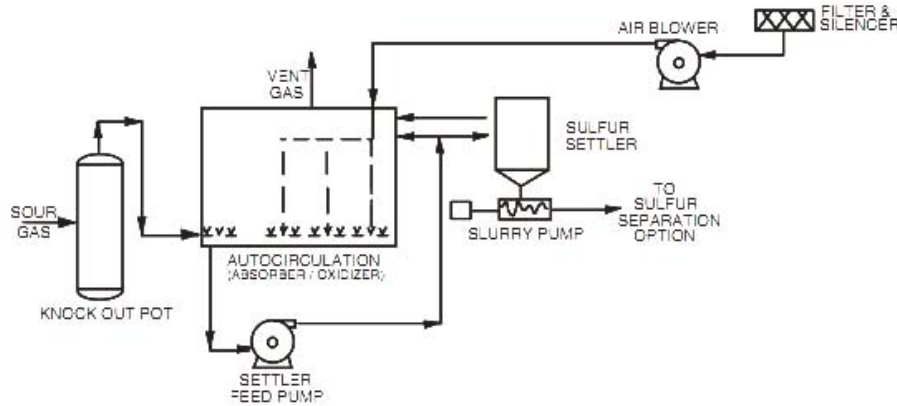
Lastly, two stages of acid gas cleanup removes poisonous molecules, primarily H₂S, NH₃, and CO₂, which can negatively affect the F-T reaction. The first stage, an amine removal plant, filters the H₂S concentration from ~400 ppm to ~10 ppm. Acceptable F-T conditions are 0.2 ppm, so a patented LO-CAT process is next employed to further reduce H₂S and CO₂ levels.

The amine acid gas removal process can be seen in Figure 44 [13]. An amine is an organic compound that includes nitrogen that dissolves with acid gases. The input is sour syngas, which refers to syngas that contains acid gases. The sour gas is first sent through a cyclone separator as precautionary measure, in case the particulate removal process did not remove all solid particles. Next, the syngas is sent to an amine contactor, diethanolamine (HN[CH₂CH₂OH]₂). This amine was chosen for the particularly low pressure acid gas removal process to minimize the overall net energy requirement and achieve the desired CO₂ and H₂S removal [115, 13]. In the amine contactor, acid gas composed of amine, CO₂, and H₂S separates from syngas and is sent to an amine regenerator, while the treated syngas is recycled through an amine cooler and sent back to the top of the amine contactor. The amine regenerator separates amine from CO₂ and H₂S, then reheats and recycles it back to the exchanger [13]. Carbon dioxide and sulfur are cooled in an amine cooler and expelled. CO₂ can be sequestered through a number of different processes and H₂S can either be vented or sent to a sulfur recovery plant to be sold commercially.

Diethanolamine-treated syngas at 107°C and 30.7 bar is sent to a patented LO-CAT process. This procedure, pictured in Figure 45, decreases the amount of H₂S in the “sour” syngas from a concentration of ~10 ppm to less than 0.2 ppm [46].

Again, the input to be cleaned is listed as a sour gas, even though it has just come from the amine removal plant, and again, a cyclone is used as a beginning filter. The syngas then enters a chamber containing oxygen flow and an iron catalyst. Acid gases from syngas are removed along with CO₂ and the products of H₂O

LO-CAT II Autocirculation Unit



Courtesy of Merichem Company. Used with permission.

Figure 45: LO-CAT acid gas removal process

Compound	Mass Flow (kg/s)
CO	10.97
H ₂	0.303
CO ₂	0
CH ₄	1.99
C ₂ H ₄	1.10
C ₂ H ₆	0.276
H ₂ S	< .2 ppm
Total	14.64

Table 23: Composition of Syngas Output after Acid Gas Removal

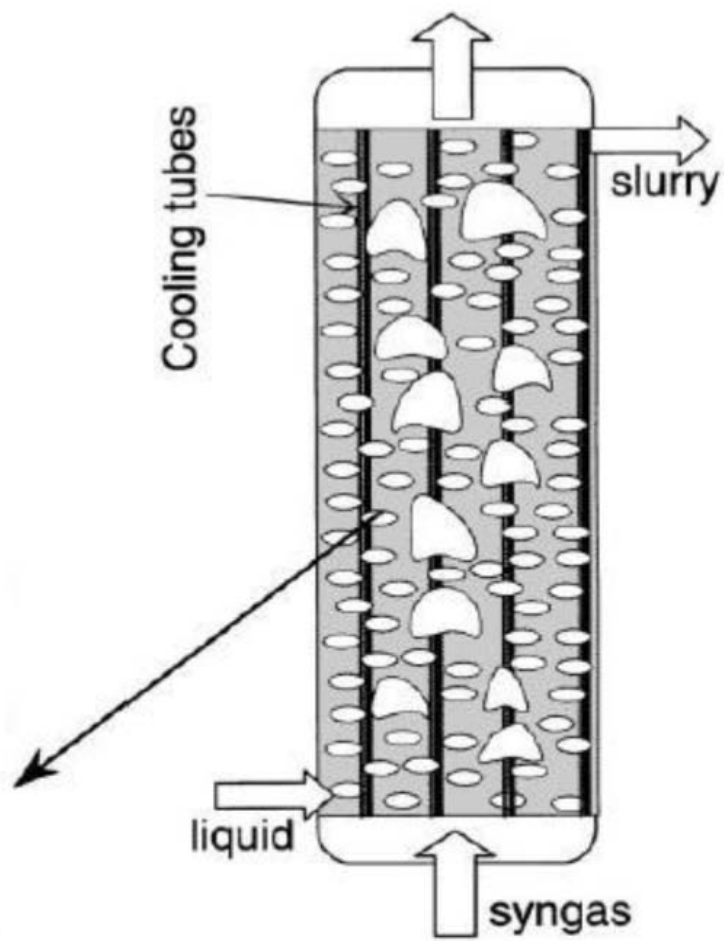
and S⁰(Fe) [46]. Sulfur is removed through the chemical reaction shown in Equation 33.



Finally, the syngas from the LO-CAT process needs to be depressurized down to 15 bar and heated to 245°C before it can enter the FT reactor. A depressurizer will be used to achieve the correct pressure conditions and the heat addition will come from the process heat group [115]. Clean syngas is sent on to the FT reactor at a mass flow of 14.64 kg/s and with the compositions shown in Table 23; there is virtually no loss of gases apart from CO₂ and sulfur removal.

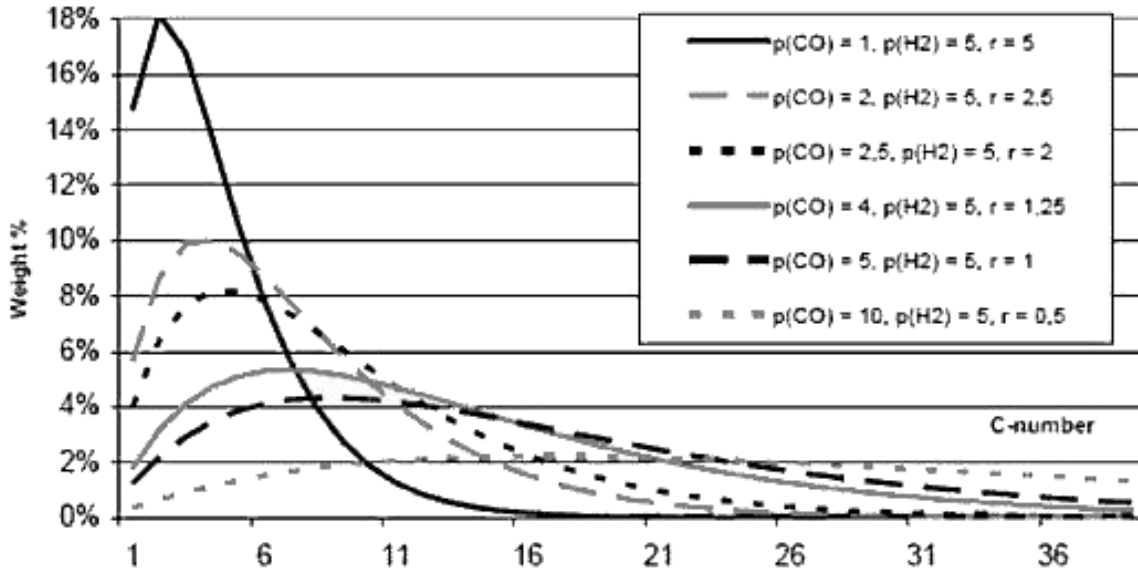
9.5 Fischer-Tropsch Reactor

The Fischer-Tropsch (FT) reactor is the heart of the biofuels production plant because it converts syngas into the long carbon chains of gasoline and diesel fuels. The reactor is filled with inert oil in which Fe catalyst particles are suspended. Processed syngas enters from the bottom of vessel through an inlet nozzle and is bubbled up vertically in a churn turbulent flow regime to maximize the mass and heat transfer [122]. As the syngas rises, the CO and H₂ gases form into longer hydrocarbons through the exothermic reactions listed below and the heat generated in these reactions is absorbed by vertical coolant tubes. A slurry phase bubble column FT reactor, pictured in Figure 46, has been chosen for its isothermal operating condition and good heat transfer [100]. The reactor is 7 m in diameter and 30 m in height and operates at a temperature of 240°C and pressure of 24.0 bar.



Courtesy of Elsevier, Inc., <http://www.sciencedirect.com>. Used with permission.

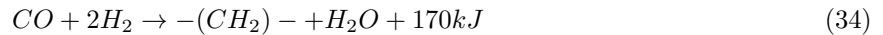
Figure 46: Slurry phase bubble reactor schematic [100]



© source unknown. All rights reserved. This content is excluded from our Creative Commons license. For more information, see <http://ocw.mit.edu/fairuse>.

Figure 47: The effect of feed ratio $r = H_2/CO$ on selectivity at $T = 300^\circ C$ [100]

Inside a FT reactor, carbon monoxide and hydrogen gas interact in the reactions shown in Equations 34 and 35 to form long, straight hydrocarbon chains called paraffins where $-(CH_2)-$ is a methylene group that polymerizes into larger molecular chains [100] and Equation 35 is the competing water shift reaction which should be minimized.



The rate of these two reactions and the distribution of their final paraffinic products depends strongly on the choice of catalyst and the entering H_2/CO ratio of the syngas stream, which in turn govern the probability of chain growth, α , and to some extent the reaction temperature. The most commonly used FT catalysts are, in decreasing order of activity, Ru, Fe, Ni, Co, and Rh [142]. Although Ru is the most active in producing high C number molecules, it is also very costly, so the second most active catalyst, Fe ($\alpha = 0.9$) was chosen for our FT reactor [100]. Our design currently employs a feed syngas ratio of around $H_2/CO = 2.0$, which is dictated by the biomass composition. The mass fraction of paraffins with carbon number n and molecular formula in final FT liquid can be found using Equation 36 where α is the chain growth probability [122] that can be calculated using Song et al's model using temperature and H_2/CO ratio [33] in Equation 37.

$$\chi_n = n(1 - \alpha_{ASF})^2 \alpha_{ASF}^{n-1} \quad (36)$$

$$\alpha = \left(\frac{0.23}{H_2/CO + 1} + 0.63 \right) \cdot [1 - 0.0039(T - 533K)] \quad (37)$$

Figure 47 and Figure 48 show effects of H_2/CO ratio and the chain growth probability factor on product selectivity in an FT reactor.

Other significant parameters in an FT reactor are the carbon conversion ratio, the superficial velocity of syngas, and the number of coolant tubes required to keep temperature controlled.

Carbon conversion ratio is the fraction of CO molecules in the feed syngas stream that is converted into larger paraffins [100]. The conversion factor increases with increased catalyst concentration, as shown

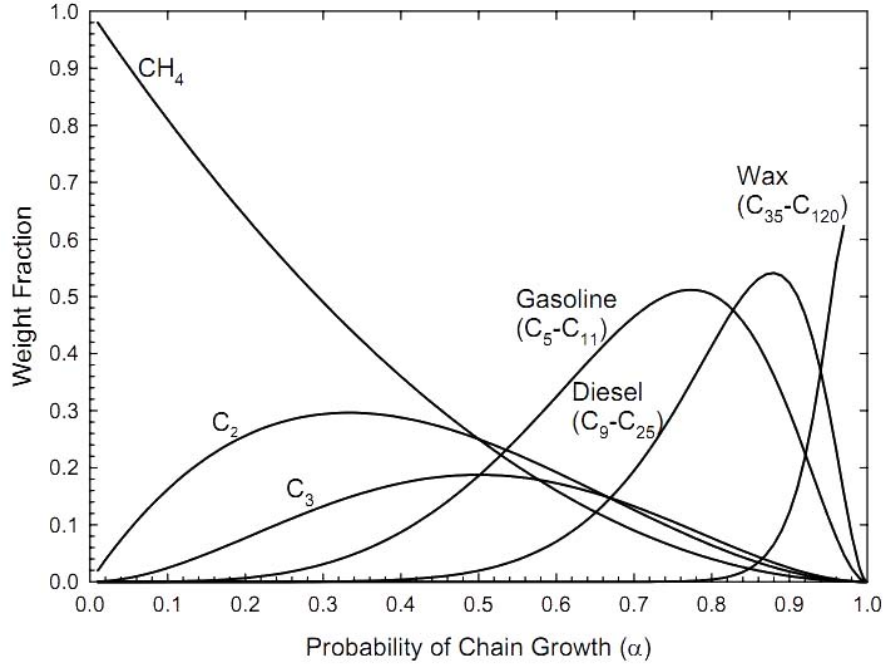


Figure 48: ASF distribution for chain growth [100]

in Figure 49, and is also influenced by reactor temperature and H_2/CO ratio of feed syngas, among other factors. A carbon conversion ratio of $\varepsilon_{smax} = 0.4$ is considered the limit for feasible commercial operation of F-T plant [122]. Our design has a ratio $\varepsilon_s = 0.35$, which maximizes conversion while staying a reasonable margin below the limit.

The total flow rate of syngas through the reactor is characterized by the superficial velocity, which is defined as the volumetric flow rate of syngas per unit cross sectional area of reactor, where \dot{n} denotes the molar flow rate and P and A represent the pressure and the cross sectional area of the reactor respectively, is shown in Equation 38.

$$U_s = \frac{\dot{V}}{A} = \frac{\dot{n}RT}{PA} = 0.05m/s \quad (38)$$

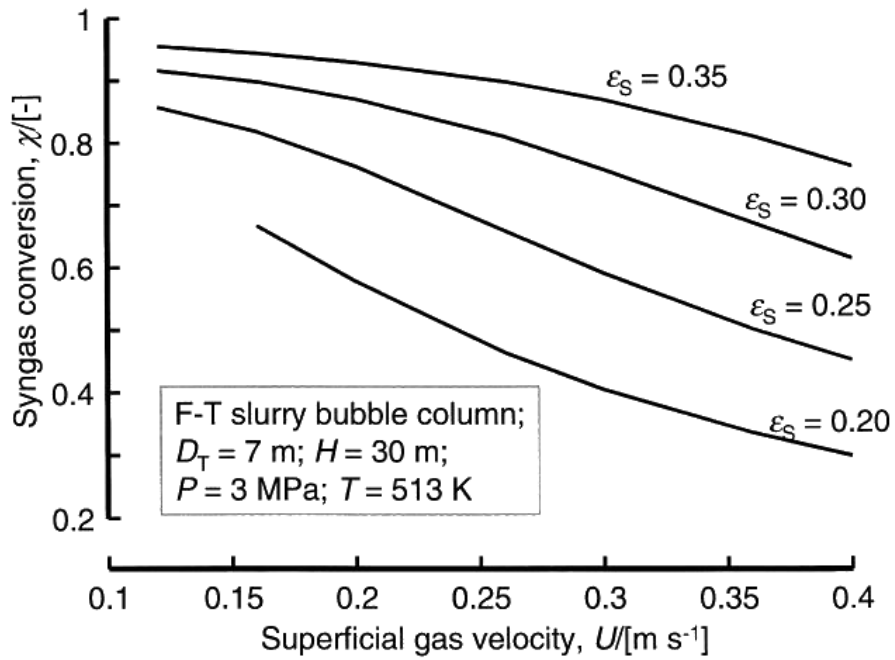
.Given our reactor size of 7 m diameter by 30 m height, along with our syngas flow rate of 14.64 kg/s, from Equation 38, the superficial velocity is found to be $U_s = 0.12$ m/s.

Currently, the FT reactor temperature has been chosen to operate at 245°C based on other published models [100]. This temperature is controlled by the coolant flow rate, which depends on the number of vertical coolant tubes needed to absorb heat and to maintain churn turbulent flow regime. As illustrated in Figure 50, the number of tubes needed increases with faster flow rate and larger catalyst concentration. The number of coolant tubes that corresponds to the superficial velocity of this design is 6,000 and pitch is 0.15 m.

Heat transfer coefficient is estimated to be 1,450 W/m² from Figure 51. This gives 41 MW for the heat exchanged with the coolant as shown in Equation 39.

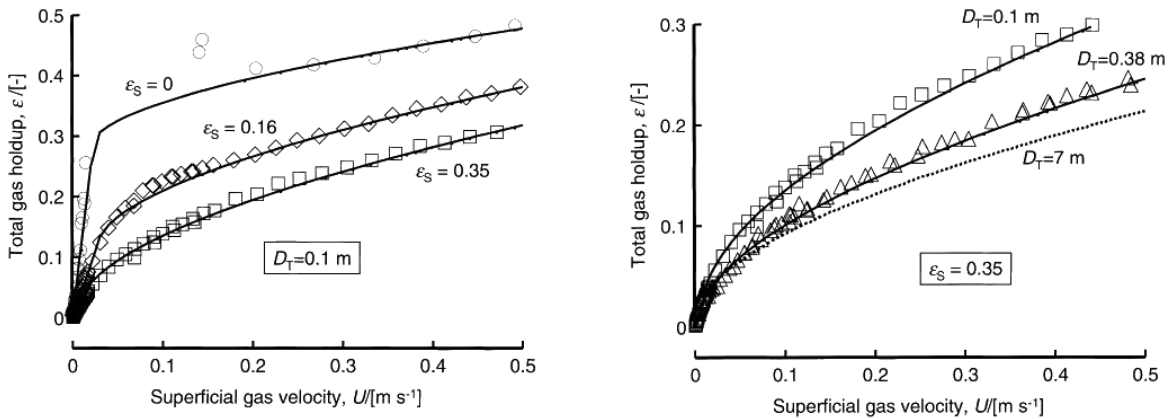
$$\dot{Q} = 6000 \cdot 30m \cdot \pi \cdot 0.05m \cdot 1450W/m^2 = 41.0MW \quad (39)$$

For coolant flow, we propose to use a one loop system at pressure 33.5 bar which corresponds to the saturation pressure at 245°C. The coolant enters the FT reactor as a condensed saturated liquid at 245°C and leaves the FT reactor as a saturated vapor. The mass flow rate in this primary heat exchange loop is 23.5 kg/s. However, if the heat were to be dumped into the environment, we must follow the EPA's limit on



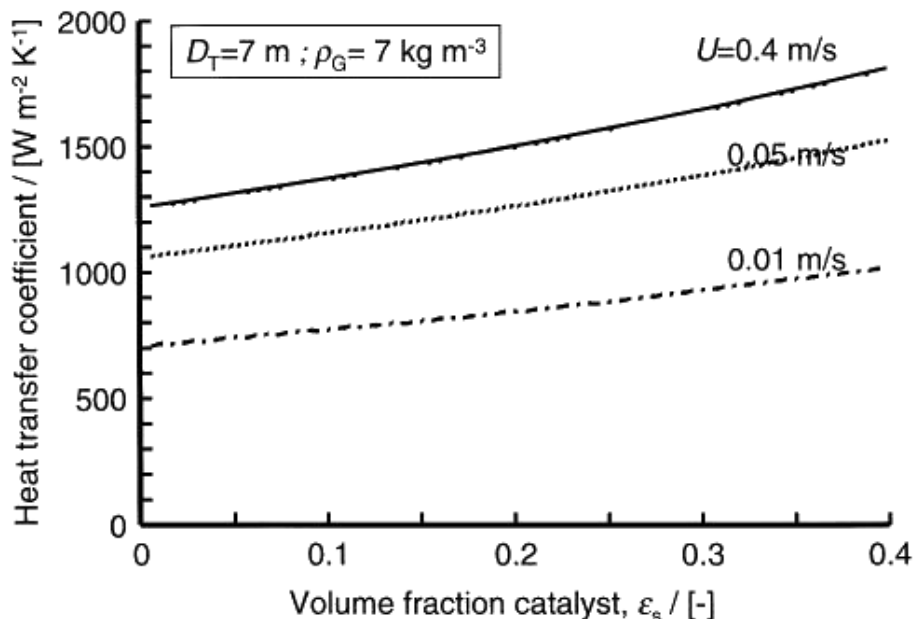
Courtesy of Elsevier, Inc., <http://www.sciencedirect.com>. Used with permission.

Figure 49: Effect of catalyst concentration on conversion ratio



Courtesy of Elsevier, Inc., <http://www.sciencedirect.com>. Used with permission.

Figure 50: Effect of superficial velocity, catalyst concentration on the number of coolant tubes [122]



Courtesy of Elsevier, Inc., <http://www.sciencedirect.com>. Used with permission.

Figure 51: Heat transfer coefficient as a function of catalyst concentration

Fraction	Carbon Number	Boiling Point (°C)	Mass Flow (kg/s)
Liquid Petroleum Gas	1-5	< 40	2.02
Light Naphtha	5-8	30-90	2.79
Heavy Naphtha	8-12	90-200	2.30
Distillate	12-20	200-300	2.65
Heavy Wax	20+	300-350	1.46

Table 24: Products of Fischer-Tropsch Process and Relative Boiling Points

the permitted temperature change of coolant water; that is, the coolant water temperature can be no more than 20°F over the intake water temperature [5]. Given that following such guidelines would require a water mass flow rate of 888 kg/s, the heat generated from the FT reaction may have to be vented or sent back to the heat processing system in order to be feasible.

In conclusion, our iron-catalyzed FT process will produce 11.22 kg/s of varying length carbon chains, as broken down in Table 24. A fair amount of naphtha and distillate, precursors of gasoline and diesel, is produced, but a significant amount of heavy wax is also produced which will need to be hydrocracked into more useable products. All the FT liquids produced in the reactor are sent on to distillation, where the lighter carbon chains are separated out, and then to the refinery to increase quality of the products using hydrogen gas.

9.6 Fractional Distillation and Refining

Outputs from the FT reactor are still primarily in the form of straight carbon chains called paraffins. Therefore, to make FT liquids ready for commercial use, they must first be distilled and refined to improve the fuel quality. The first step in refining crude FT liquids is distillation by boiling at 350°C. The various hydrocarbon components of crude oil are called fractions, which are separated from one another by a process of fractional distillation. Fractional distillation operates on the principle that different substances boil at different temperatures. As the gases rise up the distillation tower, they cool and settle out into distilled fractions with the heaviest compounds, which have the highest boiling point, settling out first. Table 24

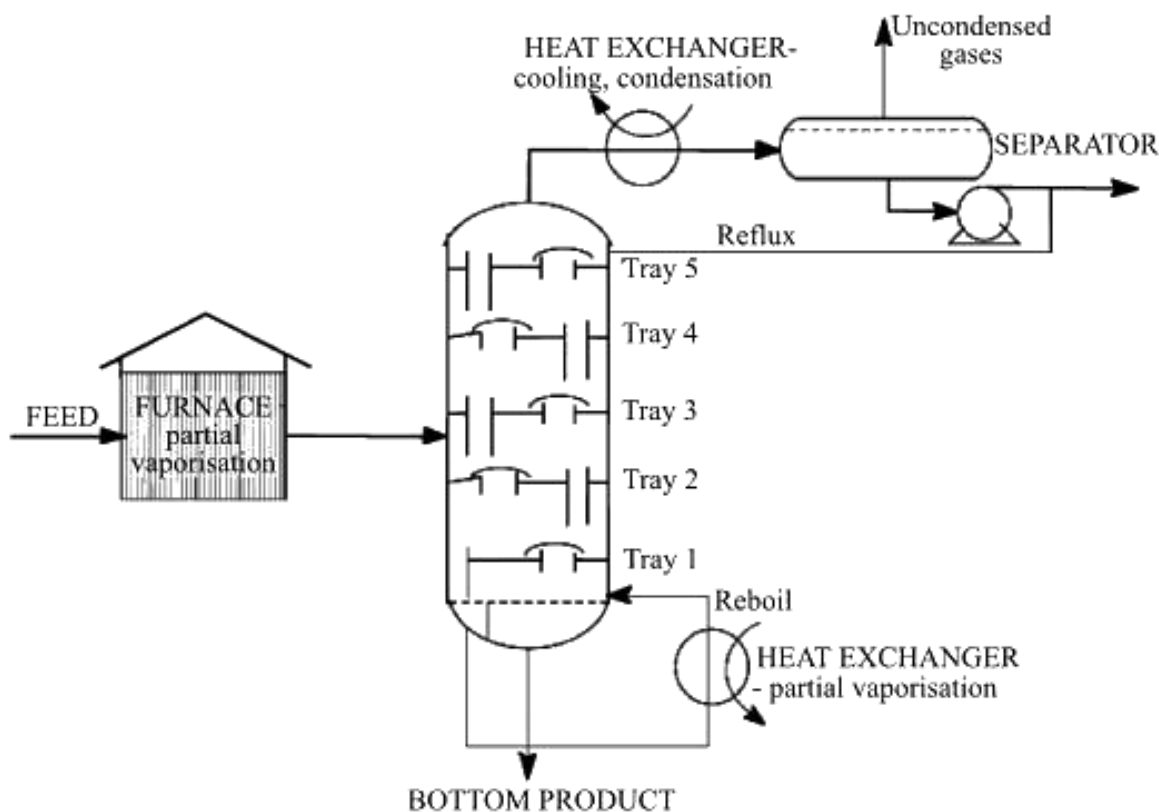


Figure 52: Distiller Schematic

shows the different products of low temperature Fischer-Tropsch Synthesis and the boiling points.

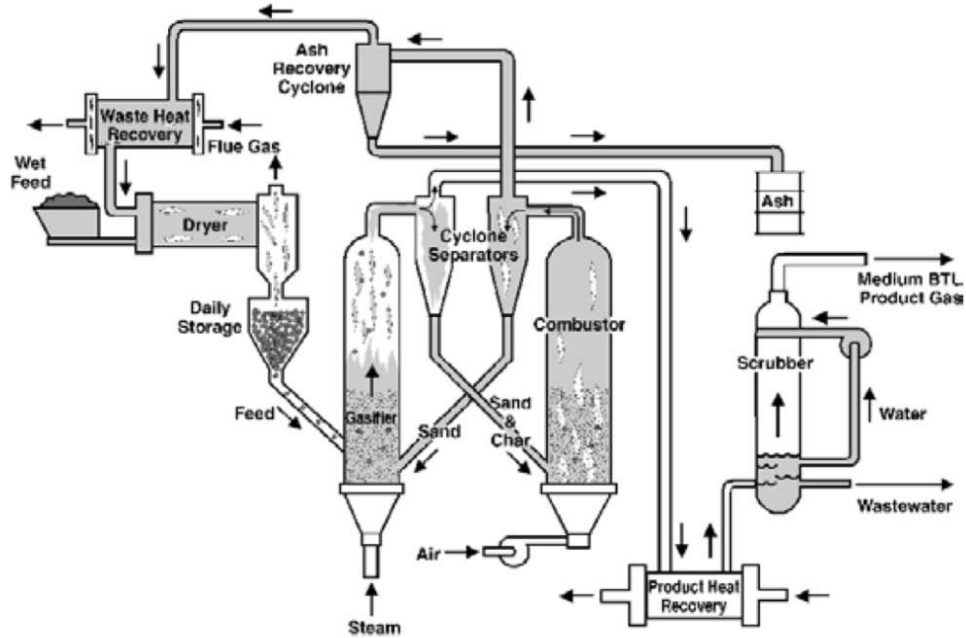
Crude oil is stored in tanks with the capacity of 20 million gallons before distillation. Inside the fractional distillation column, horizontal bubble plates located at different heights collect the fractions, which cool and condense at the proper boiling point. The crude oil is initially vaporized in the absence of air via a furnace at 350°C causing most of the oil to evaporate. As the vapor moves up the column, each fraction condenses at a different temperature and liquid fractions are collected in the trays. The hydrocarbon content with a boiling point higher than 350°C is funneled into a vacuum distillation unit which re-distills at a higher pressure. Heat exchangers are used throughout this process to recycle heat. The hot naphtha which has a low boiling point is cooled while the crude oil is preheated before entering the furnace.

Distillation separates the FT liquids into three different product streams according to molecular mass. The liquid fraction with boiling point of less than 180°C is sent out as naphtha, from 180°C to 320°C as distillate, and the remainder as a heavy wax stream [90]. Distillation is a standard process in chemical engineering and design of a distiller is relatively simple compared to other units in the whole design. Figure 52 shows a simple schematic of a generic distiller design. The vessel consists of trays for condensing separated products and heat exchangers. The three streams of separated FT hydrocarbons are then sent to refinery unit.

The refining process will closely follow a Low Temperature Fischer-Tropsch refinery design presented by Betchel [159] in Figure 53.

Four separate segments of the design will require hydrogen gas input from the hydrogen facility of respective mass flow rates, \dot{m}_{H_2} , shown by the following equations. Each equation has a fudge-factor included depending on the process.

For naphtha hydrotreatment [53],



© ASME. All rights reserved. This content is excluded from our Creative Commons license. For more information, see <http://ocw.mit.edu/fairuse>.

Figure 53: Betchel Low Temperature Fischer-Tropsch Refinery Design

$$\dot{m}_{H_2} = \frac{60\varphi_{H_2}}{\varphi_{Naphtha}} \quad (40)$$

For distillate hydrotreatment [53],

$$\dot{m}_{H_2} = \frac{140\varphi_{H_2}}{\varphi_{diesel}} \quad (41)$$

For wax hydrotreatment [93],

$$\dot{m}_{H_2} = \frac{1200\varphi_{H_2}}{\varphi_{wax}} \quad (42)$$

For C₆/C₅ isomerization [51],

$$\dot{m}_{H_2} = \dot{m}_{C_4} \frac{32kg}{ton_{C_4}} \frac{ton}{907kg} \quad (43)$$

Using Equations 40-43 along with the percent yield of each process, the input of hydrogen into the refining process was able to be calculated. Platinum/ aluminum oxide catalytic reforming process will be utilized to optimize the conversion of naphtha to diesel. The refining process in its entirety focuses on four main objectives: hydrogenation of olefins, removal of oxygen-containing compounds, hydroisomerization (to increase the octane number of the diesel fuel) and hydrocracking of n-paraffins. This refining process has been shown to increase the research octane number as high as 95.2 (the minimum rating in the United States is 87).

The fractionated distillation products are reformed using a variety of methods, including hydrogenation of olefins, removal of oxygen and sulfur containing compounds, hydroisomerization to improve the octane rating, and hydrocracking of n-paraffins to isoparaffins. As can be seen in Figure 53, H₂ gas is employed in most of these refining processes. An H₂ input of 7.9 kg/s is needed to refine our raw biofuels into consumer-ready biogasoline and biodiesel. Our estimated plant output is 662.4 tons/day or 4637 barrels/day of biogasoline and biodiesel, which is enough fuel to fill about 26,000 cars/day at 10 gallons/car.

9.7 Biofuels Results Summary

As part of a nuclear power plant coupled to hydrogen and biofuels production, a biofuels plant was designed with the capability to handle 2,903 metric tons/day of switchgrass feedstock at 20% moisture and to output 662.4 metric tons/day or 4637 barrels/day of biogasoline and biodiesel, along with other byproducts such as synthetic natural gas. Intermediate steps in the process include gasification and combustion, particulate and tar removal, acid gas cleanup, FT reactions, distillation, and refining. The plant will be located in Harris County, Texas, and will utilize a significant air input, natural water reservoir, process heat from a nuclear power plant, and hydrogen from a hydrogen production facility in order to achieve its goals. Carbon dioxide outputs will be sequestered and all other wastes will be disposed of as responsibly as reasonably achievable. The plant will create significant jobs in the local community through hiring of switchgrass farmers, switchgrass transportation and handling personnel, and other biofuels plant workers. Switchgrass expenses are estimated to be \$120k/day, while plant revenue at current prices is estimated at \$850k/day.

Part IV

Conclusions

The final design calls for a 3,575 MWt lead-bismuth eutectic (LBE) cooled fast reactor with a secondary supercritical CO₂ system. The core utilized uranium mononitride (UN) as its fuel and a ferritic/martensitic steel (T91) [67] with a 100 micron corrosion resistant layer as its cladding material [138]. The primary heat exchangers are located at the top of the reactor vessel and use shell-and-tube technology. The outlet temperature is 650°C and the inlet is 484°C. The secondary loop consists of a supercritical carbon dioxide Brayton cycle, which extracts heat from the primary LBE loop by means of three heat exchangers. The total cycle efficiency is calculated at 41.7% and produces at least 1 GWe for the grid. A zigzag channel configuration will be used for the first printed circuit heat exchanger (PCHE) and a straight channel configuration will be used for the second one in order to minimize pressure drops on the water side. Hydrogen will be produced via the UT-3 production process and high temperature steam electrolysis (HTSE). As part of a nuclear power plant coupled to hydrogen and biofuels production, a biofuels plant was designed with the capability to handle 3,500 metric tonnes per day of switchgrass feedstock at 20% moisture and to output 1,450 metric tonnes per day of biogasoline and biodiesel. Intermediate steps include gasification and combustion, particulate and tar removal, acid gas cleanup, FT reactions, distillation, and refining.

10 Future Work

10.1 Short-Term Future Work

10.1.1 Process Heat

The mass flow rate of the LBE should be calculated as a function of time, so that the change in temperature of the LBE always stays at a constant 10°C at the LBE/Helium heat exchanger. Once the function is known, the pumps can be varied during shutdown to match the mass flow rate of the LBE to the function.

Insulation must also be considered. In steady state, the temperature of the helium going through the storage device cannot drop below 605°C, or else it will start drawing latent heat from the helium. The helium enters the storage device at 606.5°C; therefore, the losses to the environment cannot exceed 1.5°C, or 1.016 MW (with a helium mass flow rate of 132 kg/s). The storage device must therefore be properly insulated to ensure that it loses less than this amount of heat to the environment.

Insulation will also be important to consider for the period between shutdown and when the stored energy will be used. The decay heat of the reactor should keep the LBE molten for approximately two weeks; during this time, there will be no helium flowing through the storage device to draw heat out, but it must still be protected against environmental losses.

Because the slabs of LiCl are so large, it is important to ensure that they are structurally secure. The effects of a support system on the flow properties of helium should be examined, in order to increase the stability of the system.

Adding another salt to the LiCl to reduce the melting temperature slightly should be examined. This would create a larger margin between the operating temperature and the melting point, so that if the operating temperature drops, the system does not solidify. This could also help reduce the cost of the LiCl, as it would result in less LiCl needed.

10.1.2 Biofuels Plant

It may be most viable for the biofuels plant to be scaled-up to maximize gasoline and diesel production. A larger plant would generate more jobs for farmers, drivers, and plant workers. It could also potentially increase our estimated profit of \$1.4 million per day. This would require more hydrogen input. Also, the biofuels plant could utilize oxygen from the hydrogen plant for the gasification step in the biofuels process. Another process that needs to be looked into more is recycling flue gas, hydrogen sulfide, carbon dioxide, and other potential wastes.

10.2 Long-Term Future Work

10.2.1 Core

With the current design of the core, a number of optimizations and more in-depth analysis were left out. On the core side, upon completion of the thermal analysis, it became apparent the current cladding material would not be suitable for the goals of the reactor. At the operating temperatures, the clad, T91 stainless steel, cannot last longer than two years. Furthermore, there is not much margin to clad failure in case of an accident scenario. A way to address the longevity of the clad would be to lower the operating temperature, however, this still does not leave much margin to failure. As such, research will need to be done to find alternative cladding materials that can better withstand the temperatures and last longer. A major advantage of the design chosen is its breeding capabilities, but without suitable cladding material, the lifetime of the core is not limited by fuel available but instead by structural issues. A similar two layer clad material to the one chosen in this design could be chosen as these class of materials have shown the ability to withstand LBE corrosion. Another potential option are silicon carbides.

Other issues on the core side of the reactor that require more study are the natural circulation during shutdown, alternative fuel types, re-arranging control rod positions to better balance power across core, and altering BOL zoning to aid in depletion effects. During shutdown the natural circulation of the core varies depending on the difference in temperature across the core and the actual values of temperatures themselves (due to viscosity effects). Developing a model to correlate how decay heat affects both of these parameters will require more analysis. While for any given difference and temperatures the natural circulation has been calculated, it is difficult to say how those will change over time and whether or not the natural circulation will maintain sufficient flow to cool the core after shutdown.

The choice to switch to UN as the fuel material instead of UO₂ was done because of the superior thermal characteristics of the UN fuel. Potential alternative fuel materials could provide the same benefits as UN but without the drawbacks to using this material, notably the requirement to enrich the nitrogen. Such materials include uranium carbides. Uranium carbide provides a better thermal conductivity (23 W/mK vs. 21 W/K) but has a lower melting point (2300°C vs 2800°C). Analysis should be done to see if UC's thermal performance is superior or comparable to UN's. If that is the case then switching to UC would be preferred, however if worse than UN the cost of the fuel would have to be considered to determine if using UN was worth it.

A depletion analysis will show how the core reactivity varies over time. If the effects of these changes in reactivity are undesired it may be necessary to alter the beginning of life core zoning. Undesired effects could include burnout of the fuel too quickly or conversely breeding could add significant reactivity to the point where it is difficult to maintain the ability to control it. Further criticality considerations would be to reconsider the location of the control rods in the core. Repositioning the rods may aid the core in maintaining a smooth power distribution. Furthermore, if reactivity increases become an issue, placing them in more reactive areas of the core (closer to the center) would increase their worth and help alleviate these issues.

10.2.2 Process Heat

The ideal configuration for the second heat exchanger would be a zigzag channels for He and straight channels for H₂O. The design group was unable to model a heat exchanger of this design due to limitations of the computational model. Future work should explore this option and also that of carrying out the heat exchange between He and H₂O in multiple stages of PCHEs or shell-and-tube heat exchangers. A Matlab model for sizing a counter flow shell-and-tube HX with He in the shell and H₂O in tubes is being developed and will be available for future studies.

10.2.3 Biofuels Plant

One problem facing the biofuels production is where to place the carbon dioxide formed from the gasification process to minimize carbon dioxide waste. Some options are to recycle, sell, store underground, or dissolve in the deep ocean. Currently General Electric has a design published for underwater and underground carbon sequestration that should be looked into for future work.

11 Economics Of Design

11.1 Expected Revenue

Some rough calculations to predict the amount of profit derived from selling electricity to the grid. After giving about 425 MWe to different processes (mostly hydrogen) and giving about 315 MWt (133 MWe) to process heat a total of 558 MWe is lost from electricity production. Assuming electricity can sell for \$0.095/kWh, the predicted revenue is \$1.272 M/day. This does not take into account operations costs or the cost to manufacture the electricity since it is beyond the scope of this course. However, this plant could be quite profitable if costs are kept low and the expected revenue from electricity sales exceeds \$1 million a day.

With mass flow rates of 1,874 barrels per day, 4,780 barrels per day for diesel and gasoline respectively, the expected revenue from the biofuel plant should be at least \$1.7 million per day. This is enough gasoline to fuel 18,500 cars per day, assuming a fifteen gallon tank. The current US demand for gasoline is 9.12 million barrels per day.

Part V

Acknowledgements

The entire design team would like to acknowledge the following people for their invaluable help with the design of this facility: Dr. Michael Short, Tyrell Arment, Koroush Shirvan, Bryan Herman, Prof. Michael Golay, Dr. Charles Forsberg, Prof. Michael Driscoll, and Prof. Neil Todreas.

References

- [1] Asme viii - div.1.
- [2] Epa federal water pollution control act.
- [3] Korea atomic energy research institute table of nuclides.
- [4] *The Westinghouse sulfur process for hydrogen production*, 2003.
- [5] *Clean Water Act NPDES Permitting Determinations for Thermal Discharge and Cooling Water Intake from Mirant Kendall Station in Cambridge, MA*, 2004.
- [6] Hydrogen production from nuclear energy via high temperature electrolysis. In *Proceedings of the International Conference on Advances in Nuclear Power Plant*, 2004.
- [7] Hydrogen production from nuclear energy via high temperature electrolysis. In *Proceedings of the International Conference on Advances in Nuclear Power Plant*, 2004.
- [8] Challenges in generating hydrogen by high temperature electrolysis using solid oxide cells. Technical report, Idaho National Laboratory, 2008.
- [9] Peterbilt motors company presents: a white paper on truck aerodynamics and fuel efficiency, May 2008.
- [10] Emission factors for locomotives, April 2009.
- [11] Alloy 20, November 2011.
- [12] Alloy 20 fasteners with world wide shipping, November 2011.
- [13] Amine plants, 2011.
- [14] Haynes 230 technical data, December 2011.
- [15] Haynes 617 alloy, November 2011.
- [16] Heatric tm, 2011.
- [17] Last federal helium reserve, near amarillo, is running out, November 2011.
- [18] Lithium chloride condensed phase thermochemistry data, November 2011.
- [19] Marine plate heat exchanger, December 2011.
- [20] Permissible weight table, December 2011.
- [21] Texas observed fire danger, December 2011.
- [22] Thermal pollution, December 2011.
- [23] Unified: Thermodynamics and propulsion, November 2011.
- [24] Wolfram alpha, November 2011.
- [25] NNFCC Project Number 10-035. Pathways to uk biofuels. Technical report, National Non-Food Crops Center and Low Carbon Vehicle Partnership, June 2010.
- [26] Isao Abe. Alkaline water electrolysis. *Energy Carriers and Conversion Systems*, 1.
- [27] A. Abhat. Low temperature latent heat thermal energy storage: Heat storage materials. *Solar Energy*, 30(4):313–332, 1983.

- [28] S. Adhikari and S. Fernando. Hydrogen membrane separation techniques. *Industrial and Engineering Chemistry Research*, 45:875–811, 2006.
- [29] Avinash Kumar Agarwal. Biofuels(alcohols and biodiesel) applicaitons as fuels for internal combustion engines. *Process in Energy and Combustion Science*, 33:233–271, 2007.
- [30] US Envirnomental Protection Agency. A comprehensive analysis of biodiesel impacts on exhaust emissions. Epa420-p-02-001, US EPA, October 2002.
- [31] A. Aochi, T. Tadokoro, K. Yoshida, H. Kameyama, M. Nobue, and T. Yamaguchi. Economical and technical evaluation of ut-3 thermochemical hydrogen production process for an industrial scale plant. *Int. J. Hydrogen Energy*, 14(7):421–429, 1989.
- [32] A. Aochi, T. Tadokoro, K. Yoshida, H. Kameyama, M. Nobue, and T. Yamaguchi. Economical and technical evaluation of ut-3 thermochemical hydrogen production process for an industrial scale plant. *Int. J. Hydrogen Energy*, 14(7):421–429, 1989.
- [33] James G Speight Mustafa Balat Ayhan Demirbas, Mrinal K Ghose. *The Biofuels Handbook*. RSC publishing, 2011.
- [34] Karin Bengtsson. Twin-bed gasification concepts for bio-sng production. Technical report, Lund University, Lund, Sweden, 2007.
- [35] BNSF. Bnsf grain elevator directory: Attebury grain, llc - tulia,tx (kimble), November 2009.
- [36] Bryan K. Boggs, Rebecca L. King, and Gerardine G. Botte. Urea electrolysis: direct hydrogen production from urine. *Chemical Communications*, pages 4859–4861, 2009.
- [37] Ulf Bossel. Does a hydrogen economy make sense? In *Proceedings of the IEEE, Vol. 94.*, 2006.
- [38] Tony Bowdery. Lng applications of diffusion bonded heat exchangers. In *AIChE Spring Meeting 6th Topical Conference on Natural Gas Utilization*, Orlando, FL, April 23-27 2006.
- [39] David I. Bransby. Cellulosic biofuel technologies. Technical report, Auburn University, February 2007.
- [40] Jacopo Buongiorno. 22.06 engineering of nuclear systems. Lecture 10, Fall 2011.
- [41] National Climatic Data Center. Average annual temperatures in texas.
- [42] Donghoon Kim Injin Sah Woo-Seog Ryu Young-sung Yoo Changheui Jang, Daejong Kim. Oxidation behaviors of wrought nickel-based superalloys in various high temperature environments. *Transactions of nonferrous metals society of China*, pages 1524–1531, 2011.
- [43] J. Charette. Pipe roughness values, February 2003.
- [44] C.K. Chow and H.F. Khartabil. Conceptual fuel channel designs for candu-scur. *Nuclear Engineering and Technology*, 40(2):139–146, 2008.
- [45] Yusuf Christi. Biodiels from microalgae. *Biotechnology Advances*, 25:294–306, February 2007.
- [46] Merichem Company. Lo-cat process for cost effective desulfurization of all types of gas streams. Schaumburg, IL.
- [47] Sandmeyer Steel Company. Alloy 304.
- [48] Leanne M. Crosbie. Hydrogen production by nuclear heat. *GENES4/ANP2003*, 2003.
- [49] Davit Danielyan. Supercritical-water-cooled reactor system - as one of the most promising type of generation iv reactor systems, November 2003.
- [50] Debabrata Das and T. Nejat Veziroglu. Hydrogen production by biological processes: a survey of literature. *International Journal of Hydrogen Energy*, 26:13–28, 2001.

- [51] Arno de Klerk and Phillip L. de Vaal. Alkylate technology selection for fischer-tropsch syncrude refining. *American Chemical Society*, 2008.
- [52] M. Faith Demirbas. Thermal energy storage and phase change materials: An overview. *Energy Sources, Part B*, pages 85–95, 2006.
- [53] R.A Diaz-Real, R.S Mann, and I.S Sambhi. Hydrotreatment of athbasca bitumen derived gas oil over ni-mo, ni-w, and co-mo catalysts. *Industrial and Engineering Chemistry Research*, 1993.
- [54] V. Dostal, M.J. Driscoll, and P. Hejzlar. A supercritical carbon dioxide cycle for next generation nuclear reactors. Technical report, Advanced Nuclear Power Technology Program., 2004.
- [55] D.Southall and S.J. Dewson, editors. *Innovative Compact Heat Exchangers*, 2010.
- [56] General Electric. Proven. tough: The 7fdl locomotive diesel engine, June 2005.
- [57] Robert J. Evans, editor. *Nuclear Hydrogen Initiative*. US DOE, AICHE Annual Meeting - Nuclear Energy and the Hydrogen Economy, 2007.
- [58] Herman Feldmann. Biomass gasification system, 2010.
- [59] Charles W. Forsberg and Mujid S. Kazimi. Nuclear hydrogen using high-temperature electrolysis and light-water reactors for peak electricity production. *Center for Advanced Nuclear Energy Systems*, April 2009.
- [60] Williams M. C. Gemmen, R. S. and K. Gerdes. Degradation measurement and analysis for cells and stacks. *J. Power Sources*, 184:251–259, 2008.
- [61] G.Hewitt. *Heat Exchanger Design Handbook*, volume 2. Begell House Inc., 1987.
- [62] H.D. Gougar. *The Very High Temperature Reactor*. Nuclear Energy Encyclopedia: Science, Technology, and Applications. John Wiley and Sons, 2011.
- [63] Carl Stoots Brian Hawks Grant Hawkes, Jame O’Brien. 3d cfd model of mult-cell high-temperature electrolysis stack. *International Journal of Hydrogen Energy*, (4189-4197), 2009.
- [64] H.G. Groehn. Thermal hydraulics of helical-type helium/helium intermediate heat exchangers (ihxs) for nuclear process heat applications of high temperature gas-cooled reactors-fundamental research and large scale tests. *Nuclear Engineering and Design*, 126:285–290, 1991.
- [65] D.C. Groeneveld and et al. The 2006 chf lookup table. *Nuclear Engineering and Design*, 237:1909–1922, 2007.
- [66] Britta K. Gross, Ian J. Sutherland, and Henk Mooiweer. Hydrogen fueling infrastructure assessment. Technical report, GM Research & Development Center, 2007.
- [67] G. Guntz, M. Julien, G. Kottmann, F. Pellicani, A Pouilly, and J.C. Vaillant. *The T91 Book*. Vallourec Industries, 1990.
- [68] Jin Haiming, Eric D. Larson, and Fuat E. Celik. Performance and cost analysis of future, commercially mature gasification-based electric power generation from switchgrass. *Biofuels, Bioprod, Bioref*, 3:142–173, 2009.
- [69] Patrick C. Hallenbeck and John R. Benemann. Biological hydrogen production; fundamentals and limiting processes. *International Journal of Hydrogen Energy*, 27:1185–1193, 2002.
- [70] Paul N. Haubenreich and J. R. Engel. Experience with the molten-salt reactor experiment. Technical report, Oak Ridge National Laboratory, 1969.
- [71] Inc. Haynes International. Haynes 625 alloy, 2001.

- [72] Anthony E. Hechanova. High temperature heat exchanger project. Technical report, UNLV Research Foundation, 2008.
- [73] A. Hoshi, D.R. Mills, A. Bittar, and T.S. Saitoh. Screening of high melting point phase change materials (pcm) in solar thermal concentrating technology based on clfr. *Solar Energy*, 79:332–339, 2005.
- [74] IAEA. Thorium fuel cycle - potential benefits and challenges. Technical report, IAEA, 2005.
- [75] Refractory Specialties Incorporated. Gemcolite azs fg26-110.
- [76] T. Ishizuka, Y. Kato, and et al, editors. *Thermal Hydraulic characteristics of Printed Circuit Heat Exchangers in a Supercritical CO2 Loop*, number NURETH 11, 2005.
- [77] N.P. Grandon J. Udagawa, P. Aguiar. Hydrogen production through steam electrolysis: Model-based steady state performance of a cathode-supported intermediate temperature solid oxide electrolysis cell. *Journal of Power Sources*, pages 127–136, 2007.
- [78] J.E.Hesselgreaves. Approaches to fouling allowances in the design of compact heat exchangers. *Applied Thermal Engineering*, 22:755–762, 2002.
- [79] J.Hejzlar. Computer code for the analysis of printed circuit heat exchangers with zigzag channels. Technical report, MIT, 2004.
- [80] J.Hesselgreaves. Compact heat exchangers. *Elsevier Science*, 2001.
- [81] Nalladurai Kaliyan and R. Vance Morey. Natural binders and solid bridge type binding mechanisms in briquettes and pellets made from corn stover and switchgrass. *Bioresource Technology*, 101(3):1082 – 1090, 2010.
- [82] H. Kameyama and K. Yoshida. Br-ca-fe water decomposition cycles for hydrogen production. *Proc. 2nd WHEC.*, pages 829–850, 1978.
- [83] H. Kameyama and K. Yoshida. Br-ca-fe water decomposition cycles for hydrogen production. *Proc. 2nd WHEC.*, pages 829–850, 1978.
- [84] Seungmo Kang, Hayri Onal, Yanfeng Ouyang, Jurgen Scheffran, and U. Deniz Tursun. Optimizing the biofuels infrastructure: Transportation networks and biorefinery locations in illinois. In *Handbook of Bioenergy Economics and Policy*, volume 33 of *Natural Resource Management and Policy*, pages 151–173. Springer New York, 2010.
- [85] Ilgi K. Kapdan and Fikret Kargi. Bio-hydrogen production from waste material. *Enzyme and Microbial Technology*, 38:569–582, 2006.
- [86] W. M. Kays and M. E. Crawford. *Convective Heat and Mass Transfer*. McGraw-Hill, 3rd edition, 1993.
- [87] James B. Kesseli, Thomas L. Wolf, F. Wells Hodous, James S. Nash, Malcolm S. Child, Robert S. Cherry, Richard L. Williamson, Ted R. Reed, and A. Joseph Palmer. Conceptual design for a high-temperature gas loop test facility. Technical report, U.S. Department of Energy, August 2006.
- [88] Ronald Allen Knief. *Nuclear engineering: theory and technology of commerical nuclear power*. American Nuclear Society, 2nd edition, 2008.
- [89] A.J. Konopka and D.P. Gregory. Hydrogen production by electrolysis: Present and future. Iecec record, Institute of Gas Technology, Chicago, Illinois, 1975.
- [90] T. G. Kreutz, Eric D. Larson, G. Liu, and R. H. Williams. Fischer-tropsch fuels from coal and biomass. Technical report, Princeton University, 2008.
- [91] National Renewable Energy Laboratory. Biomass resources. PDF, September 2007.

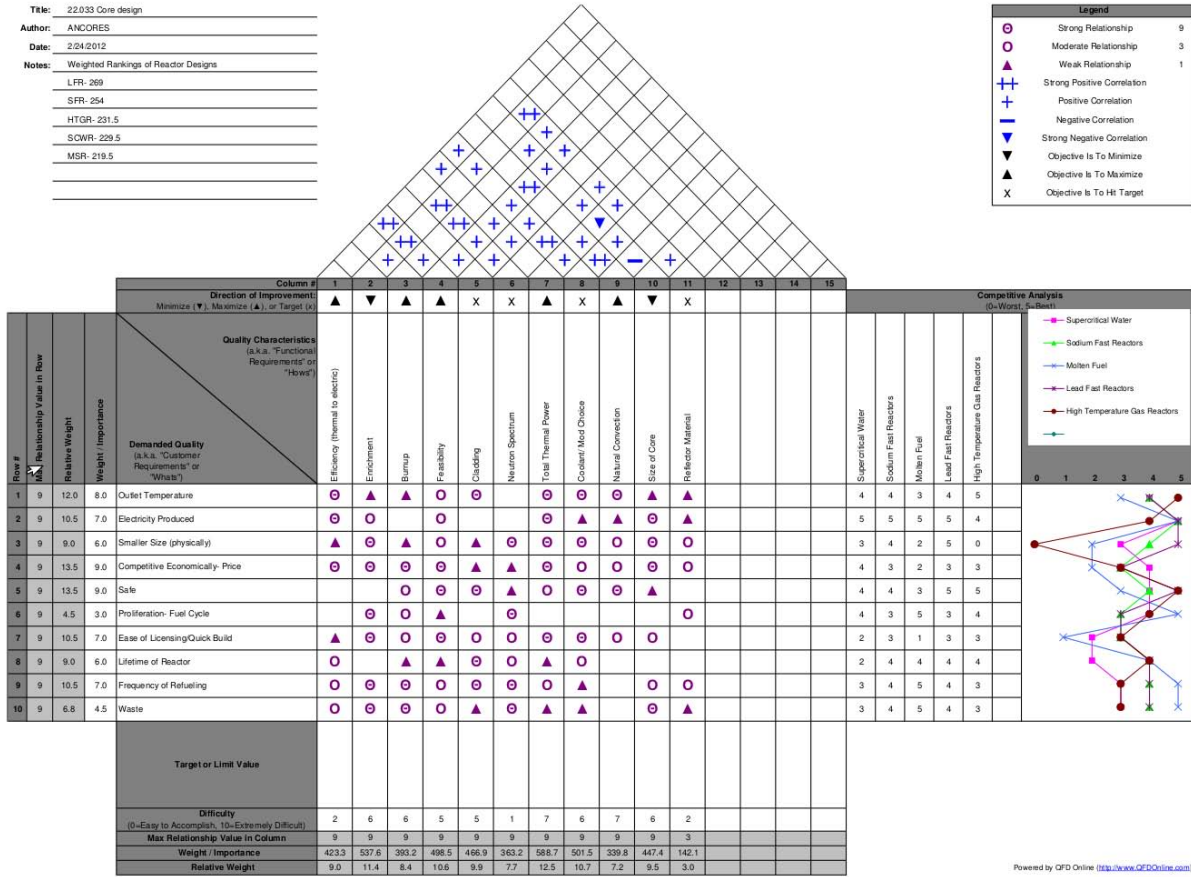
- [92] Eric D. Larson, Jin Haiming, and Fuat E. Celik. Large-scale gasification-based coproduction of fuels and electricity from switchgrass. *Biofuels, Bioprod, Bioref*, 3:174–194, 2009.
- [93] Dieter Leckel. Hydrocracking of iron-catalyzed fischer-tropsch waxes. *American Chemical Society*, 2005.
- [94] Michele A. Lewis, Manuela Serban, and John K. Basco. Hydrogen production at 500 °C using a low temperature thermochemical cycle. *Argonne National Laboratory*, lewis@m@cmt.anl.gov.
- [95] James R. Lines. Helically coiled heat exchangers offer advantages. Technical report, Graham Manufacturing Co. Inc., November 2010.
- [96] Lee R. Lynd, Eric Larson, Nathanael Greene, John Sheehan Mark Lase and, Bruce E. Dale, Samuel McLaughlin, and Michael Wang. The role of biomass in america’s energy future: framing the analysis. *Biofuels, Bioproducts and Biorefining*, 3:113–123, March 2009.
- [97] R.R. Macdonald and M.J.Driscoll. Magnesium oxide: An improved reflector for blanket-free fast reactors. *Transactions of the American Nuclear Society*, June 2010.
- [98] H.G. MacPherson, editor. *Fluid Fuel Reactors*. Addison-Wesley, 1958.
- [99] S. Majumdar, A. Moiseyev, and K. Natesan. Assessment of next generation nuclear plant intermediate heat exchanger design. Technical report, Argonne National Laboratory, 2008.
- [100] C. Maretto and R. Krishna. Modelling of bubble column slurry reactor for fischer-tropsch synthesis. *Catalysis today*, 52:279–289, 1999.
- [101] Hosein Shapouri Stephen P. Slinsky Marie E. Walsh, Daniel G. De La Torre Ugarte. Bioenergy crop production in the united states: Potential quantities, land use changes, and economic impacts on the agricultural sector. *Environmental and Resource Economics*, 24:313–333, 2003.
- [102] T. Matsuo, M. Ukei, M. Takeyama, and R. Tanaka. Strengthening of nickel-based superalloys for nuclear heat exchanger applications. *Journal of Nuclear Materials*, 22:1901–1907, 1987.
- [103] S.Khela & S.J. Matthews. Ceramic heat exchangers - materials and components performance issues. *Materials Issues in Heat Exchangers and Boilers Conference*, 1995.
- [104] H. Mehling and L. Cabeza. *Heat and cold storage with PCM: an up to date introduction into basics and applications*. Springer, 2008.
- [105] Dennis Y.C. Leung Meng Ni, Michael K.H. Leung. Technological development of hydrogen production by solid oxide electrolyzer cell (soec). *International Journal of Hydrogen Energy*, 33:2337–2353, 2008.
- [106] Microtherm. Microtherm microporous insulation vs. aspen pyrogel xt aerogel blanket. which is the better high performance insulation?
- [107] Anton Moiseyev and James J. Sienicki. Transient accident analysis of a supercritical carbon dioxide brayton cycle energy converter coupled to an autonomous lead-cooled fast reactor. *Nuclear*, 238:2094–2105, 2008.
- [108] L.F. Moody. Friction factors for pipe flow. *Transactions of the A.S.M.E*, pages 671–684, 1944.
- [109] H. Muller-Steinhagen, editor. *Heat Exchanger Fouling*. PUBLICO Publications, 2000.
- [110] N.E.Todreas and M.S.Kazimi. *Nuclear Systems Volume 1: Thermal Hydraulic Fundamentals, Second Edition*. CRC Press, 2011. Equation 11-94.
- [111] Chang H. Oh and Eung S. Kim. Design option of heat exchanger for next generation nuclear plant. Technical report, Idaho National Laboratory, 2008.
- [112] N. Ohtori, M. Salanne, and P.A. Madden. Calculations of the thermal conductivities of ionic materials by simulation with polarizable interaction potentials. *The Journal of Chemical Physics*, 130, 2009.

- [113] Haruhiko et al Ohya. Separation of hydrogen from thermochemical processes using zirconia-silica composite membrane. *Journal of Membrane Science*, 97:91–96, 1994.
- [114] M. Okazaki. High-temperature strength of ni-base superalloy coating. *Science and Technology of Advanced Materials*, 2:357–366, 2001.
- [115] Scott J. Olson. Gas cleanup technologies suitable for biomass gasification to liquid fuels. ENergy Technology Nexant, Inc., 2006 AIChE National Meeting, San Francisco, CA, 2006.
- [116] Bulent Onay and Yasutoshi Saito. Corrosion behavior of fe-20cr and ni-20cr alloys in ar-h₂o-hbr gas mixtures at 1000 k. *Oxidation of Metals*, 40, 1993.
- [117] Union Pacific. Covered hoppers, 2011.
- [118] M.A. Paisley. A promising power option - the ferco silvagas biomass gasification process - operating experience at the burlington gasifier. *ASME Turbo Expo*, 2001.
- [119] Cole Parmer. Chemical resistance database, October 2011.
- [120] Michael A. Pope. Reactor physics design of supercritical co₂-cooled fast reactors. Master’s thesis, Massachusetts Institute of Technology, September 2004.
- [121] Hideki Aita Kenji Sekita R. Hino, Katsuhiko Haga. R & d on hydrogen production by high-temperature electrolysis of steam. *Nuclear Engineering and Design*, 223:363–375, 2004.
- [122] S.T. Sie R. Krishna. Design and scale-up of the fischer-tropsch bubble column slurry reactor. *Fuel Processing Technology*, 64:73–105, 2000.
- [123] U. Eberle R. von Helmholt. Fuel cell vehicles: Status 2007. *Journal of Power Sources*, 165:833–843, 2007.
- [124] Prashaanth Ravindran, Piyush Sabharwall, and Nolan A. Anderson. Modeling a printed circuit heat exchanger with relap5-3d for the next generation nuclear plant. Technical report, Idaho National Laboratory, 2010.
- [125] New York State Energy Research and Development Authority. Hydrogen production - steam methane reforming (smr).
- [126] M.W. Rosenthal, P.R. Kasten, and R.B. Briggs. Molten-salt reactors – history, status, and potential. *Nuclear Applications and Technology*, 8(2), 1969.
- [127] Ajit Roy, Lalit Savalia, Narendra Kothapalli, and Raghunandan Karamcheti. Mechanical properties and cracking behavior of high-temperature heat-exchanger materials. In *Proceedings of the ASME Pressure Vessels and Piping Conference 2005, Vol 6*, 2005.
- [128] S. Sokhansanj S. Mani, L.G. Tabil. Evaluation of compaction equations applied to four biomass species. *Canadian Biosystems Engineering.*, 46:3.55–3.61, 2004.
- [129] Piyush Sabharwall, Eung Soo Kim, Michael McKellar, and Nolan Anderson. Process heat exchanger options for fluoride salt high temperature reactor. Technical report, Idaho National Lab, 2011.
- [130] M. Sakurai, E. Bilgen, A. Tsutsumi, and K. Yoshida. Adiabatic ut-3 thermochemical process for hydrogen production. *Int. J. Hydrogen Energy*, 21(10):865–870, 1996.
- [131] M. Sakurai, A. Tsutsumi, and K. Yoshida. Improvement of ca-pellet reactivity in ut-3 thermochemical hydrogen production cycle. *Int. J. Hydrogen Energy*, 20(4):297–301, 1995.
- [132] B. K. et al Sea. Formation of hydrogen permselective silica membrane for elevated temperature hydrogen recovery from a mixture containing steam. *Gas Separation & Purification*, 10(3):812–881, 1996.
- [133] Ramesh K. Shah and Dusan P. Sekulic. *Fundamentals of Heat Exchanger Design*. John Wiley and Sons, 2003.

- [134] J. Sheehan, T. Dunahay, J. Benemann, and P. Roessler. A look back at the u.s. department of energy’s aquatic species program—biodiesel from algae. Nrel/tp-580-24190, National Renewable Energy Laboratory, Golden, CO, 1998.
- [135] S. R. Sherman and Y. Chen. Heat exchanger testing requirements and facility needs for the nhi/ngnp project. Technical Report WSRC-STI-2008-00152, 2008.
- [136] Yoichiro Shimazu. Current situation of msr development in japan. Presentation.
- [137] K. Shirvan. *The Design of a Compact Integral Medium Size PWR: The CIRIS*. PhD thesis, MIT, 2010.
- [138] Michael Short. *The Design of a Functionally Graded Composite for Service in High Temperature Lead and Lead-Bismuth (LBE) Cooled Nuclear Reactors*. PhD thesis, MIT, 2010.
- [139] Michael Short. Core group: Non-pwr/bwr reactors. Lecture, September 2011.
- [140] J. J. Sienicki, A. V. Moiseyev, D. C. Wade, M. T. Farmer, C. P. Tzanos, J. A. Stillman, J. W. Holland, P. V. Petkov, I. U. Therios, R. F. Kulak, and Q. Wu. The star-lm lead-cooled closed fuel cycle fast reactor coupled to a supercritical carbon dioxide brayton cycle advanced power converter. In *Global*, New Orleans, LA, November 16-20 2003.
- [141] E. M. Sparrow and Jr. Loeffler, A. L. Longitudinal laminar flow between cylinders arranged in regular array. *A.I.Ch.E.*, 5:325, 1959.
- [142] P.L. Spath and D.C. Dayton. Preliminary screening-technical and economic assessment of synthesis gas to fuels and chemicals with emphasis on the potential for biomass-derived syngas. Technical report, National Renewable Energy Laboratory, 2003.
- [143] Mohamed S. El-Genk Steven B. Ross and R. Bruce Matthews. Thermal conductivity correlation for uranium nitride fuel between 10 and 1923 k. *Journal of Nuclear Materials*, 151:313–317, 1988.
- [144] Hiroshi; P. C. Paris Tada. *The Stress Analysis of Cracks Handbook (3 ed.)*. American Society of Mechanical Engineers, 2005.
- [145] Y. Tadokoro, T. Kajiyama, T.Yamaguichi, N.Sakai, H. Kameyama, and K. Yoshida. Technical evaluation of ut-3 thermochemical hydrogen production process for an industrial scale plant. *Int. J. Hydrogen Energy*, 22(1):49–56, 1996.
- [146] Hajime Takeya Toshio Hirai Takashi Goto, Chen-Yan Guo. Coating of titanium carbide films on stainless steel by chemical vapor deposition and their corrosion behavior in a br2-o2-ar atmosphere. *Journal of Material Science*, 27:233–239, 1992.
- [147] Allison M. Thomson and Cesar R. Izarrualde. Simulating potential switchgrass production in the united states. Pnnl-19072, US Department of Energy, December 2009.
- [148] Anna Nikiforova; Pavel Hejzlar; Neil E. Todreas. Lead-cooled flexible conversion ratio fast reactor. *Nuclear Engineering and Design*, 239:2596–2611, 2009.
- [149] N.E. Todreas and M.S. Kazimi. *Nuclear Systems, Vol 1*. Taylor and Francis, 1989.
- [150] Pavel Hejzlar; Neil E. Todreas. Flexible conversion ratio fast reactor systems evaluation final report. *Nuclear Energy Research Initiative, Project 06-040*, 2008.
- [151] T. B. Tokareva and V. V. Smolin. Corrosion resistance of structural materials in lithium chloride. *Chemical and Petroleum Engineering*, 10:139, 1974.
- [152] The Engineering ToolBox. Stress in thick-walled tubes or cylinders.
- [153] Michael Felderhoff Ulrich Eberle and Ferdi Schuth. Chemical and physical solutions for hydrogen storage. *Angew Chem Int Ed*, 48:6608–6630, 2009.

- [154] US. Code of federal regulations.
- [155] U.S. Geological Survey U.S. Department of the Interior. Texas precipitation. The National Atlas of the United States of America, 2006.
- [156] X. Vitart, A. Le Duigou, and P. Carles. Hydrogen production using the sulfur-iodine cycle coupled to a vht: An overview. *Energy Conversion and Management*, 47:2740–2747, 2006.
- [157] X. Vitart, A. Le Duigou, and P. Carles. Hydrogen production using the sulfur-iodine cycle coupled to a vht: An overview. *Energy Conversion and Management*, 47:2740–2747, 2006.
- [158] Qiuwang Wang, Qiuyang Chen, Guidong Chen, and Min Zeng. Numerical investigation on combined multiple shell-pass shell-and tube heat exchanger with continuous helical baffles. *International Journal of Heat and Mass Transfer*, 52:1214–1222, 2008.
- [159] Eric D. Larson Xiangbo Guo, Guangjian Liu. High-octane gasoline production by upgrading low-temperature fischer-tropsch syncrude. *American Chemical Society*, 2011.
- [160] X.Li, D.Kinimont, and et al. Alloy 617 for the high temperature diffusion-bonded compact heat exchangers. In *ICAPP Proceedings*, 2008.
- [161] B. YildizI and M.S. Kazimi. Hydrogen production using high-temperature steam electrolysis supported by advanced gas reactors with supercritical co2 cycles. *Nuclear Technology*, 2006.
- [162] Seungmo Kang Yanfeng Ouyang Yun Bai, Taesung Hwang. Biofuel refinery location and supply chain planning under traffic congestion. *Transportation Research Part B: Methodological*, 45(1):162 – 175, 2011.

Title: 22.033 Core design
 Author: ANCORES
 Date: 2/24/2012
 Notes: Weighted Rankings of Reactor Designs
 LFR- 269
 SFR- 254
 HTGR- 231.5
 SOWR- 229.5
 MSR- 219.5



HoQ template courtesy of QFD Online. Used with permission.

Figure 54: Core house of quality

Part VI

Appendix A: Core Parameter QFD

The QFD method is used to “transform user demands into design quality” [QFD2012]. A house of quality is part of this method and helps correlate what is desired from a technical and commercial standpoint and can be used to compare different products (in this case different reactor designs). The house of quality for the core design can be seen in Figure 54.

The QFD method has been used by many different designs across a wide array of fields. It helps sort through design parameters to identify which areas of a design are most important to focus on. It does this by comparing product goals, which can be seen on the left in the house of quality, and design parameters, which can be seen on the top of the house of quality. The product goals are given a weight on a scale from one to ten to determine how important each is relative to the others. The product goals are then analyzed with respect to the design parameters. The goals and parameters are judged to have either a strong, moderate, weak, or no relationship. The difficulty of optimizing the design parameter is then also judged on 0-10 scale. The combination of the importance of the design goals, relationship to design parameters, and difficulty to optimize a parameter are then used to produce relative weight for each design parameter. This weight helps focus designers on the most important features of a product.

Other features of the house of quality are the “roof” and the competitive analysis. The roof compares different design parameters and shows how each parameter relates to another. The parameters are first looked at to see if the goal is to maximize, minimize, or hit a target for the parameter for optimization.

Then each is compared as to how optimizing those parameters effects the others. There is either a strong positive, positive, negative, strong negative, or neutral relationship. This tool aids designers in identifying which parameters will be the most difficult or easiest to optimize based on how they effect other parameters. Finally, the competitive analysis compares different products, in our case reactor designs, based on the design goals. The products are rated on a scale of 0-5 to see how they perform in the design goal categories. The core designers took these performance rankings and multiplied them by the design goal importance and were able to get a weighted ranking of the different designs. The final design chose, a lead cooled fast reactor, was the highest ranked design and helped justify the decision.

Part VII

Appendix B: Criticality Model

Criticality Model

Code run in MCNP5 for criticality data

22.033 Fall 2011 Core Design v16_3_out

```
c =====
c =====> Cell cards
c =====
c =====> Fuel pin, clad and surrounding sodium; Enrich == 15%,15%,10%(going up)
c   Inner Fuel
101  71 -12.8900 -1000    u=1 $ lower fuel
102  71 -12.8900 -1005    u=1 $ middle fuel
103   7 -12.8900 -1006    u=1 $ top fuel
104   3 -10.1920 1007 -1001  u=1 $ gap w/ coolant
105  21 0.04291 1001 -1002  u=1 $ protective layer (m21)
106   2 0.04291 1002 -1003  u=1 $ steel clad   (m2 )
107  21 0.04291 1003 -1004  u=1 $ protective layer (m21)
108   3 -10.1920 1004      u=1 $ coolant
c   Intermediate Fuel
109  72 -12.8900 -1000    u=2 $ fuel,
110  72 -12.8900 -1005    u=2 $ fuel,
111  71 -12.8900 -1006    u=2 $ fuel,
112   3 -10.1920 1007 -1001  u=2 $ gap w/ coolant
113  21 0.04291 1001 -1002  u=2 $ protective layer (m21)
114   2 0.04291 1002 -1003  u=2 $ steel clad   (m2 )
115  21 0.04291 1003 -1004  u=2 $ protective layer (m21)
116   3 -10.1920 1004      u=2 $ coolant
c   Outer Fuel
117  72 -12.8900 -1000    u=3 $ fuel,
118  72 -12.8900 -1005    u=3 $ fuel,
119  71 -12.8900 -1006    u=3 $ fuel,
120   3 -10.1920 1007 -1001  u=3 $ gap w/ coolant
121  21 0.04291 1001 -1002  u=3 $ protective layer (m21)
122   2 0.04291 1002 -1003  u=3 $ steel clad   (m2 )
123  21 0.04291 1003 -1004  u=3 $ protective layer (m21)
124   3 -10.1920 1004      u=3 $ coolant
c   =====> Pin coolant channels
200   3 -10.1920 -1004    u=4 $ coolant
201   3 -10.1920 1004     u=4 $ coolant
c   =====> Pin Lattice
202   0      -2000  u=5 lat=2
      fill=-6:6 -6:6 0:0
0 0 0 0 0 0 0 0 4 1 4 0 0 $ROW 1
0 0 0 0 0 0 4 1 1 1 1 4 0 $ROW 2
0 0 0 0 4 1 1 1 1 1 1 1 4 $ROW 3
0 0 0 1 1 1 1 1 1 1 1 1 1 $ROW 4
0 0 4 1 1 1 1 1 1 1 1 1 4 $ROW 5
```

```

0 0 1 1 1 1 1 1 1 1 1 1 0 $ROW 6
0 4 1 1 1 1 1 1 1 1 1 4 0 $ROW 7
0 1 1 1 1 1 1 1 1 1 1 0 0 $ROW 8
4 1 1 1 1 1 1 1 1 1 4 0 0 $ROW 9
1 1 1 1 1 1 1 1 1 0 0 0 $ROW 10
4 1 1 1 1 1 1 1 4 0 0 0 0 $ROW 11
0 4 1 1 1 1 4 0 0 0 0 0 0 $ROW 12
0 0 4 1 4 0 0 0 0 0 0 0 0 $ROW 13

```

c

```

203 0 -2000 u=6 lat=2
fill=-6:6 -6:6 0:0
0 0 0 0 0 0 0 4 2 4 0 0 $ROW 1
0 0 0 0 0 4 2 2 2 2 4 0 $ROW 2
0 0 0 0 4 2 2 2 2 2 2 4 $ROW 3
0 0 0 2 2 2 2 2 2 2 2 2 $ROW 4
0 0 4 2 2 2 2 2 2 2 2 4 $ROW 5
0 0 2 2 2 2 2 2 2 2 2 0 $ROW 6
0 4 2 2 2 2 2 2 2 2 4 0 $ROW 7
0 2 2 2 2 2 2 2 2 2 0 0 $ROW 8
4 2 2 2 2 2 2 2 2 4 0 0 $ROW 9
2 2 2 2 2 2 2 2 2 0 0 0 $ROW 10
4 2 2 2 2 2 2 4 0 0 0 0 $ROW 11
0 4 2 2 2 2 4 0 0 0 0 0 $ROW 12
0 0 4 2 4 0 0 0 0 0 0 0 $ROW 13

```

c

```

204 0 -2000 u=7 lat=2
fill=-6:6 -6:6 0:0
0 0 0 0 0 0 0 4 3 4 0 0 $ROW 1
0 0 0 0 0 4 3 3 3 3 4 0 $ROW 4
0 0 0 0 4 3 3 3 3 3 3 4 $ROW 3
0 0 0 3 3 3 3 3 3 3 3 3 $ROW 4
0 0 4 3 3 3 3 3 3 3 3 4 $ROW 5
0 0 3 3 3 3 3 3 3 3 3 0 $ROW 6
0 4 3 3 3 3 3 3 3 3 4 0 $ROW 7
0 3 3 3 3 3 3 3 3 3 0 0 $ROW 8
4 3 3 3 3 3 3 3 3 4 0 0 $ROW 9
3 3 3 3 3 3 3 3 3 0 0 0 $ROW 10
4 3 3 3 3 3 3 4 0 0 0 0 $ROW 11
0 4 3 3 3 3 4 0 0 0 0 0 $ROW 12
0 0 4 3 4 0 0 0 0 0 0 0 $ROW 13

```

c =====> Inner Fuel Assembly

```

300 0 -3000 u=8 fill=5 $ assembly fuel lattice
301 21 0.042910 3000 -3001 u=8 $ protective layer (m21)
302 2 0.042910 3001 -3002 u=8 $ steel clad (m2)
303 21 0.042910 3002 -3003 u=8 $ protective layer (m21)
304 3 -10.1920 3003 u=8 $ assembly gap

```

c =====> Intermediate Fuel Assembly


```

9 9 9 9 9 9 9 9 13 12 11 11 11 10 10 10 14 10 10 10 11 11 11 12 13 9 9
9 $ROW 9
9 9 9 9 9 9 9 9 13 12 11 11 11 10 10 10 10 10 10 10 11 11 11 12 13 9 9
9 $ROW 10
9 9 9 9 9 9 9 9 13 12 11 11 11 10 10 14 10 10 10 14 10 10 11 11 11 12 13 9
9 9 $ROW 11
9 9 9 9 9 9 13 12 11 11 11 14 10 10 8 8 8 8 10 10 14 11 11 11 12 13 9 9 9 $ROW 12
9 9 9 9 9 13 12 11 11 11 10 10 10 8 8 8 8 10 10 10 11 11 11 12 13 9 9 9 $ROW 13
9 9 9 9 13 12 11 11 11 10 10 10 8 8 8 8 10 10 10 11 11 11 12 13 9 9 9 $ROW 14
9 9 9 13 12 11 14 11 10 10 14 8 8 8 8 8 8 14 10 10 11 14 11 12 13 9 9 9 $ROW 15
9 9 9 13 12 11 11 11 10 10 10 8 8 8 8 8 10 10 10 11 11 11 12 13 9 9 9 $ROW 16
9 9 9 13 12 11 11 11 10 10 10 8 8 8 8 8 10 10 10 11 11 11 12 13 9 9 9 $ROW 17
9 9 9 13 12 11 11 11 14 10 10 8 8 8 8 10 10 14 11 11 11 12 13 9 9 9 9 9 $ROW 18
9 9 9 13 12 11 11 11 10 10 14 10 10 10 14 10 10 11 11 11 12 13 9 9 9 9 9
9 9 $ROW 19
9 9 9 13 12 11 11 11 10 10 10 10 10 10 10 10 11 11 11 12 13 9 9 9 9 9 9 9
9 $ROW 20
9 9 9 13 12 11 11 11 10 10 10 14 10 10 10 11 11 11 12 13 9 9 9 9 9 9 9
9 $ROW 21
9 9 9 13 12 11 11 11 11 11 11 11 11 11 11 11 11 12 13 9 9 9 9 9 9 9 9 9 $ROW 22
9 9 9 13 12 11 14 11 11 11 11 11 11 11 14 11 12 13 9 9 9 9 9 9 9 9 9 9 $ROW 23
9 9 9 13 12 11 11 11 11 11 11 11 11 11 11 12 13 9 9 9 9 9 9 9 9 9 9 9 $ROW 24
9 9 9 13 12 12 12 12 12 12 12 12 12 12 12 12 13 9 9 9 9 9 9 9 9 9 9 9 $ROW 25
9 9 9 13 13 13 13 13 13 13 13 13 13 13 13 13 13 9 9 9 9 9 9 9 9 9 9 9 $ROW 26
9 9 9 9 9 9 9 9 9 9 9 9 9 9 9 9 9 9 9 9 9 9 9 9 9 9 9 $ROW 27
9 9 9 9 9 9 9 9 9 9 9 9 9 9 9 9 9 9 9 9 9 9 9 9 9 9 9 $ROW 28
9 9 9 9 9 9 9 9 9 9 9 9 9 9 9 9 9 9 9 9 9 9 9 9 9 9 9 $ROW 29

```

c =====> Full model

```

500 3 -10.1920 -5000 fill=15 $ lattice of elements
501 2 0.042910 5001 -5002 $ clad
502 3 -10.1920 -5003 $ upper plenum
503 3 -10.1920 -5004 $ lower plenum
504 0 5002 $ outer void

```

c =====

c =====

c =====> surface cards

c =====

c =====> pin interior

```

1000 RCC 0. 0. 0. 0. 0. 134. 0.500 $ Adjust for axial zoning regions
1005 RCC 0. 0. 134. 0. 0. 133. 0.500
1006 RCC 0. 0. 267. 0. 0. 133. 0.500
1007 RCC 0. 0. 0. 0. 0. 400. 0.500
1001 RCC 0. 0. 0. 0. 0. 400. 0.614
1002 RCC 0. 0. 0. 0. 0. 400. 0.615
1003 RCC 0. 0. 0. 0. 0. 400. 0.624
1004 RCC 0. 0. 0. 0. 0. 400. 0.625

```

```

c =====> pin shell
2000 HEX 0. 0. 0. 0. 0. 400. 0. 1. 0.
c =====> assembly inner
3000 HEX 0. 0. 0. 0. 0. 400. 0. 10.000 0.
3001 HEX 0. 0. 0. 0. 0. 400. 0. 10.010 0.
3002 HEX 0. 0. 0. 0. 0. 400. 0. 11.790 0.
3003 HEX 0. 0. 0. 0. 0. 400. 0. 11.800 0.
c =====> aseembly shell
4000 HEX 0. 0. 0. 0. 0. 400. 0. 12. 0.
c =====> reactor vessel
5000 RCC 0. 0. 0. 0. 0. 400. 290.      $ Pressure vessel for 12 rings
5001 RCC 0. 0. -50. 0. 0. 500. 290.
5002 RCC 0. 0. -50. 0. 0. 500. 300.
5003 RCC 0. 0. 400. 0. 0. 50. 290.
5004 RCC 0. 0. -50. 0. 0. 50. 290.
c =====> control pin
8000 RCC 0. 0. 399. 0. 0. 1. 1.500
8001 RCC 0. 0. 399. 0. 0. 1. 1.510
8002 RCC 0. 0. 399. 0. 0. 1. 2.000
8003 HEX 0. 0. 399. 0. 0. 1. 0. 10.000 0.
8004 HEX 0. 0. 399. 0. 0. 1. 0. 11.790 0.
8005 HEX 0. 0. 399. 0. 0. 1. 0. 11.800 0.
8006 HEX 0. 0. 0. 0. 0. 399. 0. 11.800 0.
c =====

c =====
c =====> data cards for problem
c =====

c =====> run description
kcode 10000 1.0 40 130
RAND GEN = 2
imp:n 1 69r 0.
c =====> source description
sdef erg=d1 cel=d2 axs=0 0 1 rad=d3 ext=d4
sp1 -3 .988 2.249 $ Watt spectrum, thermal u235 fission
sp2 D 1. 1r
si2 L 500:400(0 0 0):300:202(0 0 0):-101
      500:400(1 1 0):300:202(0 0 0):-101
c 500:400(4 7 0):300:202(0 0 0):-101
c 500:400(-3 -7 0):300:202(0 0 0):-101
c 500:400(-6 0 0):300:202(0 0 0):-101
c 500:400(5 0 0):300:202(0 0 0):-101
sp3 C 0. 1.
si3 H 0. 0.5
sp4 C 0. 1.
si4 H 0. 400.
c =====> material cards

```

m1 92238 2.6667e-1 \$ UO2 fuel enrich 20 percent
92235 0.6667e-1
8016 6.6667e-1
m11 92238 2.8333e-1 \$ fuel enrich 15 percent
92235 0.5000e-1
8016 6.6667e-1
m12 92238 3.0000e-1 \$ fuel enrich 10 percent
92235 0.3333e-1
8016 6.6667e-1
m13 92238 2.5000e-1 \$ fuel enrich 25 percent
92235 0.8333e-1
8016 6.6667e-1
m14 92238 2.74725e-1 \$ fuel enrich 17.5 percent
92235 0.58275e-1
8016 6.6667e-1
m15 92238 2.91375e-1 \$ fuel enrich 12.5 percent
92235 0.41625e-1
8016 6.6667e-1
m2 24052 -0.073315375 \$ stainless steel T91
24053 -0.008313375
24054 -0.002069375
24050 -0.003801875
14028 -0.0036892
14029 -0.0001868
14030 -0.000124
42092 -0.0014098
42094 -0.00087875
42095 -0.0015124
42096 -0.0015846
42097 -0.00090725
42098 -0.00229235
42100 -0.00091485
25055 -0.0045
c 23050 -0.000005375
23051 -0.002150000
28058 -0.00272308
28060 -0.00104892
28061 -0.0000456
28062 -0.00014536
28064 -0.00003704
41093 -0.0008
6012 -0.000989
6013 -0.000011
7014 -0.000697438
7015 -0.000002562
15031 -0.0002
16032 -0.00009502

	16033	-0.00000075	
	16034	-0.00000423	
c	16035	-0.00000002	
	26054	-0.0513619	
	26056	-0.81222646	
	26057	-0.0194821	
	26058	-0.00247954	
m21	24052	-0.100548	\$ stainless steel outer inner protective
	24053	-0.011401	
	24054	-0.002838	
	24050	-0.005214	
	14028	-0.018846	
	14029	-0.000934	
	14030	-0.00062	
	25055	-0.0001	
	28058	-0.000068077	
	28060	-0.000026223	
	28061	-0.00000114	
	28062	-0.000003634	
	28064	-0.000000926	
	6012	-0.00000989	
	6013	-0.00000011	
	15031	-0.00006	
	16032	-0.000057012	
	16033	-0.00000045	
	16034	-0.000002538	
c	16035	-0.000000012	
	26054	-0.04986086	
	26056	-0.788489324	
	26057	-0.01891274	
	26058	-0.0024070760	
m3	82204	-0.00623	\$ LBE
	82206	-0.107245	
	82207	-0.098345	
	82208	-0.23318	
	83209	-0.555	
m4	8016	0.499805	\$ reflector MgO
	8017	0.000195	
c	8018	0.001005	
	12024	0.39495	
	12025	0.05	
	12026	0.05505	
m5	5010	0.1592	\$ control rods B4C
	5011	0.6408	
	6012	0.1978	
	6013	0.0022	
m6	5010	0.1592	\$ Shield B4C

5011 0.6408

6012 0.1978

6013 0.0022

m7 7015 0.5 \$ Uranium Mononitride
92238 0.45 \$ 10% enriched
92235 0.05

m71 7015 0.5 \$ 12.5% enriched
92238 0.4375
92235 0.0625

m72 7015 0.5 \$ 15% enriched
92238 0.425
92235 0.075

m73 7015 0.5 \$ 17.5% enriched
92238 0.4125
92235 0.0875

m74 7015 0.5 \$ 20% enriched
92238 0.4
92235 0.1

c =====> tallies:

F6:N 101

F16:N 500

c F26:N (101<202[0 0 0]<300<400[0 0 0]<500)

F7:N 101

F17:N 500

Part VIII

Appendix C: Investigation of PCHE thermal hydraulics

Introduction

This appendix explains the computational model that was used to study thermal hydraulics performance of PCHEs. The thermal hydraulic parameters of 35 MW PCHEs were studied as a function of channel configuration, channel diameter and hot fluid mass flow rate. The impact of these design parameters on PCHE volume, heat transfer properties and pressure drop are discussed in the following sections. The results of this study informed the design choices for the PCHEs in the Process Heat System.

Computational model

A nodal computational model implemented in Fortran, developed at MIT by Hejzlar and Dostal [54] and improved upon by J.Hejzlar [79] and Shirvan [137], is being used to optimize the PCHEs in the Process Heat system. The model assumes that:

- The total mass flow rate is uniformly distributed among the channels,
- The wall channel temperature is uniform at every axial node and
- Cold and hot plates have the same number of flow channels.

The fortran code uses a counterflow channel configuration and can be used to analyze both straight and zigzag channels. Given the the inlet temperatures and pressures of the hot and cold fluids as well as the number of nodes in a channel, the code iterates to find the length of each node and sums them to calculate the length of each channel. Shown in Figure 55 is a schematic of the treatment of a single PCHE channel by the nodal model.

The model uses a constant Nu of 4.089 for the laminar regime ($Re < 2300$), linear interpolation is used to find Nu for the transitional regime ($2300 < Re < 5000$) and the Gnielsinki correlation is used for the turbulent ($Re > 5000$) regime [54]. Single phase and two phase pressure drops are modeled using experimental results from the Tokyo Institute of Technology [76] and the Taylor correlation [78] respectively.

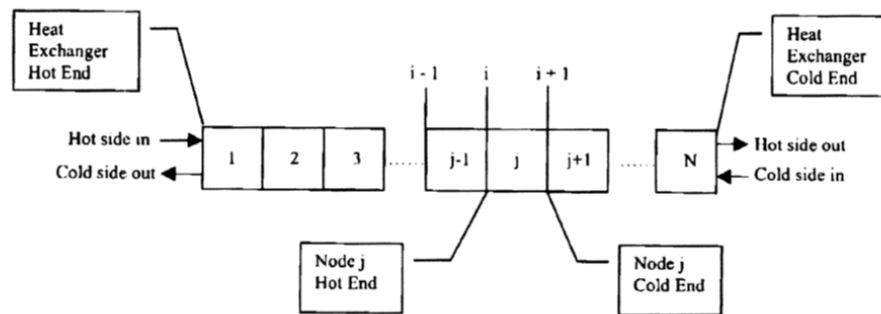


Figure 55: PCHE nodalization [54]

Comparison of straight and zigzag channel PCHEs

PCHEs can either have straight or zigzag channels. For two PCHEs of the same heat rate, the zigzag channel PCHEs are more compact but have higher pressure drops. Table 25 compares a straight channel PCHE with

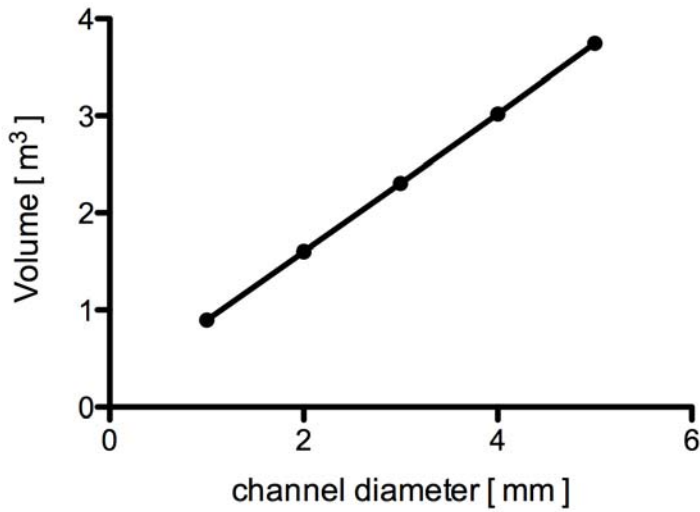
a zigzag channel PCHE. For both PCHEs, S-CO₂ and He are the hot and cold fluids respectively. Mass flow rates of 22 kg/s and 90 kg/s were used for the cold and hot fluid respectively. A bend angle of 57.5°, as recommended by Heatric and studied by Shirvan [137], was used for the zigzag channel. Both the zigzag and straight channels have a channel diameter of 2 mm. As seen in Table 25, PCHEs having zigzag channels have better heat transfer properties. In a zigzag channel, bends increase the flow turbulence and improve fluid mixing [79]. This increases the heat transfer coefficient of both the hot and the cold fluid and results in improved heat transfer. However, increasing flow turbulence using bends, as seen in Table 25, increases the pressure drop. Further study was carried out on the zigzag channel PCHE due to its significantly smaller volume.

Table 25: Straight channel and zigzag channel PCHEs

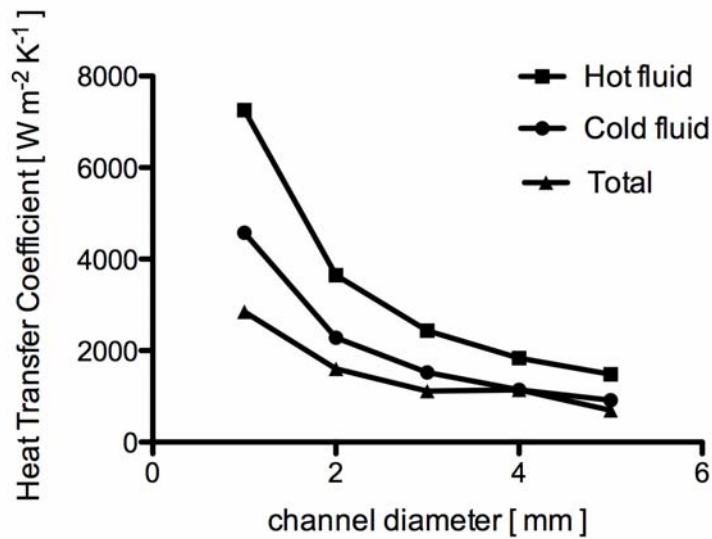
Channel	Zigzag	Straight
V [m ³]	2.99	4.37
h _{cold} [W/K-m ²]	2192.32	959.2
h _{hot} [W/K-m ²]	3280.89	524.7
Re _{cold}	1209.28	450.68
Re _{hot}	10338.09	3855.18
ΔP _{cold} [Pa]	75130.55	5532.84
ΔP _{hot} [Pa]	52904.25	2945.744

Channel diameter study

In this portion of the study hot and cold channel diameters were varied and their impact on the zigzag channel PCHE volume was studied for PCHE1. PCHEs are diffusion bonded which results in a high cost of fabrication. Both materials and fabrication costs are proportional to the volume of the PCHE and the smallest possible volume is desirable in order to reduce the capital cost of the Process Heat system. In order to study the effects of channel diameter on the PCHE volume, both hot cold channel diameters were assumed to be of the same size. A range of channel diameters from 1 mm to 5 mm were studied and, as shown in Figure 56a, it was found that the PCHE volume increases linearly with an increase in channel diameter. This increase in volume can be attributed to a decrease in the heat transfer coefficient as shown in Figure 56b. However, one of the disadvantages of using smaller channels is a larger pressure drop. The pressure drop which is of the order of kPa, is small compared to the operating pressure. The next section discusses the the impact of S-CO₂ mass flow rate on the PCHE volume.



(a) PCHE Volume



(b) Heat transfer coefficients

Figure 56: PCHE volume and heat transfer coefficient as a function of channel diameter

S-CO₂ mass flow rate study

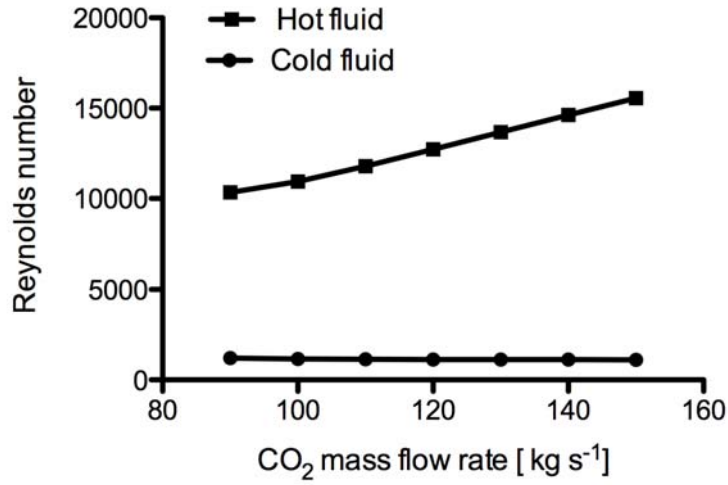
Previous studies indicate that channel diameters less than 2 mm suppress eddies and reduce flow turbulence, thus adversely affecting heat transfer [79]. As a result, further optimization for PCHE1 was performed by varying the S-CO₂ mass flow rate for a zigzag channel counterflow configuration having hot and cold channel diameters of 2 mm each. The S-CO₂ mass flow rate was varied from 90 kg/s to 150 kg/s and the effect of varying this mass flow rate on the hot and cold fluid Reynolds number, pressure drop, heat transfer coefficient and PCHE volume were studied. The cold fluid mass flow rate was fixed at 22 kg/s due to its

being constrained by the required heat rate for PCHE1 (35 MW) and the outlet temperature needed to meet the heat storage temperature requirements.

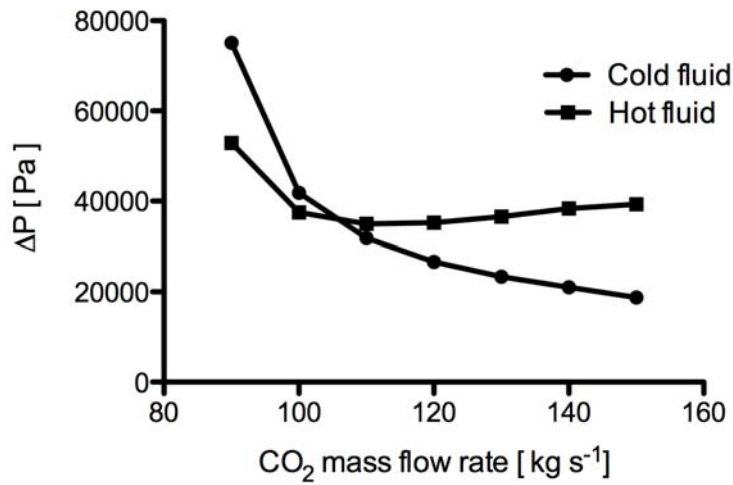
Reynolds number and pressure drop

As seen in Figure 57a, the cold fluid is in the laminar flow regime and its Reynolds number is insensitive to the mass flow rate of the hot fluid whereas the Reynolds number of the hot fluid increases linearly with an increase in the mass flow rate. Figure 57b shows that the cold fluid pressure drop decreases with an increase in the mass flow rate of the hot fluid. As explained in the next section, this occurs because a higher mass flow rate of the hot fluid increases its turbulence and improves heat transfer which leads to a reduction in the length of both hot and cold channels. For the same mass flow rate and channel diameter, a shorter channel results in a smaller pressure drop for the cold fluid.

The pressure drop of the hot fluid first decreases and then increases with an increase in the hot fluid mass flow rate. A change in the mass flow rate from 90 kg/s to 100 kg/s , reduces the pressure drop because the decrease in channel length is greater than the increase in the pressure drop due to an increase in frictional losses. However, for larger mass flow rates, the latter dominates and the hot fluid pressure drop is seen to increase as a function of the mass flow rate of the hot fluid.



(a) Reynolds number



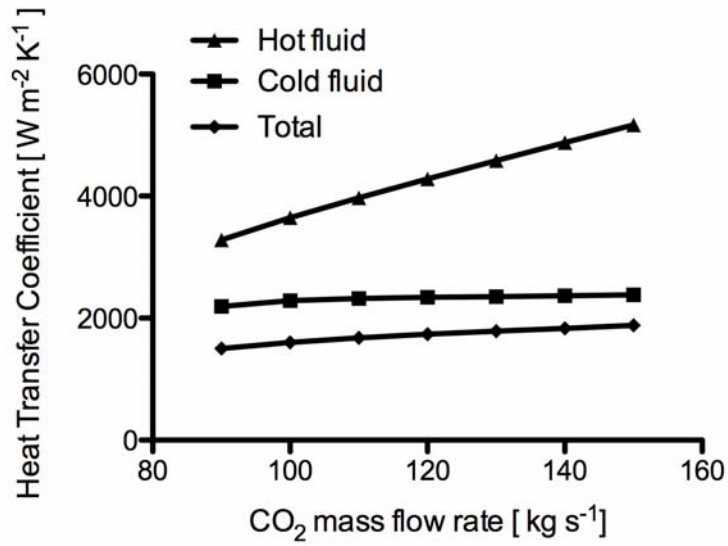
(b) Pressure drop

Figure 57: Reynolds number and Pressure drop as a function of S-CO₂ mass flow rate

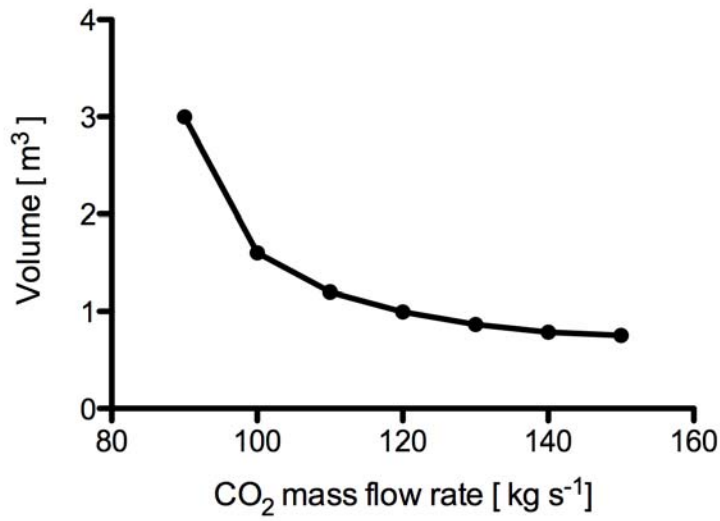
Heat transfer coefficient and PCHE volume

As shown in Figure 58a, the heat transfer coefficient of the cold fluid is insensitive to the mass flow rate of the hot fluid. However, the heat transfer coefficient of the hot fluid increases with an increase in its mass flow rate. This increases the total heat transfer coefficient and, as seen in Figure 58b, reduces the PCHE volume. Counterintuitively, the total heat transfer coefficient (HTC) of a PCHE is not the average of the hot and cold HTCs. The total HTC is calculated using the expression in Equation 44 [137] in which h_h and h_c are the HTCs for the hot and cold fluids respectively, c_l is the conduction length, and k is the thermal conductivity of the PCHE plates.

$$h_{tot} = \left(\frac{1}{h_h} + \frac{c_l P_h}{k2P} + \frac{P_h}{h_c P_c} \right)^{-1} \quad (44)$$



(a) Heat transfer coefficients



(b) PCHE volume

Figure 58: Heat transfer coefficients and PCHE volume as a function of S-CO₂ mass flow rate

Conclusion

This work indicates that zigzag channel PCHEs are significantly smaller than straight channel PCHEs having the same operating parameters. It was also observed that the PCHE volume increases with an increase in the channel diameter and decreases with an increase in the mass flow rate of the hot fluid.

Part IX

Appendix D: Implementation of switchgrass as feedstock for a industrial biofuels process in a nuclear complex

Abstract

This article describes new calculations that contribute to this study of the use of switchgrass (*Panicum virgatum*) in a nuclear-powered biorefinery. Areas examined include location, transportation methods and costs, carbon emissions, and injection of feedstock as fuel for the process.

Background

The current development of the nuclear reactor complex by the 22.033 design team consists of several challenges rooted in the provision of enough resources to the different sectors at the appropriate rates. The biofuels refinery has to be scaled according to the amount of hydrogen available for the refining procedure. The gasification and distillation processes contained within the biorefinery are dependent on the available power from the process heat, and therefore, since hydrogen is the ultimate limiting factor, the process heat designers must engineer to sustain those infrastructures.

With the power available from the lead-cooled fast reactor at 3.6 GeV, the hydrogen facility is able to provide 7.9 kg/s of hydrogen gas to our refining process. The biorefinery is thus allowed to operate with an input of 2,903 t/d¹ (24.38 kg/s), which amounts to 9.2 kg/s of end-product produced after processing. To meet these needs, the process heat group is providing a large heat source to the biorefinery, which will allow for 13.7 MW of steam to be used in the gasification process. The cooling of syngas from this process to the acid-gas removal process will provide 19 MW back to the heat source. Based on current crude oil and natural gas prices, the biofuels facility should be expected to generate about \$1.7 M in revenue on a daily basis from end products, all the while contributing to an American-based sustainable fuel source.

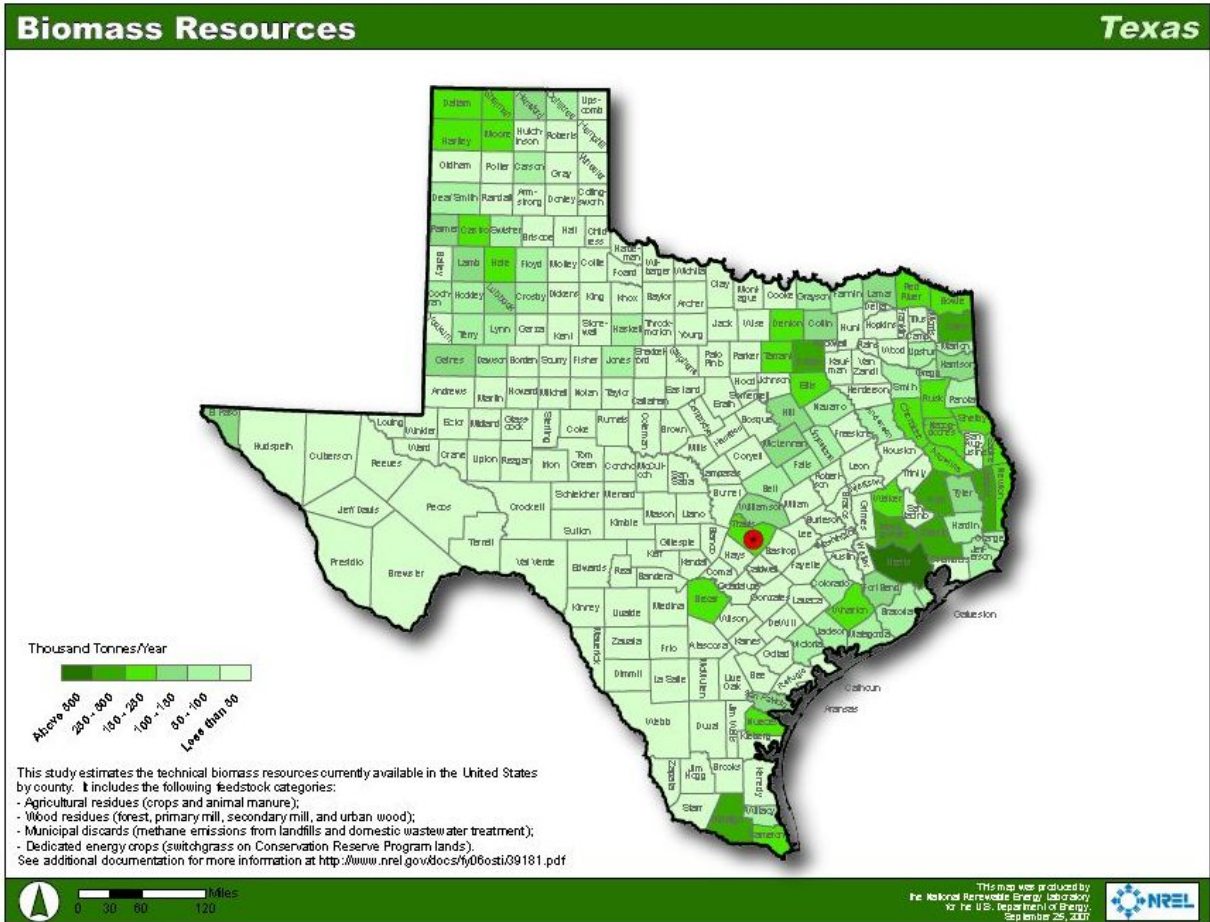
Introduction

The design requirements surrounding the successful implementation of these flow rates revolve around facilitating the injection of the feedstock into the refinery, having a reliable heat dump, and coordinating the operating times of all sectors (i.e. the core life cycle and shutdown period of the hydrogen facility.) A natural reservoir is required for cooling the Fischer-Tropsch (FT) process, and this treatment must meet EPA standards for environmental impact. Backflow preventers must be installed in all pipelines involving large amounts of flammable gas, such as the syngas and hydrogen pipelines, in the case of large pressure waves. Multiple flares can also be used to get rid of excess pressure.

The site must allow room for temporary switchgrass (SG) storage, and this in turn must be located a safe distance from the holding tanks for the biofuels due to flammability. Storage must be climate-controlled and have a system of feeding biomass into a conveyor system. If temporary storage is at capacity, there must be open grounds upon which excess material can be dumped to be used later. This requires loading operators to be on hand on a continual basis, and for the moisture content to be monitored for optimal levels. Storage of material should amount to holding three days worth of feedstock in case of shortages caused by traffic congestion, severe weather or natural disasters. In any case, this would allow enough time for the engineers to coordinate a refinery shutdown with minimal impact.

Loading bays for SG must have direct access to major highway systems and be designed to reduce on-site traffic conditions. The distance between the facility and the cropland providing the feedstock should be less than 200 km, and SG densification should be performed as close to the land as possible to allow for more efficient transportation and fewer carbon emissions. The grain trucks used for transportation are limited

¹These values are based on an approximately 20 hr daily operating period.



Map produced by the National Renewable Energy Laboratory for the U.S. Department of Energy.

Figure 59: Map of biomass resources in Texas. Harris County is noticeable in dark green to the lower right. (National Renewable Energy Laboratory)

by the allowed tonnage of the highway system used. They must feature an efficient unloading mechanism, possible by hydraulic-powered dumping, and the pelletized SG should be contained in such a fashion that minimizes operational losses. Ideally, some sort of grain elevator will be used to feed a lock-hopper, which will directly feed into the gasifier.

Location

Harris County, Texas is a prime location for the reactor complex. Located in the southeastern portion of the state, it is situated near a large natural body of water and has considerable biomass resources [91] (see Figure 59). The region is in a low-risk area for wildfire [21] and receives around 65 inches in annual precipitation [155], and has a climate that is less harsh than more established growing regions in the midwest. It is considered part of the greater Houston metropolitan area, and the nearby Trinity Bay can be used as a natural reservoir for cooling the FT process and as a general source of water for intake. (This environmental resource will be subject to an EPA-limited 36°C on temperature increases.)

To meet the daily reactor requirement of 2903 t/d ($1.06 \times 10^6 \text{ t/yr}$), and considering that SG is a perennial crop that can be cultivated at 14.6 t/ha and harvested twice a year, the growing region will need to cover at least 36,287.5 ha (140.1m²). To allow for a consistent input of feedstock, the engineers will need to set up a network of suppliers (both primary and secondary/back-up) that can ensure a dependable flow of product. There are existing highways in all directions from Trinity Bay that can allow for multiple providers, and

Harris County is surrounded by other regions containing considerable biomass resources.

Transportation

Road

Grain trucks can be used to transport densified SG from the farmland to the storage facilities on the reactor site. If the SG is compressed to a density of about 1300 kg/m^3 , a large 2 ft grain bed with a 905 ft^3 (25.6 m^3) capacity should be able to haul at least $3.4 \times 10^4 \text{ kg}$ (33.3 t) of feedstock. To meet the daily requirement for feedstock, this would imply around 85 trips to the reactor site on a daily basis (not acknowledging relief from the amount available in storage.)

If College Station, TX was taken as the nearest growing location, this would mean that 98.1 mi (157.9 km) would need to be traveled on a 1.6 hr^2 one way trip. A typical Peterbilt® truck has a fuel efficiency of about 10 miles per gallon [9], so about 20 gallons of diesel are consumed on a round-trip, amounting to about \$70 worth of fuel. For a full day of refinery operation, this would imply an expense of \$5,950.

The trucks would need to travel along US-290 W and TX-6 (Texas State Highway), and could possibly resort to the I-45 N and TX-105 W to avoid congestion (although this would mean a longer trip). If we use a Peterbilt Model 388 Day Cab (front/tandem rear axle of 12,000/40,000 lbs) with a load of 66,600 lbs and a tare of 4,440 lbs, a tonnage limit of 80,000 lbs over 6 axles[20] can be met.

Rail

Transportation by rail is highly feasible in Harris County due to existence of a well-developed railroad network, although it introduces trade-offs in adjusting the amount of freight cars for a particular bulk load needed by the refinery. However, it allows larger amounts of feedstock to flow unimpeded by ground traffic patterns and for a more systematized unloading system, along with greater loads and capacities through freight cars.

The Union Pacific (UP) Railroad would comprise most of the rail networks used. A large UP 65 ft (19.8 m) covered hopper car with three compartments and a capacity of $5,200 \text{ ft}^3$ (147.24 m^3) can haul 191,425 kg of densified SG, which is just under the lower load limit for these cars [117]. To supply the reactor on a daily operating basis, that would amount to at least 14 cars at full capacity delivering to the reactor site.

The site will need to have local rails that will ensure the cars can remain idle or in use for the proper amount of time without interfering with regular rail traffic. These hopper cars will gravity-feed the SG pellets into the unloading and conveying system for temporary storage. If storage is at capacity, then the cars can use an alternative rail to dump onto open storage space, although this presents the risk of exposing the pellets to variable amounts of moisture from the environment.

Storage

SG in its pelletized form will amount to $2,026 \text{ m}^3$ of volume used per day of operation. To operate with a guaranteed flow of feedstock, storage should supply for many days of operation throughout the growing season. If we get a full yield twice a year from 140 mi^2 of farmland, and if we use a large grain elevator of $1.4 \times 10^7 \text{ bu}$ ($4.8 \times 10^5 \text{ m}^3$) [35], we can supply for a maximum of 230 days of operation. With $4.8 \times 10^8 \text{ kg}$ as an upper estimate yield of 140 mi^2 of farmland in half a year, this would amount to $3.7 \times 10^5 \text{ m}^3$ of densified feedstock, which is enough to fit entirely in such a grain elevator. Thus, economic factors will come into play into deciding whether to build such a facility on site, to build a smaller one, or to employ on of the many existing grain elevators around Harris County (see [35] for examples).

Local managers of grain elevators would store pelletized feedstock until they can be transported to the site for temporary storage and implementation. Temporary storage would amount to a small grain elevator of approximately three operating days capacity specifically engineered for conveying feedstock into the gasification process.

²The truck can be assumed to have an average speed of 60 mi/hr.

Emissions

Carbon emissions are limited by the EPA to 15 g/bhp-hr (6.1 g/MJ) of nitric oxides and Non-Methane Hydro-Carbons (NMHC). Following these standards, on a typical day of round-trip site-to-reactor driving, there are 5,100 g/bhp of CO emissions and 850 g/bhp in NO_x/NMCH. With a total weight of 83,000 lbs (38,000 kg) traveling at 60 mi/hr (26.8 m/s) for 4 hours a day, with 85 trips to supply the refinery, this would amount to approximately 40 kg CO and 7 kg NO_x/NMCH emitted in a single day.

Emissions resulting from rail transport are regulated by the EPA at 1.28 g/bhp-hr of CO and 4.95 g/bhp-hr of NO_x for a modern engine [10]. Since locomotives typically consume 1 gallon of fuel per 400 ton-miles [10], a General Electric 8-cylinder model 7FDL with a continuous power output of 2,045 bhp (1,525 kW) at 1,050 RPM [56] can haul 2,903 tons from College Station in approximately 5 hours, using about 700 gallons of fuel. If these engines meet EPA standards, they should thus be expected to emit around 13 kg CO and 51 kg NO_x every trip.

Conclusion

With the general conditions in place for building the reactor complex in Texas, further measures can be taken such as assessing the reactor safety and disaster prevention mechanisms, availability of labor, cost of distribution, and environmental regulations, among other things. It will be ideal in defending this choice of location to use superimposed maps of climate, precipitation, etc, and to compare with GIS maps of potential biomass growing regions. It is also necessary to establish a communication network between engineers at the complex and farmers in the region to ensure a steady flow of feedstock.

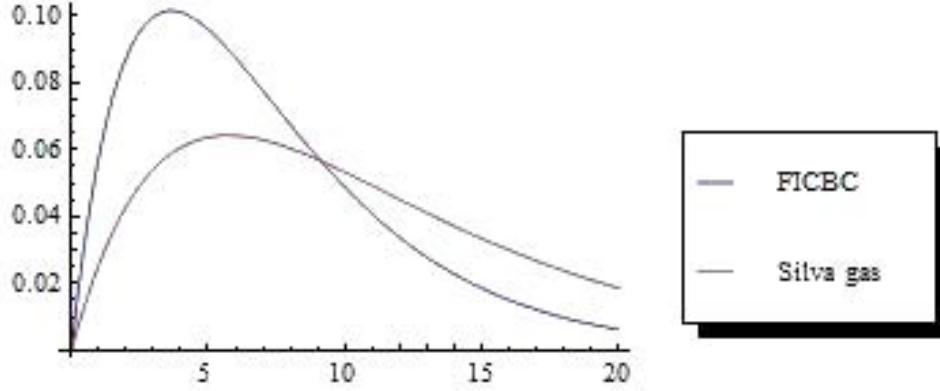


Figure 60: Silva gas and FICBC for product selectivity

Part X

Appendix E: Impact of gasifier design on FT product selectivity

A gasifier produces a syngas stream which is then fed into FT reactor. Different gasifier designs will produce syngas streams of different compositions and H_2/CO ratios. Since the H_2/CO ratio critically impacts product selectivity, it is necessary to evaluate how different gasifier design choices affect final product composition. Depending on the final product requirement, the conditions of the reactor can be modified to alter the composition of product F-T liquid. The parameters of the reactor have been chosen to maximize the production of carbon number 5-20 molecules which can be used for biogasoline and biodiesel production. Two designs of gasifier were proposed and their final product selectivities were analyzed using Equation 45 for the probability of chain growth.

$$\alpha = \frac{0.23}{H_2/CO + 1} + 0.63 \cdot [1 - 0.0039(T - 533K)] \quad (45)$$

$T = 240^\circ\text{C} = 513\text{ K}$ is the operating temperature of the reactor and for Silva gas gasification process which is an American design, the hydrogen to CO ratio in the syngas stream is $H_2/CO = 22/38.2 = 0.57 \approx 0.5$. For the Swedish FICBC process, $H_2/CO = 44.4/22.9 = 1.94 \approx 2$. We can then compare the chain growth probability of the two different gasifier designs at the same temperature by using Equations 46 and 47.

$$\alpha_{Silva} = \frac{0.23}{H_2/CO + 1} + 0.63 \cdot [1 - 0.0039(T - 533K)] = 0.84 \quad (46)$$

$$\alpha_{FICBC} = \frac{0.23}{H_2/CO + 1} + 0.63 \cdot [1 - 0.0039(T - 533K)] = 0.76 \quad (47)$$

We can then apply ASF distribution to calculate mass fraction of molecules with carbon number, n , using Equations 48 and 49.

$$\chi_n^{Silva} = 0.16^2 n \cdot 0.84^{n-1} \quad (48)$$

$$\chi_n^{FICBC} = 0.24^2 n \cdot 0.76^{n-1} \quad (49)$$

Figure 60 shows mass fraction as a function of carbon number for both processes.

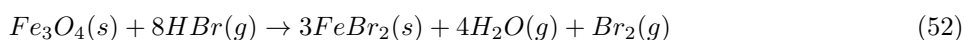
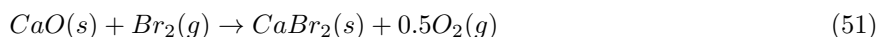
Naphtha is a term that refers to mixture of hydrocarbon molecules having carbon numbers between 5-12. The term distillate covers hydrocarbons with n between 12-20. Wax refers to carbon number 20 or more

hydrocarbons. Using this definition, we can tabulate the mass flow rate for naphtha, distillate and wax streams. Silvagas is chosen as it produces more heavy diesel products and is a design that is patented in the US. This will impact positively on feasibility of our design.

Appendix E: The UT-3 Hydrogen Production Process

Background

UT-3 hydrogen production is a four-staged thermochemical water splitting process using four separate reactor units connected in series, which undergo the following reactions at the indicated desired temperatures. Each set of calcium reactors and iron reactors are cyclically linked such that the products of one reaction become the reactants of the other, and can operate continuously with a periodic reversal of the flow direction of gaseous compounds [83].



Multiple scalings of a UT-3 hydrogen production plant have been done previously using the software ASPEN-PLUS [130] and other means to determine the thermal power required for a particular hydrogen production rate [145]. Each reference used for the scaling of this UT-3 hydrogen production plant was for a similarly designed UT-3 reactor system to ensure the most accurate extrapolations possible for the hydrogen production rate of interest in this study. Future analysis with ASPEN or other similar software would be ideal to ensure the accuracy of the required thermal power for the requested hydrogen mass flow by the biofuels production plant; however, extrapolation using studies that have utilized such software provides the most accurate value for the thermal power requirement presently possible.

Reactions 50 and 51 in the UT-3 process occur in two different calcium reactor units. Pellets containing either CaBr_2 or CaO as the initial compounds will transform into the other calcium reagent cyclically during the continuous hydrogen production operation of the UT-3 plant. There is a 76% volumetric difference in the structure of the two calcium compounds, which could cause fines to form and pellet sintering as cycling progresses [94]. Supports to stabilize the calcium reagents, and well as porous configurations of CaO micro-pellets to allow space for expansion and contraction during the UT-3 cycle, were researched and implemented in each calcium reactor unit to ensure the structural integrity and material stability of the calcium reagent pellets.

The optimal temperatures for each reactions were identified as 760 °C, 572 °C, 220 °C, and 560 °C respectively, as shown in Figure 61. Steam is used to both react with solid chemicals to produce the desired products and mix with and transport gaseous products to the next reactor. Once the reactions have run to completion in a forward progression, the flow of the steam cycle will be reversed, utilizing the products remaining in the reactors as the reactants for the corresponding reverse reaction. Figure 61 depicts a schematic of the UT-3 plant in forward flow. Heat exchangers (denoted by the orange, crossed circles) are placed in between the reactors to ensure that the gaseous reactants enter the reactor at the correct temperature. Two compressors (one for forward flow, one for backward flow) are placed in series with the reactors, creating the pressure differential to sustain the flow progression of the gaseous products. H_2 and O_2 separators remove the products from the system; the H_2 will be sent to a bio fuels production plant while the excess O_2 will be sold or vented to the atmosphere.

UT-3 Plant Design

Analytical Scaling of the UT-3 Hydrogen Production Plant

The analytic scaling of the UT-3 hydrogen production plant was conducted using information from two previous studies of commercial scale UT-3 hydrogen production plants, is presented in Table 26 for convenience.

Table 26: Hydrogen Production Rates and Thermal Power Requirements

H ₂ Production Rate (Nm ³ h ⁻¹)	Thermal Power Requirement (MW)	H ₂ Production Rate (Nm ³ h ⁻¹) per MW
20000	176.7	113.2 [145]
20000	157.8	126.7 [145]
30000	225.4	133.1 [130]

Though there is a range of 20 MW over all values analyzed, the plants yielding the values of 126.7 Nm³h⁻¹MW⁻¹ and 133.1 Nm³h⁻¹MW⁻¹ are most similar to the design used in this study, and provides a roughly constant hydrogen production rate per MW suggesting the assumption of a linear behavior of hydrogen production rate per MW is a reasonable one. Originally, only 0.7 kg s⁻¹ was required by the biofuel production plant, which corresponds to 30090 Nm³h⁻¹ and thus would require approximately 226.1 to 237.29 MW of thermal power. This scaling was taken simply as an estimation for the thermal power required for the desired hydrogen production rate, and due to the large uncertainty of whether hydrogen production rate per MW actually scales linearly up to the desired production rate of 30090 Nm³h⁻¹, values of thermal power requested from the process heat design team were upwards of 300-400 MW. Though this requirement may seem arbitrary, without a more sophisticated analysis for thermal power requirements using a software package such as ASPEN, it is clear the favorable situation for the hydrogen production plant would be a surplus of power rather than the alternative. Should the hydrogen production plant require less than 300-400 MW of thermal power, the process heat team can redistribute that heat to either the biofuels production plant, or back to the core group to feed into the secondary turbine to produce additional electricity.

However, after subsequent changes in required biofuel production rate, the required production of hydrogen was raised to 7.9 kg s⁻¹. This larger production rate of 316351 Nm³h⁻¹ would require approximately 2376.8 to 2496.9 MW of thermal power using two most conservative values for power requirements per Table 26. This quantity of thermal power is too large to be provided by the process heat system, and thus with this new hydrogen production requirement, the UT-3 cycle is no longer a viable approach for this design. This large thermal power requirement motivated the transition to high-temperature steam electrolysis (HTSE) for this hydrogen production plant. Nevertheless, should such a large hydrogen production rate not be required, the UT-3 process is an attractive hydrogen production approach that has been studied thoroughly for implementation on the scale of 0.5 - 0.75 kg s⁻¹ hydrogen production rates.

Plant Schematic

The optimal temperatures for each reaction have been identified as 760 °C, 572 °C, 220 °C, and 560 °C respectively. The steam is used to both react with solid chemicals to produce the desired products and to serve as a working fluid to transport gaseous products to the next reactor unit. Once the reactions have run to completion in a forward progression, the flow of the steam cycle will be reversed, utilizing the products remaining in the reactors as the reactants for the corresponding reverse reaction. Figure 61 depicts a schematic of the UT-3 plant in forward flow. Heat exchangers (denoted by the orange, crossed circles) are placed in between the reactors to ensure that the gaseous reactants enter the reactor at the correct temperature. Two compressors (one for forward flow, one for backward flow) are placed in series with the reactors, creating the pressure differential to sustain the flow progression of the gaseous products. H₂ and O₂ separators remove the products from the system; the H₂ will be sent to a bio fuels production plant while the excess O₂ will either be sold or vented to the atmosphere.

Materials and Components

Calcium Reagent Structures

A proposed design for a stable calcium pellet structure which can endure the cycling expansion and contraction of the calcium reagents during the UT-3 process has been thoroughly researched and is presented graphically in Figure 62 [131].

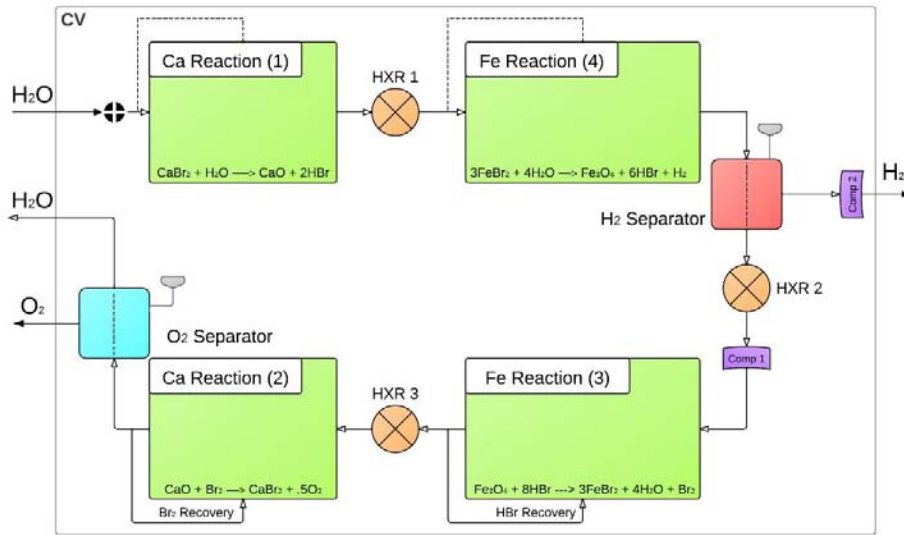


Figure 61: Block diagram of the UT-3 plant.

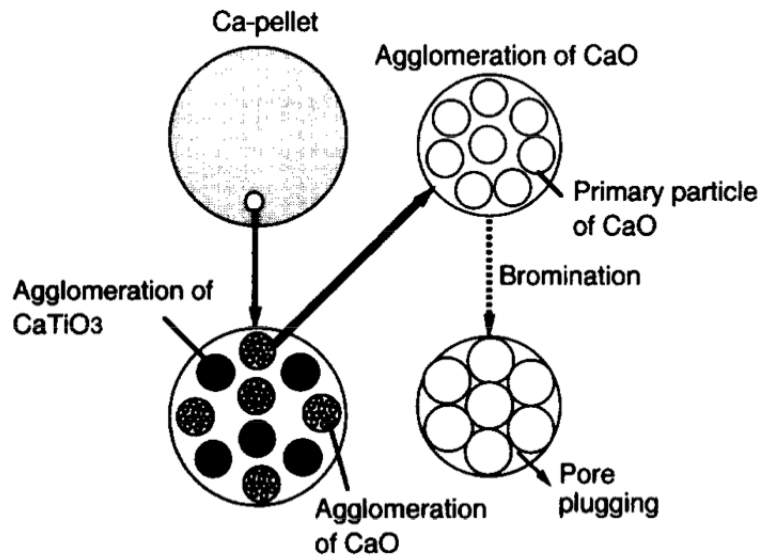
Calcium pellets are formed using smaller pellets that contain both the reactant CaO and binder CaTiO_3 that maintains structural integrity while the CaO expands to CaBr_2 , and vice versa. The CaTiO_3 agglomerations are essentially solid spheres, whereas the CaO pellet contains a smaller substructure of CaO primary particles arranged uniformly throughout the smaller sphere with considerable space between each primary CaO particle before bromination. While CaO undergoes bromination and transforms into CaBr_2 , the space between the primary particles decreases due to the volumetric expansion from CaO to CaBr_2 , and the reaction goes to completion just as the primary particles begin to exert stresses on one another. Due to the presence of voids for CaO to expand into during bromination, the expansion of each substructure is fairly small, and thus the relatively small volumetric change of an entire calcium pellet during cycling between CaO and CaBr_2 coupled with the structural supports of CaTiO_3 provide a stable calcium structure which can endure the UT-3 process cycles. This proposed design would be implemented in both calcium reactors in this UT-3 plant to ensure the structural integrity of calcium reagent pellets.

Hydrogen Separator Membrane

Hydrogen membrane separation technology has emerged as an attractive option to the energy-intensive processes of cryogenic distillation and pressure swing adsorption [28], and consequently has been chosen as the method of H_2 separation for the UT-3 cycle. Various types of membranes exist, each offering benefits when optimized for the system's temperature. Of these choices, metallic membranes (optimized at $\sim 350^\circ\text{C}$) and ceramic membranes (optimized at $\sim 500^\circ\text{C}$) were identified as contenders. Ceramic membranes were ultimately chosen as they presented fewer poisoning concerns [28]. Looking at the permeance of the various types of ceramic membranes, a Zr Silica [113] membrane was compared to the chemical vapor deposition tetra-ethyl-ortho-silicate (CVD TEOS)[132]. The results of the comparison are summarized by the table 27. The Zr silica was chosen specifically because it would require 39200 m^2 of membrane area to achieve the 7.9 kg/s compared to the CVD TEOS which required 98000 m^2 .

Oxygen Separator Membrane

The thermochemical decomposition of water also produces oxygen in addition to hydrogen which must be removed before the steam can be recycled. Since oxygen in its gaseous form is much larger than hydrogen gas and is comparable to or larger than the steam molecules it must be separated from, oxygen separation is not as easy. However, oxygen-ion conducting ceramic membranes have been shown to produce oxygen of



Courtesy of Elsevier, Inc., <http://www.sciencedirect.com>. Used with permission.

Figure 62: Proposed Calcium Pellet Design [131]

	CVD (TEOS)	Zr Silica
Diffusion	Solution-diffusion	Solution-diffusion
Permeance [$\frac{mol}{m^2 s Pa}$]	$4.0 * 10^{-8}$	$10.0 * 10^{-8}$
Pressure [MPa]	2.0	2.0
Area Needed [m^2]	1,240	496
Stability Concerns	Phase transition	Phase transition
Poisoning Concerns	H_2S, HCl, Co	H_2S, HCl, Co

Table 27: Comparison of CVD (TEOS) and Zr Silica ceramic membranes

very high purity, separating out the molecules from a mixed gas.

Electric voltage driven separators were considered but deemed to be too energy intensive given that the separation rates were directly proportional to the voltage applied.

Much more promising were found to be mixed conducting membranes. Membrane electrons create oxygen ions which then pass through the membrane due to temperature and pressure differences on the two sides of the membrane. Thus no electrodes are required. The only membrane material found to work at our temperature of 500 C was CeO_2 doped with SmO to provide electrical conductivity.

Corrosion and Bromination

The production of high temperature bromic acid in the UT-3 process is of considerable concern from a material science perspective. The industry standard for dealing with high-temperature corrosive substances are the alloys Fe-20 Cr and Ni-20 Cr. It has been shown that under exposure to high temperature bromic acid both of these alloys form chromium scales which prevent the oxidation of the underlying iron. The best of these two materials was shown to be the Fe-Cr, whose easier scale formation better prevented oxidation and bromination than its nickel counterpart [116]. Other corrosion resistant coatings such as titanium carbide films were also investigated. It was shown that titanium oxides form along with volatile titanium bromides making micro cracks in the coating [146]. For these reasons Fe-Cr would be preferred going forward.

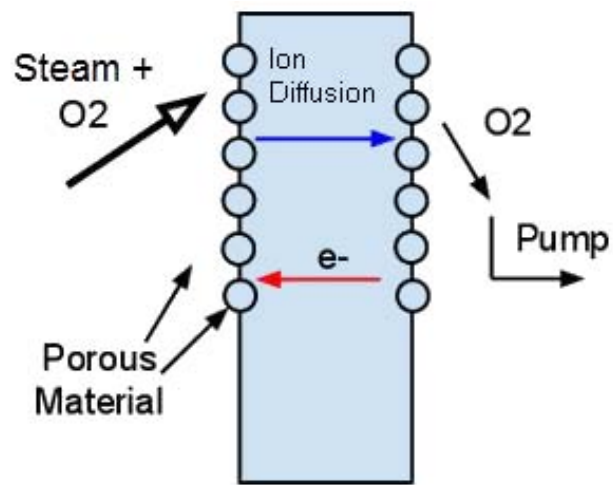


Figure 63: The mixed conducting membrane process. O_2 is separated from the steam mixture and diffused across as ions with the aid of a pump.

Part XI

Appendix G: Excess O₂ and Hydrogen Storage

Excess O₂

Oxygen is a versatile gas with many applications in the industrial, pharmaceutical, and medical world. The largest consumer of oxygen is the modern steel industry. Oxygen is used to enrich air and increase combustion temperatures in blast furnaces, combine with unwanted carbon in the steel-making process to form carbon oxides, and allow greater use of scrap metal in electric arc furnaces. These applications apply to the manufacturing of other metals as well (copper, zinc, lead, etc.).

Hospitals also require large stores of liquid oxygen (kept at cryogenic temperatures) for various medical applications. After the oxygen has been vaporized and divided into smaller containers, it is distributed throughout the hospital to be used in hyperbaric chambers, surgeries, and increasing patient comfort. Hospitals require an oxygen purity over 90% for use with patients which is easily achieved by high temperature steam electrolysis.

Off-site oxygen is delivered to steel plants and hospitals through bulk liquid shipments. Large oxygen tankers can transport 26 m³ (~30,000 kg) of liquid oxygen using refrigerated storage systems. Consequently, hospitals and steel plants purchase oxygen at a price that accounts for refrigeration costs, trucking costs and transfer losses. A revenue will be generated from sales of excess oxygen produced by the high-temperatures steam electrolysis, but this amount will ultimately be dwarfed by the revenue from biofuel sales. (Information provided by Universal Industrial Gases Inc.)

Hydrogen Storage

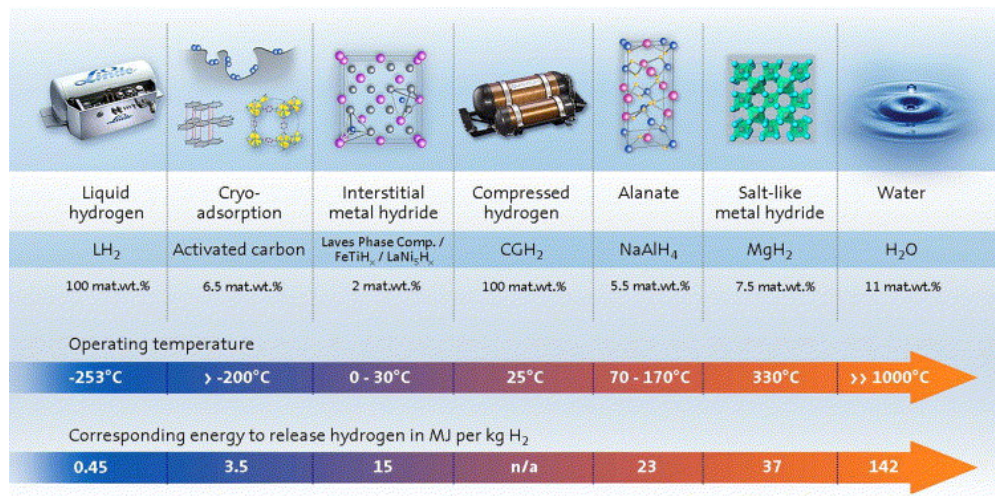
Since this hydrogen production plant is part of a larger facility, it is important that the hydrogen plant be shut down as little as possible in order to keep the other parts of the facility working as well. In initial design, hydrogen storage was included for one day's worth of hydrogen as a liquid so that there was a backup source of hydrogen for the biofuels plant should the hydrogen plant need to be shut down for a short amount of time.

Hydrogen can be stored as a solid, liquid, or gas. Examples of these can be seen in 64. Solid hydrogen storage mostly consists of metal and complex hydrides such as MgH_2 and $NaAlH_4$. In metal hydrides, hydrogen atoms occupy the interstitial sites; in complex hydrides, hydrogen is covalently bound to a metal to form a complex anion which is then balanced to a cation [153]. While solid-state materials have much potential, at this point they have very low storage capabilities, only 2-8% hydrogen by weight. In addition, the thermodynamics and kinetics of solid hydrogen systems are unknown at this point. Solid hydrogen storage will not be a feasible choice until it has a higher storage capacity and more is known about the system.

To store hydrogen as a gas, it must be compressed to 35-70 MPa, though the temperature is merely room temperature. Compressed gaseous hydrogen (CGH₂) is a very well-developed technology which is widely used, especially by fuel-cell vehicle manufacturers. However, because the very high pressures cause strain on the walls, the walls must be made of high-strength materials such as carbon composites and be very thick. Because of this, CGH₂ makes the most sense for small- to mid-scale pressure vessels, which would not be enough to store the amount of hydrogen the biofuels plant requires.

Liquid hydrogen (LH₂) stored at 0.1 MPa and -253C has a very high mass density, which is advantageous. The main concern with liquid hydrogen is that heat flowing from the environment into the storage tank will cause the hydrogen to evaporate. However, this means that larger tanks have implicitly better thermal behavior than smaller ones because they have a lower surface-to-volume ratio. For large volume storage, as this plant plans to have, liquid hydrogen is the most promising option.

The amount of hydrogen to be stored was determined in conjunction with the biofuels team and the process heat team. While a larger amount of hydrogen would provide a larger safety net for the biofuels



Courtesy of Elsevier, Inc., <http://www.sciencedirect.com>. Used with permission.

Figure 64: Hydrogen storage options with corresponding energy, operating temperature, and wt.% [123]

team, allowing the biofuels plant to run longer if the hydrogen plant was shut down, there were significant size and safety concerns. The first proposed number was 26,000 kg of hydrogen, which would be enough for 3 days, but that would be 375m³ of liquid hydrogen, and the process heat team calculated that the plant would need to be 150m away from everything else for safety purposes. By decreasing the amount of hydrogen to just one day's worth, or 9,000 kg, it will only be 125m³ and need to be 40m away. When the amount of hydrogen needed per day increased by more than an order of magnitude, it was determined that hydrogen storage was no longer a smart decision, and was thus removed from the design. However, it is included here for completeness in case future work requires hydrogen storage.

MIT OpenCourseWare
<http://ocw.mit.edu>

22.033 / 22.33 Nuclear Systems Design Project
Fall 2011

For information about citing these materials or our Terms of Use, visit: <http://ocw.mit.edu/terms>.